Master thesis : Laminar and Transitional Shock Wave-Boundary-Layer Interactions

Auteur : Niessen, Sébastien
Promoteur(s) : Terrapon, Vincent
Faculté : Faculté des Sciences appliquées
Diplôme : Master en ingénieur civil en aérospatiale, à finalité spécialisée en "aerospace engineering"
Année académique : 2016-2017
URI/URL : http://hdl.handle.net/2268.2/3278

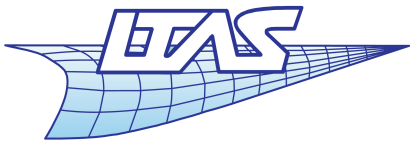

University of Liege
Faculty of Applied Sciences

Academic year : 2016-2017

BiGlobal Stability Analysis: Laminar Shock-Wave/Boundary-Layer Interactions

Submitted by NIESSEN Sébastien to the department of aerospace and mechanical engineering of the University of Liège in partial fulfilment of the requirements for the degree of master in aerospace engineering

Author:	Sébastien Niessen	
Thesis Supervisors:	Prof. Vincent E. Terrapon	ULG (promoter)
	Prof. Stefan Hickel	TU Delft
	Ir. Koen J. Groot	TU Delft

Research project conducted within the Aerodynamics Group, Faculty of Aerospace Engineering, of Delft University of Technology

Abstract

The Shock-Wave/Boundary-Layer Interaction (SWBLI) occurs in the inlet of high-speed engines and on transonic wings, and can exhibit unsteadiness. Large scale unsteadiness may cause the premature fatigue of aerodynamic structures and the instabilities of the air intakes, while small scales cause laminar-turbulent transition, leading to higher friction and thermal load. The latter small scales are studied in this work with stability theory.

The linearised Navier-Stokes equations for stability analyses are used to identify the linear eigenmode growth present in a broad range of flow applications. They present a pertinent approach to identify the origin of the unsteadiness and of the laminar-turbulent transition occurring in the SWBLI. The compressible BiGlobal stability equations are implemented and the validation of the solver with well-known Blasius flows shows excellent agreements with the literature.

The convective instability represented by the Tollmien-Schlichting waves in developing boundary layers is thoroughly analysed. A moving reference frame is used to represent the most unstable instability by one unique eigenfunction, aiming to improve the effectiveness of the BiGlobal approach drastically. Finally, the convective instabilities associated with the Kelvin-Helmholtz waves and the underlying characteristics of steady modes existent in the SWBLI are detailed through the Reynolds-Orr energy equation.

Acknowledgements

First and foremost, I would like to thank Professor Stefan Hickel for giving me the opportunity to join his research group at TU Delft and for the trust he has placed in me. His very warm welcome makes the time there really enjoyable and I am grateful for his advices, about scientific and more personal aspects, from the beginning of my internship until writing the final lines of my thesis.

I really want to thank my advisor Koen Groot who followed enthusiastically my research project. He always find an exciting way to present scientific approach that makes me want to improve my knowledge and to make new discoveries. I am very grateful for his availability and for the huge effort he put in my thesis. I am looking forward to continue our researches.

To Professor Vincent Terrapon, my promoter, for the trust he has placed in me to conduct my master thesis in TU Delft and for giving me the opportunity to work on the research topic I wanted. I am really excited to pursue a PhD in his department at ULiège and I am eagerly awaiting for our upcoming project with Stefan and Koen.

I want to show my gratitude to my INCA colleagues and friends, Jordi Casacuberta and Lluis Laguarda. We had fun time discussing about CFD, "as good as it gets", and about general programming issues that we fixed together. Moreover, I would like to thank all the student-colleagues of the HSL basement who make this place agreeable.

I definitely want to thank all my friends in Belgium. They always supported my choice and my research ambitions, even though the topics seem sometimes crazy. We constantly have very good time together and, without them, the achievement of my master would not have taken the same happy ending.

Last, but not least, I want to thank my family for their encouragements and for supporting my choices. I am very grateful for giving me the opportunity to let my scientific curiosity grows. Even though Delft is not so far away, it was really good to be back home and to enjoy simple moments.

Contents

List of Figures

List of Tables

List of Symbols

Acronyms

CBL Compressible Boundary Layer

DNS Direct Numerical Simulation

ESFD Encapsulated Selective Frequency Damping

HLLC Harten-Lax-van Leer-Contact

KH Kelvin-Helmoltz

LES Large-Eddy Simulations

LPPE Linearised Pressure Poisson Equation

LST Linear Stability Theory

NSE Navier-Stokes Equations

ODE Ordinary Differential Equation

PSE Parabolised Stability Equation

RANS Reynolds Averaged Navier Stokes

SFD Selective Frequency Damping

SWBLI Shock-Wave/Boundary-Layer Interaction

TS Tollmien-Schlichting

WENO Weighted Essentially Non-Oscillatory

Greek Symbols

α	Streamwise wavenumber	$[\mathrm{m}^{-1}]$
β	Spanwise wavenumber	$[\mathrm{m}^{-1}]$
δ	Boundary layer height at $U = 0.99U_e$	[m]
δ^*	Boundary layer displacement thickness	[m]

ϵ	Infinitesimal variable	general
η	First in-plane (wall-normal) coordinate in BiGlobal system	[-]
γ	Specific heat's ratio	[-]
λ	Lamé's first viscosity parameter	[Pa.s]
μ	Lamé's second viscosity parameter	[Pa.s]
ω	Complex frequency	[rad s^{-1}]
$\overline{\rho}$	Base flow density	[kg m^{-3}]
ρ'	Perturbation density	[kg m^{-3}]
Θ	Complex phase	[m^{-1}]
θ_d	Deflection angle of the shock	[°]
θ_w	Wave angle of the shock	[°]
ξ	Second in-plane coordinate in two-dimensional BiGlobal system	[-]

Roman Symbols

$\overline{h}$	Enthalpy	[J]
$\overline{P}$	Base flow pressure	[Pa]
$\overline{Q}$	General base flow variable	general
$\overline{T}$	Base flow temperature	[K]
$\overline{U}$	Base flow streamwise velocity	[ms^{-1}]
$\overline{V}$	Base flow wall-normal velocity	[ms^{-1}]
$\overline{W}$	Base flow spanwise velocity	[ms^{-1}]
$\tilde{p}$	Complex perturbation amplitude of pressure	[Pa]
$\tilde{q}$	General complex perturbation amplitude	general
$\tilde{T}$	Complex perturbation amplitude of temperature	[K]
$\tilde{u}$	Complex perturbation amplitude of streamwise velocity	[ms^{-1}]
$\tilde{v}$	Complex perturbation amplitude of wall-normal velocity	[ms^{-1}]
$\tilde{w}$	Complex perturbation amplitude of spanwise velocity	[ms^{-1}]
C	Sutherland reference value	[$kgm^{-1}s^{-1}K^{-0.5}$]
c_f	Skin friction coefficient	[-]

c_p	Heat capacity ratio	[J/K]
C_r	Chapman-Rubesin constant	[-]
k	Thermal conductivity coefficient	[$\mathrm{Wm^{-1}K^{-1}}$]
k_y	Wall-normal wavenumber	[$\mathrm{m^{-1}}$]
l	Blasius length	[m]
M	Mach number	[-]
N_x	Number of grid points in the streamwise direction	
N_y	Number of grid points in the wall-normal direction	
p	Static pressure	Pa
p'	Perturbation pressure	[Pa]
p_{inc}	Pressure for incipient separation	[Pa]
Pr	Prandtl number (freestream)	[-]
Q	General instantaneous flow variables	general
q'	General perturbation variable	general
R	Specific gas constant	[$\mathrm{m^2s^{-2}K^{-1}}$]
Re	Reynolds number	[-]
S	Sutherland effective temperature	K
T'	Perturbation temperature	[K]
x	Streamwise coordinate	[m]
y	Wall-normal coordinate	[m]
z	Spanwise coordinate	[m]

Sub- and Superscript

$\{.\}_i$	Imaginary part
$\{.\}_r$	Real part
$\{.\}_s$	Quantity at the separation location
$\{.\}^+$	Quantity in viscous unit
$\{.\}^d$	Dimensional variable
$\{.\}_x$	Derivative w.r.t x

$\{.\}_y$ Derivative w.r.t y

$\{.\}_z$ Derivative w.r.t z

$\{.\}_2$ Quantity in freestream after incident shock

$\{.\}_3$ Quantity in freestream after all the shocks reflection system

$\{.\}_\infty$ Quantity in freestream

$\{.\}_{\overline{T}}$ Derivative w.r.t $\overline{T}$

$\{.\}_e$ Quantity at the edge of the boundary layer (equivalent to freestream)

$\{.\}_{imp}$ Quantity at shock impinging location

$\{.\}_{SB}$ Quantity related to the separation bubble

1. Introduction

1.1 Motivation

The ubiquitous presence of the Shock-Wave/Boundary-Layer Interaction (SWBLI) in applications ranging from the transonic to the hypersonic regime makes it a thoroughly studied fundamental phenomenon in fluid dynamics. The laminar/turbulent SWBLI impacts high-speed aerodynamic surfaces and engines with the ultimate effect of increasing the drag in addition to the potential unsteadiness of the shock-induced separation bubble. The SWBLI can affect significantly the performances of the aircraft at different scales and hence it consists of a worthwhile research work for the improvement of fuel consumption.

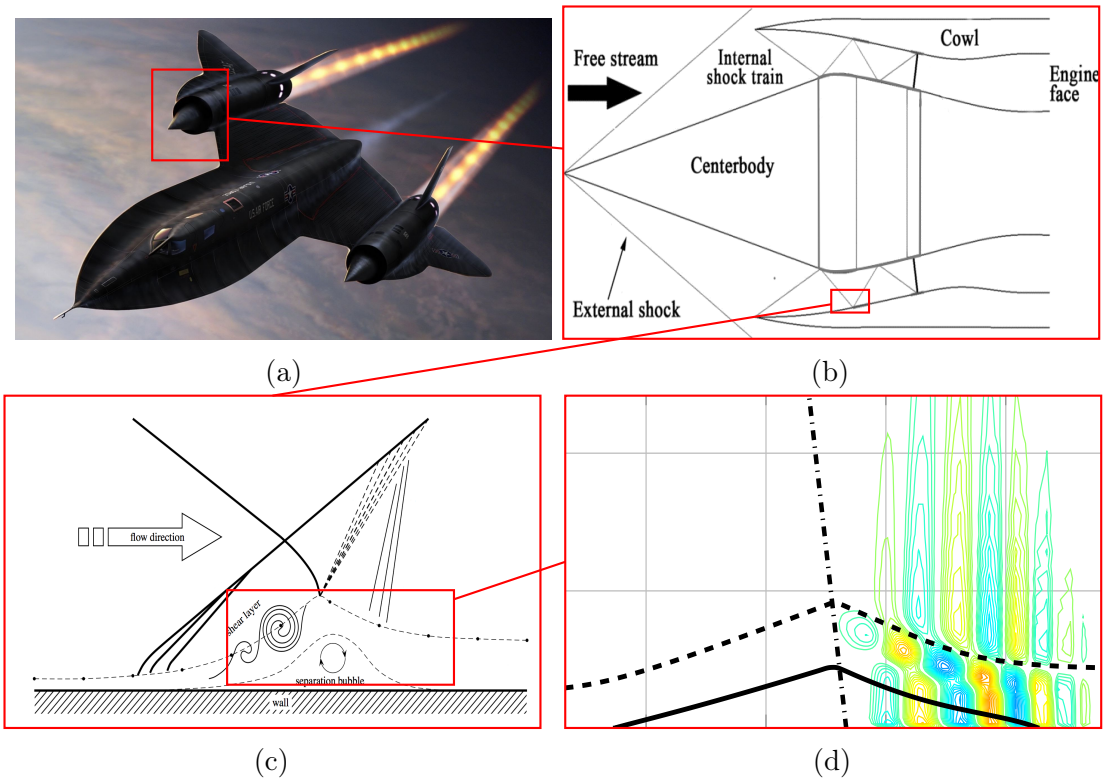

Figure 1.1.1: From the largest scales to the smallest scales of the SWBLI: Lockheed SR-71 (a), supersonic air intake (b) from Yongzhao et al. [2015], laminar SWBLI (c) from Touber and Sandham [2009] and Kelvin-Helmholtz instability (d) from present work.

In regards of the largest scale of the high-speed aircraft, depicted in Fig. 1.1.1a, the shocks along the aerodynamic surfaces induce wave drag to be added to all the other drag components. At a scale relative to the engine (Fig. 1.1.1b), the shocks system existent in the inlet generates total pressure losses, decreasing inevitably the engine efficiency. Furthermore, the flow at the air intake is significantly distorted by the large shock-induced separation of the boundary layer on the cowls and by large amplitude unsteadiness. These phenomena can be so severe that the performance of the engine can be affected drastically. In the worst scenario, highlighted by Babinsky and Harvey [2011], it can result in an engine unstart.
Fig. 1.1.1c suggests a zoom at the scale of the boundary layer, where the shock-induced separation originates. The whole SWBLI potentially exhibits a low-frequency breathing, characterised by a periodic increase and decrease of the size of the separation bubble. Although the origin of this unsteadiness defies the physical explanation of the fluid dynamics community for decades (Dolling [2001]), the breathing is generally associated to an amplification of the turbulent structures by the separation bubble.
The turbulent structures are significantly enhanced by the separated region, where the laminar-turbulent transition generally takes place in laminar SWBLI. Turbulent flows increase the friction drag and the thermal load on the aerodynamic surfaces. For the present work, we zoom in the perturbation level, that represents the smallest scales of the SWBLI (Fig. 1.1.1d), where the laminar-turbulent transition originates from the linear growth and, thereafter, from the interaction between eigenmodes of the system. The analysis of these theoretically infinitesimal modes gives the opportunity to identify the origin of the incipient turbulence and of the largest scale unsteadiness.

In the current thesis, we approach the stability of the laminar separation bubble induced by an incident shock impinging on a flat plate with BiGlobal linear stability analysis. With the rising computational power, such analyses have become possible nowadays and it is a pertinent methodology used to approach the stability problem. Nevertheless, due to the complexity of the compressible equations, stability studies of the SWBLI are almost non-existent in the literature. The present thesis aims to provide a first insight into the stability of the modes present in the SWBLI. As a baseline for the flow configuration, the experiments conducted by Giepman [2016] in the TST-27 blowdown transonic/supersonic wind tunnel of Delft University of Technology are considered.

1.2 The shock-wave/boundary-layer interaction

The occurrence of a shock-wave is characterised by an abrupt change in pressure, temperature, velocity and density such that a sharp discontinuity is generated where it appears in the flow (Courant and Friedrichs [1999]; Babinsky and Harvey [2011]). Typical situations where shocks occur are a pressure adaptation through a diverging-converging nozzle or a flow deviation at a solid boundary. Moreover, the shock can be normal, oblique or even curved in case of bluff bodies or subsonic aerofoils travelling at supersonic speed. They reflect at solid interfaces, yielding extremely complex shock patterns in high-speed internal flows. In addition, the fluid viscosity causes the development of boundary layers over the solid surfaces (Schlichting [1960]; White [1991]). Depending

on the flow conditioning such as, the Mach number, the Reynolds number, Re, or the surface roughness, the boundary layer can be laminar, transitional or turbulent (Pope [2000]; Davidson [2015]). Finally, dealing with supersonic flows over a surface yields to inevitable interactions between the shock and the boundary layer. The phenomenon is referenced by the fluid dynamics community as Shock-Wave/Boundary-Layer Interaction (SWBLI) and has been observed experimentally for the first time by Ferri [1939].

The SWBLI consists of the interaction between the viscous region (boundary layer) and the shock-waves in the supersonic flow around solid surfaces. The Mach number M, defined as the ratio between the flow velocity and the speed of sound, must be higher than the unity to observe shocks. The emphasis about the local Mach number is important to take into account transonic flows, where $M < 1$ in the freestream but reaches unity locally (Anderson [2011]). Nonetheless, in the current thesis, the transonic regime is omitted and the SWBLI with a supersonic freestream is considered.

Three basic configurations are generally considered for the study of the SWBLI; backwards facing step, compression ramp and the flat plate (Fig. 1.2.1). Although only the latter is considered in the current thesis, the basic principles of the SWBLI remain valid for the other flow configurations. Fig. 1.2.1 shows the interaction between an incident oblique shock and a developing boundary layer over a flat plate. Due to the pressure rise across the incident shock, a strong adverse pressure gradient is induced within the boundary layer around the impinging location. Due to the decrease in speed when entering the boundary layer, a slight curvature of the incoming shock is observed in this particular region. In addition, the decrease in speed implies the existence of a sonic line within the boundary layer, where the flow becomes subsonic and finally reaches zero at the wall. The subsonic region is a fundamental feature as it ensures the information to travel upstream and downstream, while supersonic regime allows only the latter. As a consequence of the strong adverse pressure gradient, an incipient separation of the boundary layer occurs upstream of the shock. The separation induces a strong deflection of the boundary layer. A reflected shock is generated as a result. On the other hand, the incident shock reflects on the sonic line, resulting in an expansion fan emerging from the top of the bubble. Consequently, the lifted shear layer is redirected towards the wall, yielding the reattachment which induces a final compression fan. Between the separation and the reattachment points, a bubble characterised by a reversed flow takes place and exhibits a near-constant pressure. Note that this physical description is based on Fig. 1.2.1, where a strong shock is considered. In case of weak interaction, the separation bubble is small and does not exhibit constant pressure. Furthermore, the compression waves at the separation coalesce with the expansion fan and the compression waves. Such arrangements are greatly detailed by Babinsky and Harvey [2011] beside several other combinations of shock strengths and flow configurations.

Up to this point, the boundary layer has been treated equally for laminar and turbulent regimes. However, it influences the behaviour of the SWBLI strongly due to the fuller boundary layer velocity profile for the latter, yielding a higher momentum close to the wall. Therefore, more energy is needed to induce a separation compared to the emptier velocity profile of the laminar boundary layer. Consequently, the turbulent

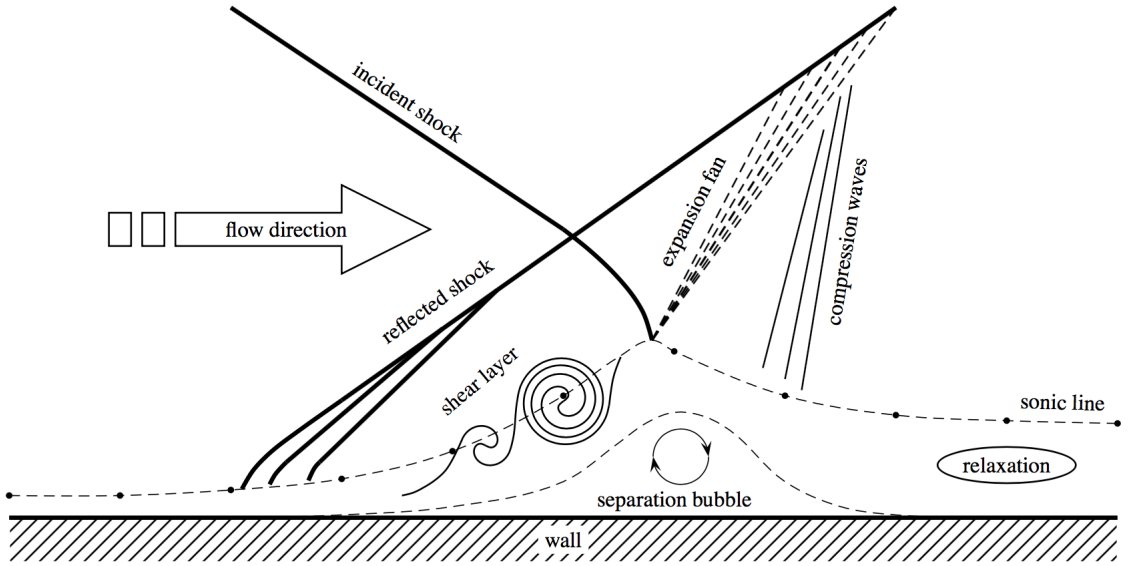

Figure 1.2.1: Schematic representation, from Touber and Sandham [2009], of a SWBLI induced by an incident shock impinging on a flat plate.

SWBLI exhibits a smaller separation bubble than the laminar equivalent. Note that the latter flow regime is difficult to maintain over the entire interaction due to the strong generation of perturbations in the shear layer across strong shocks. In general, it leads to the transition to turbulence of the boundary layer in the rear region of the bubble.

In addition to the static comportment of the SWBLI, the shock-induced separation bubble can exhibit unsteadiness. This is observed experimentally and numerically with both laminar and turbulent boundary layers. Nowadays, the origin of the unsteadiness is not well understood and two different perspectives are considered by the fluid dynamics community (Dolling [2001]; Clemens and Narayanaswamy [2014]). The first approach proposed by Ganapathisubramani et al. [2007, 2009] consists of considering the bubble as a perturbation amplifier (extrinsic mode). They argue that the low frequency unsteadiness is caused by the response of the bubble to the incoming turbulent structures. The broad frequency spectrum resulting from the amplification of the turbulent structures has been extensively studied by Touber and Sandham [2009]; Grilli et al. [2012]; Sansica et al. [2013]; Clemens and Narayanaswamy [2014]; Sansica et al. [2016]; Larchevêque [2016]; Pasquariello et al. [2017] for turbulent SWBLI. Although, such structures do not exist in laminar boundary layers, a similar approach is followed by Sansica et al. [2013, 2014, 2016]; Guiho et al. [2016], who artificially perturb the laminar SWBLI. A white noise is imposed at different regions through Direct Numerical Simulations (DNS) conducted by Sansica et al. [2013, 2014] and the dominant frequencies correspond to the growth of Kelvin-Helmholtz (KH) instabilities followed by vortex shedding in the post-shock region of the bubble. Similarly, Sansica et al. [2016] use the one-dimensional Linear Stability Theory (LST) and the linear Parabolised Stability Equations (PSE) to highlight the transition from a laminar SWBLI to a turbulent SWBLI. According to the authors, the unsteadiness is caused by a feedback mechanism of the post-shock

turbulence that induces the low-frequency motion of the separation region.

The second approach, followed by Boin et al. [2006]; Robinet [2007]; Guiho et al. [2015] with DNS and global stability analyses, consider intrinsic modes existing in the shock-induced separation bubble. Nevertheless, they used the stable configuration of Degrez et al. [1987], which does not exhibit any growth of the low-frequency unsteadiness. Guiho et al. [2015] were only able to reveal briefly the presence of extrinsic modes such as KH-like structures and Mach waves radiations, which demonstrate again the amplifier characteristic of the laminar SWBLI. On the other hand, Boin et al. [2006]; Robinet [2007] highlight for the first time the presence of a global mode in SWBLI, yielding a bifurcation towards a three-dimensional topology of the separation bubble, when the shock strength is increased. In addition, for a sufficiently large shock angle, the unsteadiness of the bubble is highlighted by DNS. However, this unsteady case is not handled by Boin et al. [2006]; Robinet [2007] with the global stability analysis and the presence of an intrinsic mode related to the bubble breathing is not revealed nowadays.

1.3 The linear stability analysis

The stability analysis is based on the linearisation of the Navier-Stokes Equations (NSE) and gains interest in the fluid dynamics community as it represents an alternative tool to the conventional methods (DNS, Large-Eddy Simulations (LES) and Reynolds Averaged Navier-Stokes (RANS)) to predict the linear regime before non-linearities occur. The DNS solve the entire NSE and consists, therefore, of the most accurate and realistic approach for solving any flow configuration. Nevertheless, as the entire underlying physics of the fluid dynamics is involved, all the turbulent structures from the largest to the smallest scales are resolved. It implies very expensive simulations in term of the computational requirements and only canonical cases can be resolved in a reasonable amount of time. On the other hand, RANS is based on modelling turbulence entirely. The flow is decomposed into mean variables and finite perturbations representing the turbulent fluctuations. Aiming to decrease the requested computational power, it leads

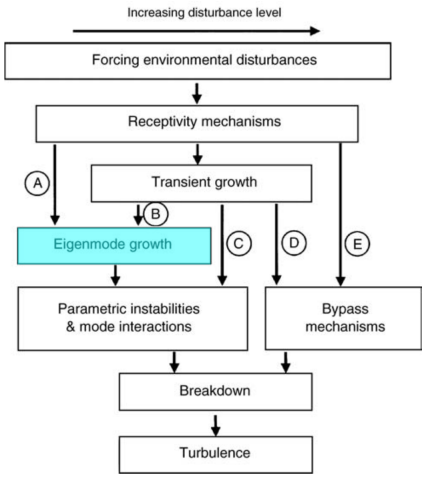

Figure 1.3.1: Schematic representation, adapted from Reshotko and Tumin [2006], of the path to turbulence breakdown.

to approximation errors depending on the approach used to evaluate the eddy viscosity (Frahnert and Dallmann [2002]), which is related to the modelling of the Reynolds stresses. For instance, RANS is not adapted for the prediction of the transition, for separated flows (separation bubbles, stalled aerofoils) or for secondary flows (backwards facing step, square pipe). Nevertheless, because of the ease to interpret the results and of the relatively low requirement of computational power, this is the most used method in the industry.
LES is located between RANS and DNS as it solves fully the largest turbulent scale, while the smallest ones are modelled. LES require less computational resources than DNS if there is no need to solve the near-wall region accurately. Notwithstanding, if wall-bounded flows are considered, the smallest structures have to be resolved to ensure realistic results and the computational time becomes similar to DNS. Although all these methods can compute or model the non-linearities of the flow, it does not make them efficient to predict the earlier linear regime.
Therefore, the linear stability analysis approach shows up as an ideal alternative to predict such a flow regime without solving the full NSE. The eigenmode growth shown in the path A[1] of Fig. 1.3.1 illustrates the all possible perturbation amplification physics considered by the linear stability theory. As the non-linearities are due to the combinations and to the interactions of linear modes, understanding the origins of the latter is essential. A characterisation of the linear modes gives the opportunity to control and to delay the transition to non-linear breakdowns, which are difficult to control afterwards, such that the friction drag can be decreased and the unsteadiness predicted.

Different types of stability equations can be derived from the linearisation of the NSE depending on the important physics to be resolved. The simplest formulation of the linear stability equations consider only the effects associated to one-dimensional boundary layer profiles and consists of the LST approach[2]. LST considers only one inhomogeneous direction (streamwise in this case), while the spanwise and wall-normal direction of the modes are assumed to be homogeneous. Through the continuity equation and the boundary conditions, it implies that the wall-normal velocity component of the flow is not included in the stability equations; the streamlines are always assumed to be parallel to the wall. In contrast, the BiGlobal stability analysis involves all the flow features in two directions and assumes only that the modes have a fixed spanwise wavelength. In case of separation bubbles which are at least two-dimensional, the BiGlobal approach must be chosen. The third dimension could be entirely resolved by the means of TriGlobal stability analysis, but this is not feasible with the computational memory available nowadays.

Although the stability analysis has been originally derived to predict the transition to turbulence without using DNS, it has the ability to reveal all the eigenmodes present in a flow before the non-linear regime. For instance, Batterson [2011] applied the methodology to bidirectional vortex, Theofilis [2017] to lid-driven cavity and Dogval et al. [1994]; Theofilis et al. [2000]; Rist and Maucher [2002]; Rist [2005]; Theofilis and

[1]The reader interested in the other non-linear paths depicted in Fig. 1.3.1 is referred to the book of Schmid and Henningson [2001] and to the article of Reshotko and Tumin [2006] for detailed descriptions.

[2]The appellation LST by the fluid dynamics community for one-dimensional problems is confusing and, as emphasized by Groot [2013], UniGlobal stability analysis would be more appropriate in the current context. Even though LST must stand only for Linear Stability Theory, the abbreviation is used in the current thesis when the one-dimensional stability equations are involved.

Colonius [2004]; Rodriguez and Theofilis [2010]; Rodriguez [2010] exploited extensively the incompressible stability equations for the analysis of different modes in the laminar separation bubbles. The application of the stability theory to compressible flows is more rare and only a few examples can be found in the literature (Boin et al. [2006]; Robinet [2007]; Guiho et al. [2015, 2016]). In addition, the exact compressible BiGlobal equations have been reported for the first time by Groot [2013].

1.4 Thesis objectives

Analysing the stability of the shock-wave/boundary-layer interaction must take into account the two-dimensionality of the phenomenon, justifying the application of the BiGlobal linear stability theory. The development and the validation of a BiGlobal solver based on the compressible formulation of the linear equations derived by Groot [2013] consist of the first objective of the thesis (chapters 2 and 3). As a part of this objective, the pressure boundary closure derived by Theofilis [2017] for incompressible problems is adapted to the present compressible solver in order to improve the quality of the stability results.

The second objective handled in chapter 4 is the stability analysis of compressible and incompressible developing boundary layers. It aims to study the effect of the method used to compute the equilibrium solution of the NSE on the BiGlobal results. The understanding of the impact of the boundary conditions and of the grid convergence on the stability results is a fundamental purpose handled in chapter 4. Furthermore, it aims at providing a first insight into the underlying physics of simple developing flows in order to acquire experience for further more complex flows. The improvement of the representation of the convective modes is a third objective of the thesis and the methodology employed is presented in chapter 4 with developing boundary layers.

The fourth objective, handled in chapter 5 of the thesis, is the analysis of the laminar shock-wave/boundary layer interaction computed with direct numerical simulations. It aims at the comparison with the experiments conducted by Giepman [2016] and with similarity laws derived from the free interaction theory to predict the wall-pressure distribution within the separation bubble. Finally, the identification of the instabilities present in the laminar shock-wave/boundary layer interaction and providing an initial analysis of their underlying characteristics is the ultimate objective of the thesis.

The overall purpose of the research work is to understand the atoms of the flows physics of developing boundary layers and of laminar shock-wave/boundary layer interactions through direct numerical simulations and the built BiGlobal tools.

2. BiGlobal Stability Solver

This chapter consists of the development of a BiGlobal stability code written in the `Matlab` language. The first section considers the different theoretical aspects to take into account regarding the stability theory in general. The derivation of the equations is not handled in the current thesis and the reader is referred to Groot [2013]; Pinna and Groot [2014].
The second part focuses on the numerical approaches followed to implement the BiGlobal stability solver. The Chebyshev and Lagrange polynomials are presented to ensure discretisation with high accuracy. In addition, two mappings of the collocation points to the physical space are handled. The concepts are used to numerically represent the stability equations in terms of a discrete eigenvalue problem. Different boundary conditions are discussed and implemented in the current solver. Finally, some brief explanations about the `Matlab` built-in eigensolver end the chapter.

2.1 Theoretical approach

From a general point of view, stability theories are based on the linearisation of the considered equations around an equilibrium state. For the unsteady Navier-Stokes Equations (NSE), the instantaneous flow is decomposed into a base flow $\overline{Q}$ and a perturbation part q' leading to:

$$Q = \overline{Q} + q'. \tag{2.1.1}$$

It is important to remark that $\overline{Q}$ is $\mathcal{O}(1)$ while the perturbations q' are $\mathcal{O}(\epsilon)$ with $\epsilon << 1$, i.e. q' are infinitesimally small as opposed to the $\overline{Q}$ and hence do not have an effect on the variables latter. The equilibrium state $\overline{Q}$ is so-called the base flow which is distinguishable from a mean flow, consisting of a statistically time averaged flow. In a mean flow, all the non-linearities are included and may not have to correspond to a proper equilibrium solution of the NSE. A differentiation has to be done between the current decomposition proposed by Eq. (2.1.1) and the Reynolds Averaged Navier Stokes (RANS) approach. While the former assumes a total decoupling between $\overline{Q}$ and q', the RANS equations consider that the fluctuation component influences the mean flow.
Regarding the stability analysis, the equations obtained by the introduction of (2.1.1) in the NSE are called the mean-plus-perturbation equations. The stability equations to be solved ultimately are obtained by subtracting the base flow equations from the mean-plus-perturbation equations and performing linearisation.

2.1.1 Stability equations

In addition to the linearisation accompanying Eq. (2.1.1), the perturbation q' is decomposed into the following modal form:

$$q' = \tilde{q} e^{(\Theta(x,y,z)-\omega t)} + c.c, \tag{2.1.2}$$

where $\Theta(x, y, z)$, ω are the complex phase in space and angular frequency, respectively. $\tilde{q}$ is the complex perturbation amplitude and the additional term $c.c$ ensures that q' remains a real quantity. The spatial feature of the modes is defined by $\Theta(x, y, z)$ where the real part gives information about the wavenumber and the imaginary part represents the spatial growth rate or, more generally, the amplitude. On the other hand, the real and the imaginary parts of ω are the frequency and the temporal growth rate, respectively.
Nowadays, the available computational power does not allow to solve three-dimensional (TriGlobal) problems with regular workstations and, therefore, the spatial directions are not all numerically resolved. It implies that one (or two) directions are spectrally (i.e. homogeneously) solved. Considering a spectral direction implies that a unique wavenumber of the modes is imposed such that the derivatives in this direction are not based on numerical differentiations. In other words, it imposes the periodicity of the modes in the direction resolved spectrally. Tab. 2.1.1 summarises the different kinds of global stability equations. Generally, the LST method solves spectrally the streamwise and the spanwise direction while the only differential direction is the wall-normal one.

Name	Perturbation	Base Flow
TriGlobal	$q' = \tilde{q}(x, y, z)e^{-i\omega t} + c.c$	3D
Streamwise BiGlobal	$q' = \tilde{q}(x, y)e^{i(\beta z-\omega t)} + c.c$	2D
Spanwise BiGlobal	$q' = \tilde{q}(y, z)e^{i(\alpha x-\omega t)} + c.c$	2D
LST	$q' = \tilde{q}(y)e^{i(\alpha x+\beta z-\omega t)} + c.c$	1D

Table 2.1.1: Global stability appellation and related modal formulation of the perturbations.

Instead of solving the entire 3D domain with the TriGlobal stability equations, the use of the BiGlobal or LST approaches on different base flows locations inside the whole domain is feasible, i.e. extracted profiles or planes of interest. The LST method is generally applied at different streamwise locations for developing flows. However, it keeps the homogeneity assumption in the streamwise direction and the base flow wall-normal velocity is not included in the problem. Therefore, the streamlines are parallel to the wall; the non-parallel effects are neglected in the stability solutions. An alternative is the use of a spatial marching instead of solving each location separately. Such methods are known as the Parabolised Stability Equations (PSE) and consist of allowing a slight amplitude change in the marching direction, essentially streamwise. It makes generally sense only for the streamwise direction the boundary layer advects perturbations in this direction, while developing at a slow rate compared to the large length scale. As the PSE are not used in the current thesis, the reader is referred to Holmes [2013] for more information. Only the streamwise and spanwise BiGlobal equations are considered in the present implementation.

In the present thesis, all variables are expressed in the temperature and pressure variables using the calorically perfect gas equation of state, expressed in terms of the base flow and perturbation variables as follows:

$$\gamma M^2 \overline{P} = \overline{\rho}\overline{T}, \qquad \gamma M^2 p' = \rho' \overline{T} + \overline{\rho} T'. \tag{2.1.3}$$

with p the pressure, T the temperature and ρ the density. The Mach number is defined by $M = \overline{U}_e / \sqrt{\gamma R \overline{T}_e}$ with R the specific gas constant, γ the specific heat's ratio and the subscript e indicative of a quantity evaluated in the freestream. On the other hand, the instantaneous transport coefficients, such as the viscosity coefficients μ and λ and the thermal conductivity k, are assumed to vary only with the temperature $\overline{T}$, yielding to:

$$\overline{\mu} = \frac{\partial \overline{\mu}}{\partial \overline{T}} \frac{\partial \overline{T}}{\partial x}, \qquad \overline{\lambda} = \frac{\partial \overline{\lambda}}{\partial \overline{T}} \frac{\partial \overline{T}}{\partial x}, \qquad \overline{k} = \frac{\partial \overline{k}}{\partial \overline{T}} \frac{\partial \overline{T}}{\partial x}, \tag{2.1.4}$$

$$\mu' = \frac{\partial \overline{\mu}}{\partial \overline{T}} T', \qquad \lambda' = \frac{\partial \overline{\lambda}}{\partial \overline{T}} T', \qquad \overline{k} = \frac{\partial \overline{k}}{\partial \overline{T}} T', \tag{2.1.5}$$

where the derivatives of the base flow transport coefficients depend only on the base flow temperature $\overline{T}$ and on the viscosity/conductivity law (Sutherland or the power law).

2.2 Numerical approach

2.2.1 Weighted residual methods

The choice of the discretisation in the BiGlobal code development is handled in order to ensure accurate results. As previously done by many authors (Robitaillié-Montané [2005]; Piot [2008]; Batterson [2011]; Pinna [2012]; Groot [2013]), the numerical discretisation is based on a pseudo-spectral method with Chebyshev polynomials. The spectral methods represent a type of weighted residual methods. It assumes that the solution of an ODE can be evaluated as a series expansion minimising the error with the exact function at the discrete nodes. A spatial (time-independent) ODE equation can be written in the general form:

$$\mathcal{A} f(\xi) = g(\xi), \qquad \xi \in [-1; 1], \tag{2.2.1}$$

where $\mathcal{A}$ could be any spatial differential operator with respect to ξ and $f(\xi)$ contains the variables. Assuming that the solution of Eq. (2.2.1) is given by a series expansion leads to

$$f(\xi) = \sum_{k=1}^{\infty} \hat{f}_{k-1} \phi_{k-1}(\xi), \qquad \xi \in [-1; 1], \tag{2.2.2}$$

under the hypothesis of homogeneous boundary conditions. In Eq. (2.2.2), both $\hat{f}_{k-1}$ (expansion coefficients) and $\phi_{k-1}(\xi)$ (basis function) have to be determined. Only a finite number of points is used, leading to the truncated series:

$$f_N(\xi) = \sum_{k=1}^{N} \hat{f}_{k-1} \phi_{k-1}(\xi), \qquad \xi \in [-1; 1]. \tag{2.2.3}$$

The residual is defined by the difference between the polynomials approximation and the exact function:

$$\mathcal{R}(\xi) := f_N(\xi) - f(\xi) \tag{2.2.4}$$

The fundamental of the weighted residual methods is to select expansion coefficients such that:

$$\int_{-1}^{+1} \mathcal{R}(\xi) w_i(\xi) d\xi = 0, \tag{2.2.5}$$

where w_i (for $i = 1, ..., N$) are test functions to determine. Amongst the different ways to verify Eq. (2.2.5), the current approach focuses only the spectral methods characterized by globally defined basis functions. In this sub-category of the weighted residual methods, the test functions can verify Eq. (2.2.5) following different approaches: Galerkin, Collocation, τ-method, Petrov-Galerkin.
According to Batterson [2011] and Pinna [2012], the collocation method is the more adapted for the eigenvalue problem of the stability analysis. Therefore, w_i is selected such that $\mathcal{R}(\xi)$ is zeroed at each collocation node ξ_i. Mathematically, this can be written:

$$\mathcal{R}(\xi_i) = 0, \tag{2.2.6}$$

which implies that the test functions should verify:

$$w_i = \delta(\xi - \xi_i) \qquad \text{with } \delta(\xi - \xi_i) = \begin{cases} 1 & \text{for } \xi = \xi_i \\ 0 & \text{for } \xi \neq \xi_i \end{cases}. \tag{2.2.7}$$

Using the conditions described by Eq. (2.2.7), the expansion coefficients $\hat{f}_k$ are determined through the set of equations:

$$f_N(\xi_i) = \sum_{k=1}^{N} \hat{f}_{k-1} \phi_{k-1}(\xi_i), \tag{2.2.8}$$

where the only unknowns are the basis functions.

For periodic problems, the basis functions could be trigonometric polynomials (Fourier series), but it is subjected to Runge oscillations if the periodicity is not strictly respected. The Chebyshev polynomials circumvent this issue, logically introduce a non-uniform grid and are able to sustain quite sharp gradients. For a detailed comparison of both methods, the reader is referred to Dutykh [2016].

2.2.2 Chebyshev and Lagrange polynomials

The Chebyshev polynomial of the first type is a solution of the Sturm-Liouville equation:

$$(1 - \xi^2) \frac{\partial T_{k-1}^2}{\partial \xi^2}(\xi) - \xi \frac{\partial T_{k-1}}{\partial \xi}(\xi) - k^2 T_{k-1} = 0, \tag{2.2.9}$$

By applying the change of variables $\xi = \cos\theta$ with $\frac{1}{d\xi} = -\frac{1}{\sin\theta}\frac{d}{d\theta}$, Eq. (2.2.9) simply becomes:

$$\frac{d^2 T_{k-1}}{d\theta^2} + (k-1)^2 T_{k-1} = 0. \tag{2.2.10}$$

The solution of Eq. (2.2.10) reads:

$$T_{k-1} = \cos((k-1)\theta), \tag{2.2.11}$$

and represents the Chebyshev polynomial of the first kind. The derivative of Eq. (2.2.11) gives:

$$\frac{dT_{k-1}}{d\theta} = (k-1)\frac{\sin((k-1)\theta)}{\sin(\theta)} = (k-1)U_{k-1}, \tag{2.2.12}$$

where U_{N-1} is defined as the Chebyshev polynomial of the second kind. Finally, considering again $\theta = \arccos(\xi)$, the polynomials become:

$$T_{k-1} = \cos((k-1)\arccos(\xi)), \qquad U_{k-1} = \frac{\sin((k-1)\arccos(\xi))}{\sin(\arccos(\xi))}, \tag{2.2.13}$$

for $\xi \in [-1, 1]$. To circumvent the limited interval of ξ where the inverse transformation is valid, mappings to the physical domain are applied and will be presented later. Introducing T_{k-1} as a basis function in Eq. (2.2.3) leads to:

$$f_N(\xi) = \sum_{k=1}^{N} \hat{f}_{(k-1)} T_{(k-1)}(\xi). \tag{2.2.14}$$

According to De Vicente et al. [2012], the orthogonality of the Chebyshev polynomials of the first kind as well as the condition represented by Eq. (2.2.7) allows writing Eq. (2.2.14) as a Lagrange interpolation:

$$f_N(\xi) = \sum_{i=1}^{N} f(\xi_i)\psi_i(\xi), \tag{2.2.15}$$

where, according to Robitaillié-Montané [2005], Batterson [2011], De Vicente et al. [2012] and Groot [2013], the Lagrange functions $\psi_i(\xi)$ correspond to:

$$\psi_i = \kappa_i(\xi) = \frac{(-1)^i}{c_i(N-1)^2}\left(\frac{1-\xi^2}{\xi-\xi_i^2}\right)\frac{dT_{N-1}}{d\xi} = \frac{(-1)^{i+1}}{c_i(N-1)^2}\left(\frac{\sqrt{1-\xi^2}}{\xi-\xi_i^2}\right)U_{N-1},$$
$$\text{with } c_i = \begin{cases} 2 & \text{for } i = 1 \text{ or } i = N \\ 1 & \text{for } 2 \leq i \leq N-1 \end{cases}. \tag{2.2.16}$$

However, inasmuch as the discretisation is to be applied with BiGlobal stability equations, the previous development is extended to a second dimension η (Groot [2013]):

$$f_{N_\xi \times N_\eta}(\xi, \eta) = \sum_{i=1}^{N_\xi}\sum_{j=1}^{N_\eta} f(\xi_i, \eta_j)\psi_{ji}(\xi, \eta) = \sum_{i=1}^{N_\xi}\sum_{j=1}^{N_\eta} f_{ji}\kappa_i(\xi)\gamma_j(\eta), \tag{2.2.17}$$

with the corresponding Lagrange functions:

$$\kappa_i(\xi) = \frac{(-1)^i}{c_i(N-1)^2}\left(\frac{1-\xi^2}{\xi-\xi_i^2}\right)\frac{dT_{N-1}}{d\xi} = \frac{(-1)^{i+1}}{c_i(N-1)^2}\left(\frac{\sqrt{1-\xi^2}}{\xi-\xi_i^2}\right)U_{N-1}, \tag{2.2.18}$$

$$\gamma_j(\eta) = \frac{(-1)^j}{c_j(N-1)^2}\left(\frac{1-\eta^2}{\eta-\eta_j^2}\right)\frac{dT_{N-1}}{d\eta} = \frac{(-1)^{j+1}}{c_j(N-1)^2}\left(\frac{\sqrt{1-\eta^2}}{\eta-\eta_j^2}\right)U_{N-1}, \tag{2.2.19}$$

$$\text{where} \quad \begin{matrix} c_i = \begin{cases} 2 & \text{for } i = 1 \text{ or } i = N_\xi \\ 1 & \text{for } 2 \leq i \leq N_\xi - 1 \end{cases} \\ c_j = \begin{cases} 2 & \text{for } j = 1 \text{ or } j = N_\eta \\ 1 & \text{for } 2 \leq j \leq N_\eta - 1 \end{cases} \end{matrix} .$$

2.2.3 Pseudo-spectral derivatives

The major advantage of the Chebyshev polynomials is to evaluate the derivatives of Eq. (2.2.17) as follows:

$$\frac{\partial f_{N_\xi \times N_\eta}(\xi,\eta)}{\partial \xi} = \sum_{i=1}^{N_\xi}\sum_{j=1}^{N_\eta} f_{ji}\frac{\partial \kappa_i(\xi)}{\partial \xi}\gamma_j(\eta), \tag{2.2.20}$$

$$\frac{\partial f_{N_\xi \times N_\eta}(\xi,\eta)}{\partial \eta} = \sum_{i=1}^{N_\xi}\sum_{j=1}^{N_\eta} f_{ji}\kappa_i(\xi)\frac{\partial \gamma_j(\eta)}{\partial \eta}, \tag{2.2.21}$$

which can be written:

$$\frac{\partial f_{N_\xi \times N_\eta}(\xi,\eta)}{\partial \xi} = \sum_{i=1}^{N_\xi}\sum_{j=1}^{N_\eta}\sum_{m=1}^{N_\xi} f_{jm1}D_{\xi,mi}\kappa_i(\xi)\gamma_j(\eta), \tag{2.2.22}$$

$$\frac{\partial f_{N_\eta \times N_\eta}(\xi,\eta)}{\partial \eta} = \sum_{i=1}^{N_\xi}\sum_{j=1}^{N_\eta}\sum_{m=1}^{N_\eta} {}_1D_{\eta,jm}f_{mi}\kappa_i(\xi)\gamma_j(\eta), \tag{2.2.23}$$

such that the derivatives are computed by multiplying the discrete function f with the coefficients:

$${}_1D_\xi = \begin{cases} {}_1D_{\xi,11} = \frac{2(N_\xi-1)^2+1}{6} & \\ {}_1D_{\xi,ii} = -\frac{\xi_i}{2(1-\xi_i^2)} & \text{for } i = 2,...,N_\xi - 1 \\ {}_1D_{\xi,im} = \frac{c_i}{c_m}\frac{(-1)^{i+m}}{\xi_i-\xi_j} & \text{for } i \neq m \quad i,m = 2,...,N_\xi - 1 \\ {}_1D_{\xi,N_\xi N_\xi} = -\frac{2(N_\xi-1)^2+1}{6} & \end{cases} , \tag{2.2.24}$$

where the subscript 1 indicates a one dimensional formulation of the matrix:

$${}_1D_\xi = \left[\begin{array}{c|ccc|c} \frac{2(N_\xi-1)^2+1}{6} & \cdots & 2\frac{(-1)^{1+m}}{1-\xi_m} & \cdots & \frac{1}{2}(-1)^{1+N_\xi} \\ \hline \vdots & \ddots & \cdots & \frac{(-1)^{i+m}}{\xi_i-\xi_m} & \vdots \\ \frac{1}{2}\frac{(-1)^{i+1}}{\xi_i-1} & \vdots & -\frac{\xi_i}{2(1-\xi_m^2)} & \vdots & \frac{(-1)^{i+N_\xi}}{\xi_i+1} \\ \vdots & \frac{(-1)^{i+m}}{\xi_i-\xi_m} & \cdots & \ddots & \vdots \\ \hline -\frac{1}{2}(-1)^{N_\xi+1} & \cdots & 2\frac{(-1)^{N_\xi+m}}{1+\xi_m} & \cdots & -\frac{2(N_\xi-1)^2+1}{6} \end{array}\right] . \tag{2.2.25}$$

This is the pseudo-spectral differentiation matrix (Batterson [2011]). To be complete, Eq. (2.2.24) and Eq. (2.2.25) have to be extended in the other direction, η, but this is not shown in full for sake of brevity. The matrix Eq. (2.2.25) and its analogue for η are simply used as a coefficient matrices to compute the derivatives of the function $f_{N_\xi \times N_\eta}$ at the collocation nodes. A `Matlab` suite for collocation methods has been implemented by Weideman and Reddy [2000] to efficiently obtain the numerical representation of Eq. (2.2.25).

2.2.4 Vector and matrix representation

In the previous sections, all the mathematical development are based on the matrix form of the function $f_{N_\xi \times N_\eta}$. However, in order to solve ultimately an eigenvalue problem, $f_{N_\eta \times N_\eta}$ should be written in stack-column vector form. The different columns of $f_{N_\eta \times N_\eta}$ are concatenated to construct a vector as follows:

$$f_{N_\eta \times N_\eta} = \begin{bmatrix} f_{11} & f_{12} & \dots & f_{1N_\xi} \\ f_{21} & f_{22} & & \vdots \\ \vdots & & \ddots & \vdots \\ f_{N_\eta 1} & \dots & \dots & f_{N_\eta N_\xi} \end{bmatrix} \Longrightarrow f_{N_\eta \times N_\eta} = \begin{bmatrix} f_{11} \\ \vdots \\ f_{N_\eta 1} \\ f_{12} \\ \vdots \\ f_{N_\eta 2} \\ \vdots \\ f_{1N_\xi} \\ \vdots \\ f_{N_\eta N_\xi} \end{bmatrix}, \tag{2.2.26}$$

The pseudo-spectral differentiation matrix (Eq. (2.2.25)) has to be adapted in a same way. This transformation is handled by considering the Kronecker product, defined on arbitrary matrices $A_{m\times n}$ and $B_{p\times q}$ as follows:

$$A_{m\times n} \otimes B_{p\times q} = \begin{bmatrix} a_{11}B & \dots & a_{1n}B \\ \vdots & \ddots & \vdots \\ a_{m1}B & \dots & a_{mn}B \end{bmatrix} = C_{nq\times mp}, \tag{2.2.27}$$

According to Eq. (2.2.27), the pseudo-spectral differentiation matrices become:

$$D_\xi = {}_1D_\xi \otimes I_{N_\eta}, \qquad D_\eta = I_{N_\xi} \otimes {}_1D_\eta, \tag{2.2.28}$$

$$D_\xi = {}_1D_\xi \otimes I_{N_\eta}, \qquad D_\eta = I_{N_\xi} \otimes {}_1D_\eta, \qquad D_{\xi\eta} = {}_1D_\xi \otimes {}_1D_\eta, \tag{2.2.29}$$

with the I_{N_ξ} and I_{N_η} identity matrices of sizes $N_\xi \times N_\xi$ and $N_\eta \times N_\eta$, respectively. Fig. 2.2.1a, 2.2.1b and 2.2.1c show the non-zero elements of the differential matrices, with $N_\xi = N_\eta = 5$ collocation nodes.

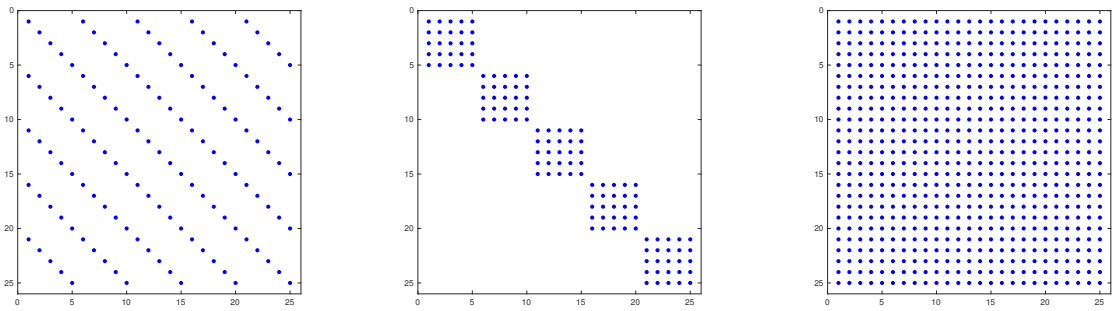

(a) D_ξ and $D_{\xi\xi}$ (b) D_η and $D_{\eta\eta}$ (c) $D_{\xi\eta}$

Figure 2.2.1: Non-zero coefficients of the pseudo-spectral differentiation matrices with $N_\xi = N_\eta = 5$.

2.2.5 Mapping to physical space

The Chebyshev polynomials have been derived by considering only a square domain $[-1, 1] \times [-1, 1]$. To represent other domain types, mapping methods are used. In the current thesis, two mappings are considered.

Bi-linear mapping

A first mapping is proposed by Malik [1990] and has been extensively used by Piot [2008]; Pinna [2012]; Groot [2013]. It reads:

$$y = \frac{y_i y_{max}(1+\eta)}{y_{max} - \eta(y_{max} - 2y_i)}, \tag{2.2.30}$$

with y the wall-normal direction in the physical space $[0, y_{max}]$. The same formula can be applied for the mapping in the x-direction. The coordinate y_i represents mapping half of the points in $[0, y_i]$ and the other half in $[y_i, y_{max}]$. For semi-infinite problem, where y_{max} tends to infinity, it becomes:

$$y = \frac{y_i(1+\eta)}{1-\eta}. \tag{2.2.31}$$

If y_i is equal to $y_{max}/2$, Eq. (2.2.30) degenerates into:

$$y = \frac{y_{max}}{2}(1+\eta), \tag{2.2.32}$$

which implies a uniform repartition of the collocation points.

Bi-quadratic mapping

The second mapping, developed by Groot et al. [2017], divides the domain into three refinement regions. In the current thesis, where SWBLI is ultimately studied, particular refinements are needed to resolve the shock and the bubble in the x-direction. It justifies the use of the bi-quadratic mapping, which reads:

$$y = y_{max}\frac{a\eta^2 + b\eta + c}{d\eta^2 + e\eta + cf}, \qquad \text{with} \begin{cases} a = & (y_{i2} - 3y_{i1}) \\ b = & 1.5(y_{i2} - y_{i1}) \\ c = & 0.5(y_{i2} + 3y_{i1}) \\ d = & 2(2y_{i2} - 2y_{i1} - y_{max}) \\ e = & 0 \\ f = & 2y_{max} - y_{i2} + y_{i1} \end{cases}, \tag{2.2.33}$$

where the values y_{i1} and y_{i2} have to be selected such that $0 < y_{i1} < y_{i2} < y_{max}$, $y_{i2} < 9y_{i1}$ and $9y_{i2} < y_{i1} + y_{max}$ to avoid discontinuities and mapping outside the physical domain $[0, y_{max}]$. The bi-quadratic mapping separates the domain in to three parts ($[0, y_{i1}]$, $[y_{i1}, y_{i2}]$ and $[y_{i2}, y_{max}]$), each containing one third of the collocation nodes. The cosine distribution is (globally) maintained near the boundaries, so avoiding the Runge phenomenon.

Mapping and pseudo-spectral differentiation matrices

The mapping functions are finally taken into account to compute the coefficients of the pseudo-spectral differentiation matrices acting in the physical space of interest. Using the chain rule for the wall-normal direction leads to:

$$\frac{\partial f}{\partial y} = \frac{d\eta}{dy}\frac{\partial f}{\partial \eta}, \tag{2.2.34}$$

which could be written as:

$${}_1D_y = {}_1T_y^{\eta}\ {}_1D_{\eta}, \tag{2.2.35}$$

where ${}_1T_y^{\eta}$ is the discrete analogue of $d\eta/dy$ used to scaled the derivatives. Considering again the form to be applied to the stack-column representation, Eq. (2.2.35) becomes:

$$D_y = T_y^{\eta} D_{\eta} = (\ {}_1T_y^{\eta} \otimes I_{N_\xi}\ )(\ {}_1D_{\eta} \otimes I_{N_\xi}\ ) = (\ {}_1T_y^{\eta}\ {}_1D_{\eta} \otimes I_{N_\xi}\ ), \tag{2.2.36}$$

Finally, the full discretisation process is handled by extending Eq. (2.2.36) to the x-direction as well as to the other derivatives (Eq. (2.2.28) and Eq. (2.2.29)).

2.2.6 The eigenvalue problem

From a general point of view, the eigenvalue problem of the stability equations can be written as:

$$A\Xi = \lambda B\ \Xi + \lambda^2 B_2\ \Xi, \tag{2.2.37}$$

with Ξ an eigenvector and λ the corresponding eigenvalue. The latter can be either a complex spatial wavenumber (α or β) or a complex frequency ω, depending on the kind of stability problem solved. The matrices A and B are the amplitude coefficient matrices corresponding to the stability equations derived by Groot [2013]. In the present thesis, the temporal features are of main interest and Eq. (2.2.37) degenerates into:

$$A\Xi = \omega B\ \Xi, \tag{2.2.38}$$

simply due to the linearity of the stability equations with respect to ω. The eigenvector Ξ represents the different perturbation variables, expressing the thermodynamics in the temperature and pressure variables $(\tilde{T}, \tilde{p})$. Therefore, Ξ has the form:

$$\Xi = \begin{bmatrix} \tilde{u} \\ \tilde{v} \\ \tilde{w} \\ \tilde{T} \\ \tilde{p} \end{bmatrix}, \tag{2.2.39}$$

where each component is a vector of size $N_\eta N_\xi$. Dealing with compressible stability equations, other combinations of thermodynamics variables are possible such as $(\tilde{\rho}, \tilde{T})$, $(\tilde{\rho}, \tilde{p})$ using the calorically perfect gas equation of state.

The amplitude coefficient matrices for temporal compressible stability analysis reads:

$$A = \begin{bmatrix} \mathcal{L}_1^{\tilde{u}} & \mathcal{L}_1^{\tilde{v}} & \mathcal{L}_1^{\tilde{w}} & \mathcal{L}_1^{\tilde{T}} & \mathcal{L}_1^{\tilde{p}} \\ \mathcal{L}_2^{\tilde{u}} & \mathcal{L}_2^{\tilde{v}} & \mathcal{L}_2^{\tilde{w}} & \mathcal{L}_2^{\tilde{T}} & \mathcal{L}_2^{\tilde{p}} \\ \mathcal{L}_3^{\tilde{u}} & \mathcal{L}_3^{\tilde{v}} & \mathcal{L}_3^{\tilde{w}} & \mathcal{L}_3^{\tilde{T}} & \mathcal{L}_3^{\tilde{p}} \\ \mathcal{L}_4^{\tilde{u}} & \mathcal{L}_4^{\tilde{v}} & \mathcal{L}_4^{\tilde{w}} & \mathcal{L}_4^{\tilde{T}} & \mathcal{L}_4^{\tilde{p}} \\ \mathcal{L}_5^{\tilde{u}} & \mathcal{L}_5^{\tilde{v}} & \mathcal{L}_5^{\tilde{w}} & \mathcal{L}_5^{\tilde{T}} & \mathcal{L}_5^{\tilde{p}} \end{bmatrix}, \qquad B = \begin{bmatrix} \mathcal{R}_1^{\tilde{u}} & 0 & 0 & 0 & 0 \\ 0 & \mathcal{R}_2^{\tilde{v}} & 0 & 0 & 0 \\ 0 & 0 & \mathcal{R}_3^{\tilde{w}} & 0 & 0 \\ 0 & 0 & 0 & \mathcal{R}_4^{\tilde{T}} & \mathcal{R}_4^{\tilde{p}} \\ 0 & 0 & 0 & \mathcal{R}_5^{\tilde{T}} & \mathcal{R}_5^{\tilde{p}} \end{bmatrix}, \tag{2.2.40}$$

where the subscripts 1, 2 and 3 are, respectively, referencing to x-, y-, z-momentum equations while 4 and 5 stand for the continuity and the energy equations. $\mathcal{L}$ or $\mathcal{R}$ correspond to the coefficients in stability equations, while the superscripts indicate the variable they multiply. Up to this point, the matrices A and B depend only on the base flow. The boundary conditions have to be imposed for the five perturbations variables at the four boundaries of the domain.

2.2.7 Boundary and compatibility conditions

Having an infinite domain would be the perfect condition to represent a natural phenomenon, but it is impossible to represent discretely. It implies that the domain used should be finite and boundary conditions have to be chosen.
The boundary conditions replace the governing equations at the boundary nodes of the domain. Note that any eigenvalue problem is homogeneous in the sense that there is no forcing term and therefore, all the boundary conditions should verify this property as needed as well for the collocation method. The detailed theoretical foundations about the boundary conditions can be found in the master thesis of Groot [2013]. The current section briefly handles their implementation in the BiGlobal tools. An exception is made for the linearised pressure Poisson equation (LPPE) initially derived by Theofilis [2017] for the incompressible stability equations. A detailed derivation of the LPPE is handled in the current section for the compressible stability equations. The effect on the results is analysed in chapter 4 beside the stability of developing compressible and incompressible boundary layers.

Homogeneous Dirichlet condition

Applying on a variable the Dirichlet conditions consists of imposing zero at the considered boundary. It is an essential feature to represent the no-slip condition at a solid wall. According to Groot [2013], imposing such a condition in the present eigenvalue problem consists of setting 1 in the amplitude coefficient matrix A at the location of the boundary and imposing 0 elsewhere for the corresponding variable, including in B.

Homogeneous Neumann condition

The Neumann condition specifies a variable to have zero normal derivative at the boundary. This condition involves, therefore, coefficients in differentiation matrices. For the B matrix, it simply corresponds to set 0 at the location of the boundary, while for the matrix A, the coefficients from the stability equations are overwritten by the pseudo-spectral differentiation matrices D_ξ or D_η.

Pressure Compatibility (PC) condition

The solid boundary closure for the pressure is an issue encountered when solving flow problems and thus as well for the linear stability problem on a collocated grid. Although the no-slip condition logically extrapolates to velocity and temperature perturbations, there is no such condition for the pressure. Different closures are commonly applied. A widely used boundary closure variant is the PC equation, based on evaluating a momentum equation at the wall. The resulting equation relates the first order wall-normal derivative of the pressure to (higher order derivatives of) the velocity and temperature variables. Considering a streamwise BiGlobal stability problem, where the top and bottom boundaries are a solid-wall, the PC closure is derived by using the y-momentum equation with enforcing the no-slip and isothermal condition ($\tilde{u} = \tilde{v} = \tilde{w} = \tilde{T} = 0$) through Dirichlet condition. Therefore, the PC closure reads:

$$\begin{aligned}
&\left[\frac{\gamma M^2 \overline{V}\,\overline{V}_y}{\overline{T}} + \frac{\gamma M^2 \overline{U}\,\overline{V}_x}{\overline{T}} + \frac{\partial}{\partial y}\right]\tilde{p} \\
&= \left[\frac{\overline{\mu}_{\overline{T}}\,\overline{T}_x}{Re}\frac{\partial}{\partial y} + \frac{\overline{\mu}}{Re}\frac{\partial^2}{\partial x \partial y} + \frac{\overline{\lambda}}{Re}\frac{\partial^2}{\partial x \partial y}\right]\tilde{u} \\
&+ \left[-\frac{\gamma M^2 \overline{P}\,\overline{V}}{\overline{T}}\frac{\partial}{\partial y} + \frac{2\,\overline{\mu}_{\overline{T}}\,\overline{T}_y}{Re}\frac{\partial}{\partial y} + \frac{\overline{\lambda}_{\overline{T}}\,\overline{T}_y}{Re}\frac{\partial}{\partial y} + \frac{2\,\overline{\mu}}{Re}\frac{\partial^2}{\partial y^2} + \frac{\overline{\lambda}}{Re}\frac{\partial^2}{\partial y^2}\right]\tilde{v} \\
&+ \left[\frac{i\,\beta\,\overline{\mu}}{Re}\frac{\partial}{\partial y} + \frac{i\,\beta\,\overline{\lambda}}{Re}\frac{\partial}{\partial y}\right]\tilde{w} \\
&+ \left[\frac{2\,\overline{\mu}_{\overline{T}}\,\overline{V}_y}{Re}\frac{\partial}{\partial y} + \frac{\overline{\lambda}_{\overline{T}}\,\overline{V}_y}{Re}\frac{\partial}{\partial y} + \frac{\overline{\lambda}_{\overline{T}}\,\overline{U}_x}{Re}\frac{\partial}{\partial y}\right]\tilde{T}.
\end{aligned} \tag{2.2.41}$$

This boundary closure does not introduce independent information for the pressure (Rempfer [2006]) and it causes strongly oscillatory spurious modes which can affect physical modes by displaying comparable oscillations. To circumvent the issue, Theofilis [2017] derives the LPPE for the incompressible stability equations and it effectively removes the spurious mode. Consequently, an adaptation of the LPPE for compressible flow is derived in the current thesis.

Linearised Pressure Poisson Equation (LPPE)

The LPPE is used at boundaries where the no-slip condition causes the flow to approach the incompressible limit. This justifies using the incompressible Poisson equation as a boundary condition for the pressure, when accounting for the appropriate thermodynamic properties. Following Theofilis [2017], the Poisson equation for the instantaneous flow reads:

$$\frac{\partial^2 p}{\partial x_i \partial x_i} = -\rho \frac{\partial}{\partial x_i}\left(u_k \frac{\partial}{\partial x_k}\right) u_i. \tag{2.2.42}$$

where p is the pressure, u_i are the velocity components and x_i the coordinates ($x_1 = x$, $x_2 = y$, $x_3 = z$). As a result, the LPPE for a no-slip condition at a boundary $y = \text{const}$ becomes:

$$\begin{aligned}\left[\frac{\partial^2}{\partial x^2} + \frac{\partial^2}{\partial y^2} - \beta^2 + \frac{\gamma M^2}{\overline{T}}\left(2\,\overline{U}_y\,\overline{V}_x + \overline{U}_x^2 + \overline{V}_y^2\right)\right]\tilde{p} \\ = -2\frac{\gamma M^2 \overline{P}}{\overline{T}}\left[\overline{V}_x \frac{\partial}{\partial y}\right]\tilde{u} \\ -2\frac{\gamma M^2 \overline{P}}{\overline{T}}\left[\overline{V}_y \frac{\partial}{\partial y}\right]\tilde{v}.\end{aligned} \tag{2.2.43}$$

2.2.8 Practical implementation

Considering the previous concepts, the matrices A and B, where the boundary conditions are included, are built. In order to solve any kind of temporal BiGlobal stability problem, the matrices are generated in four steps illustrated in Fig. 2.2.2. In this example, only A is handled for sake of clarity; the matrix B is similarly built. For this illustrative case, the Neumann condition is imposed for all the variables at inlet/outlet while the no-slip condition is imposed for the top and bottom boundaries beside the PC closure for the pressure. Therefore, according to Fig. 2.2.2, the different steps consist of:

- (a) The base flow is interpolated on the Chebyshev collocation node and the matrices A and B are filled with the coefficients in front of each variable in the BiGlobal stability equations.
- (b) All the boundary nodes are zeroed without considering the type of boundary conditions to be applied later on.
- (c) The values of the boundary conditions are imposed in the A matrix. The red dots correspond to coefficients set to 1 for Dirichlet conditions. The green dots are the corresponding coefficients of the pseudo-spectral differentiation matrices D_ξ or D_η where the Neumann conditions are applied. In matrix B, the coefficients at the boundaries remain zero.
- (d) The PC boundary closure is imposed for the pressure in matrix A and B. The y-momentum equation at the boundaries is shifted in A and B to lie beside the energy equation. It is equivalent to impose Eq. (2.2.41), but it consists a more systematic application of the boundary conditions. The same is applicable regarding the x-momentum equation, if the inlet/outlet needs the closure for the pressure as well.

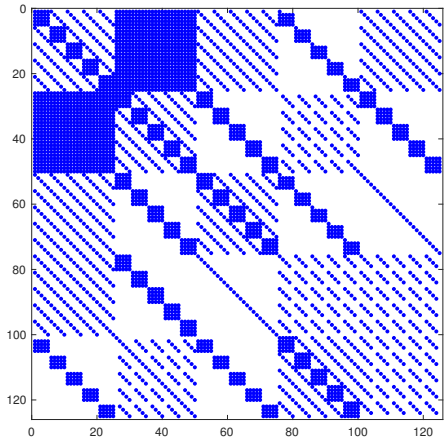

(a) Full matrix with all the coefficient of BiGlobal stability equations.

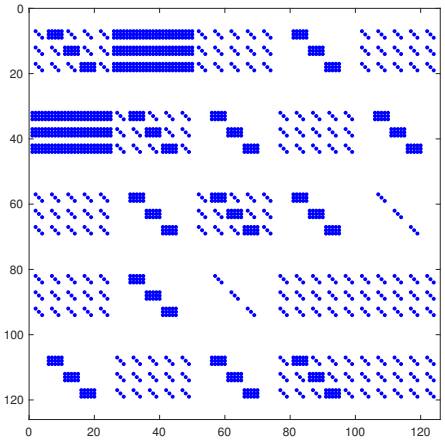

(b) Matrix without the boundary collocation nodes.

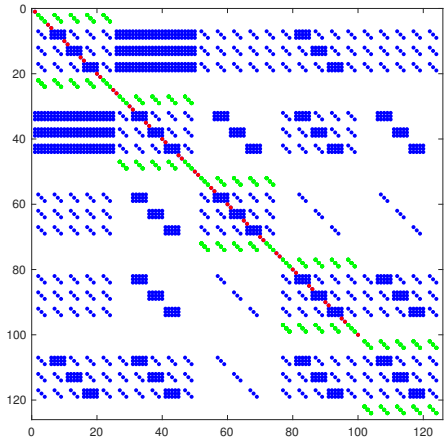

(c) Matrix with Dirichlet condition (except $\tilde{p}$) at $y = 0, y_{max}$ (red) and Neumann condition (all variables) at $x = 0, x_{max}$.

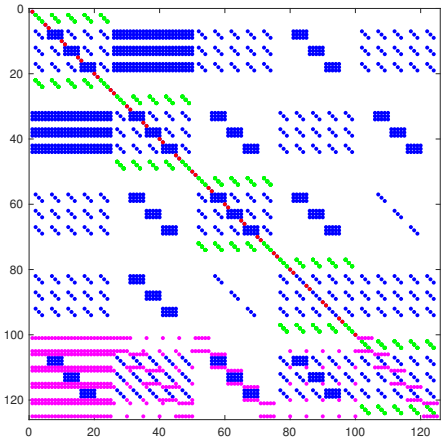

(d) Final matrix with PC boundary closure at $y = 0, y_{max}$ (magenta).

Figure 2.2.2: Construction of the matrix A with $[N_\xi, N_\eta] = [5, 5]$.

Finally, the eigenvalue problem can be solved for the two matrices A and B. It can be remarked that the size of the matrices is already significant (125×125) for a very simple illustrative case $[N_\xi \times N_\eta] = [5 \times 5]$.

2.2.9 Solving the eigenvalue problem

Two widely used algorithms, the QZ and Arnoldi algorithms, are available through the ARPACK and LAPACK routines, and offer the possibility to solve the current large eigenvalue problems. From a general point of view, the two methods do not give the same accuracy and the eigenvalue problem is treated in a very different way. The QZ-algorithm (function `eig` in `Matlab`) is a direct method which solves the entire problem and delivers all the eigenvalues with their corresponding eigenfunctions. On the other

hand, the Arnoldi algorithm (function `eigs` in `Matlab`) is an iterative method based on the formation of a Krylov subspace, which needs an initial eigenvector to compute a certain amount of eigenvalues close to it. It has the advantage to be fast as it provides only the required number of eigenvalues instead of solving the entire problem. In stability theory, the region where the most unstable modes are located is generally close to the origin in the half-plane of positive real parts and the initial value for the iterative method can be easily selected.
On the other hand, it is important to note that the eigensolvers have a limited accuracy, which is relevant to identify for both algorithms in order to track eventual accuracy lacks in the stability solution. The QZ-algorithm is capable of solving the eigenvalue problem with an accuracy (Anderson et al. [2012]) up to:

$$\epsilon_{crit}^{QZ} = \epsilon_m \max(\|A\|_F, \|B\|_F), \tag{2.2.44}$$

where $\|A\|_F$ and $\|B\|_F$ denote the Frobenius norm of the matrices A and B. Moreover, ϵ_m stands for the machine precision, generally about 10^{-16}. All the solutions below the ϵ_{crit} should be considered with care as it reaches the edge of the solver accuracy. For the current compressible stability problem, the observed ϵ_{crit} is about 10^{-12}. According to Lehoucq et al. [2012], the accuracy of the Arnoldi algorithm reads:

$$\epsilon_{crit}^{Arnoldi} = \epsilon_m |\omega|, \tag{2.2.45}$$

where ω is a complex eigenvalue computed by the eigensolver. Dealing with temporal stability, ω is generally small and therefore the accuracies of the two algorithms are indistinguishable. In the current thesis, the Arnoldi algorithm is mainly used for the streamwise stability problems due to extremely large matrices A and B.

3. Parallel Blasius Boundary Layer

The parallel (non-developing) boundary layer profile is a case for which the stability has been well studied by many authors during the past decades and represents a relatively simple case to validate the BiGlobal code. A first analysis consists of a supersonic flat plate boundary layer profile for which the only velocity component of the boundary layer is exactly aligned with the streamwise direction. The second analysis is conducted using a low Mach number Blasius profile to demonstrate the ability of the compressible BiGlobal code to solve very low subsonic cases. A third case is analysed by using the former supersonic parallel flow where a spanwise component of the base flow velocity, $\overline{W}$, is added, implying that the direction of the flow is not aligned with the streamwise direction. The velocity $\overline{W}$ is added to the base flow such that the direction of the flow is perpendicular to the wave front of the most unstable mode, minimising the number of nodes required to represent the mode structure in the plate parallel direction. Conducting such a rotation involves other terms of the stability equations, but the most unstable mode showing up is exactly the same as for the streamwise case, allowing a direct verification. For all the cases, a convergence analysis is performed in both directions. The current results are finally compared with stability analyses carried out by Mack [1976], Malik [1990], Pinna [2012] and Groot [2013].

3.1 Numerical set-up of the base flows

The profiles of both compressible and incompressible boundary layers have been computed by Groot [2013] with a fourth-order Runge-Kutta shooting method. The base flows are computed such that the residual is below the critical epsilon of the eigenvalue problems leading to 10^4 points for the incompressible profile while the compressible case comprises 3.2×10^6 points. On the other hand, as the considered cases consist of parallel Blasius flows, only one of each compressible and incompressible profile is computed and is duplicated in the spanwise direction in order to create two-dimensional base flows for BiGlobal analysis. The self-similar compressible Blasius boundary layers can be evaluated, according to White [1991], with the set of equations

$$\begin{cases} (cf'')' + ff'' & = 0 \\ (\frac{c}{Pr}g')' + fg' + (\gamma - 1)M^2 cf''^2 & = 0, \end{cases} \tag{3.1.1}$$

coupled with the boundary conditions

$$\text{for } f: \begin{cases} f'(0) = 0 \\ f(0) = 0 \\ \lim_{\eta\to\infty} f'(\eta) = 1, \end{cases} \qquad \text{for } g: \begin{cases} g'(0) = 0 \\ \\ \lim_{\eta\to\infty} g(\eta) = 1, \end{cases} \tag{3.1.2}$$

and considering the superscript d indicates dimensional variables

$$\begin{cases} f'(\eta) = \frac{df(\eta)}{d\eta} = \frac{\overline{U}^d(\eta)}{\overline{U}_e^d} \\ g(\eta) = \frac{\overline{h}^d(\eta)}{\overline{h}_e^d} \\ c = \frac{\overline{\rho}^d \overline{\mu}^d}{\overline{\rho}_e^d \overline{\mu}_e^d} \\ \xi(x^d) = \int_0^{x^d} \overline{\rho}^d \overline{U}_e^d \overline{\mu}_e^d d\tilde{x}^d \\ \eta(x^d, y^d) = \frac{\overline{U}_e^d}{\sqrt{2\xi}} \int_0^{y^d} \overline{\rho}^d d\tilde{y}^d \end{cases} . \tag{3.1.3}$$

The thermodynamic quantities are evaluated assuming a calorically perfect gas and therefore, the density and the enthalpy can be expressed in terms of the other variables:

$$\gamma M^2 \overline{P} = \overline{\rho}\overline{T}, \qquad \overline{h} = c_p \overline{T}, \tag{3.1.4}$$

where c_p is the heat capacity ratio at constant pressure. On the other hand, the Lamé's second viscosity parameter (dynamic viscosity) $\overline{\mu}$ and the thermal conductivity are evaluated with the Sutherland law as follows:

$$\overline{\mu}^d = C \frac{(\overline{T}^d)^{3/2}}{\overline{T}^d + S}, \qquad \overline{k} = \frac{c_p \mu}{Pr}, \tag{3.1.5}$$

where $Pr = 0.7$ is a constant Prandtl number and the temperature is in Kelvin. The Sutherland constant are defined as $S = 110.4\text{K}$ and $C = 1.458 \times 10^{-6} \ \frac{\text{kg}}{\text{ms}\sqrt{\text{K}}}$. Moreover, Stokes hypothesis is considered for the Lamé's first viscosity parameter $\overline{\lambda} = -\frac{2}{3}\overline{\mu}$.

3.2 BiGlobal stability analysis

3.2.1 Streamwise parallel Blasius

The BiGlobal stability analysis is carried out on a compressible and an incompressible boundary layer. In Tab. 3.2.1, the mean flow data is summarised. The velocity components $\overline{U}_e$, $\overline{V}_e$ and $\overline{W}_e$ at the edge of the boundary layer show that the base flow velocity is strictly aligned in the streamwise direction. A convergence with respect to the variables y_i and y_{max} used for the mapping of Malik [1990] has been done by Groot [2013] to show the influence of the domain truncation on the stability results. Selecting $y_{max} = 283$, the domain is sufficiently high to have a proper representation of the decay of the most unstable mode in the freestream. Additionally, y_i is chosen so to impose a high resolution near the wall. Generally, for boundary layer cases, y_i is about δ_{99}, such that half of the collocation points are mapped into the boundary layer while the other half is in the freestream.
For both wall and freestream boundaries, the Dirichlet condition is imposed for the velocity and temperature variables while the compatibility condition is applied for pressure. Concerning the spanwise boundaries, the symmetry is enforced, according to Piot [2008] who suggested the Neumann condition for all the variables except for the spanwise velocity perturbations where Dirichlet is enforced ($\tilde{w} = 0$). For the present temporal

BiGlobal stability analysis, the streamwise direction is assumed to be spectral (real wavenumber α). The values of α for both cases is set according to Malik [1990], Pinna [2012] and Groot [2013]. The aim is to analyse an unstable Tollmien-Schlichting mode which is represented, for parallel Blasius flow, by a unique discrete eigenvalue. Tab. 3.2.1 shows that for the incompressible case, the TS mode has an infinite spanwise wavelength ($\beta = 0$) while the compressible case assumes an oblique TS wave. In this section, this mode is especially analysed beside convergence analyses of the results to ensure accurate comparison with external results for the code validation. For a deep analysis of several other modes present in the parallel Blasius flows, the reader is referred to the master thesis of Groot [2013].

M	Re	$\overline{U}_e$	$\overline{V}_e$	$\overline{W}_e$	β	α	y_i	y_{max}
2.5	3000	1	0	0	0	0.06	6	283
10^{-6}	580	1	0	0	0	0.179	10	283

Table 3.2.1: Parameters of the BiGlobal set-up for the streamwise parallel Blasius.

For the stability analysis, the lengths are scaled with respect to the Blasius length l and the reference Reynolds number is based on l as well.

Convergence analysis

In Fig. 3.2.1 and Fig. 3.2.2, the convergence of the spectra with respect to different numbers of collocation points in the wall normal direction η and the spanwise direction ξ is shown, respectively. Different features can be distinguished when a continuous branch, a discrete mode or even a purely numerical mode is considered. In Fig. 3.2.1, the discrete modes have a higher convergence rate than the continuous ones; it is almost impossible to distinguish the former when N_η is increased. Tab. 3.2.2 shows the convergence of the real and the imaginary parts of the Tollmien-Schlichting wave. For N_η larger than 110, both parts of the complex $\omega l/\overline{U}_e$ are converged to the ϵ_{crit} and it is therefore not useful to increase the number of collocation points in this direction. As depicted by Tab. 3.2.3, the most unstable mode is also converged in the z-direction when $N_\xi = 15$. Moreover, Fig. 3.2.2 shows that when N_ξ is increased, a branch extends from the Tollmien-Schlichting mode towards the branch of vorticity modes corresponding to higher harmonics. It consists of a cluster of discrete modes related to the most unstable one. The higher the number of points in the spanwise direction, more and more harmonics of the TS mode are resolved.

The spurious modes, observable in all spectra for the current parallel Blasius, are purely numerical and do not represent any physical phenomenon. They come from the PC boundary closure imposed at the wall and the freestream. Fig. 3.2.1 and Fig. 3.2.2 show clearly a linear divergence of the modes when N_η is increased. On the other hand, an increasing N_ξ adds even more spurious mode. Due to their lack of physical meaning, the spurious modes should be avoided. Using other boundary conditions for the pressure circumvents the issue. For instance, applying Neumann conditions at the freestream boundary does not reveal the presence of these modes. However, the decay of the modes of interest should be taken into account. Imposing Neumann on the perturbations components enforces indeed the decay/growth of the modes at the boundaries. In section 4

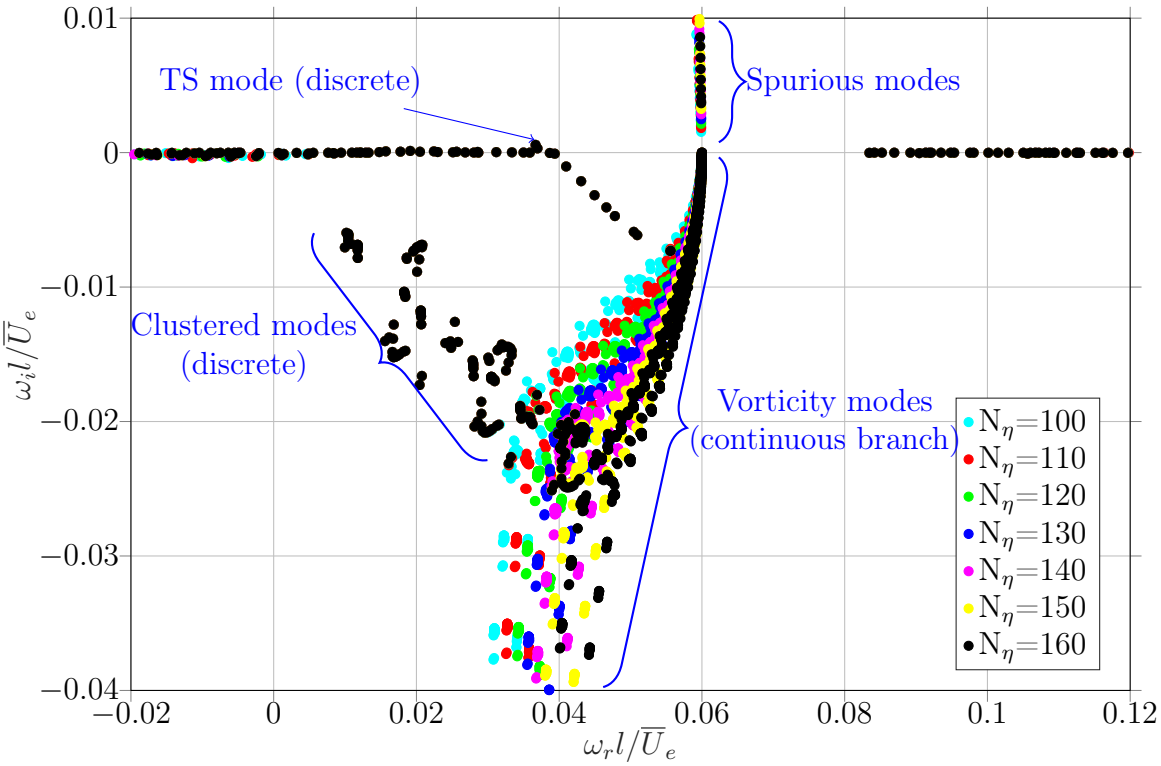

Figure 3.2.1: Compressible ($M = 2.5$) streamwise parallel Blasius: convergence of the BiGlobal spectrum with respect to the normal direction N_η for a fixed $N_\xi = 15$.

N_η	$\omega_r l/\overline{U}_e$	$\omega_i l/\overline{U}_e$	ϵ_{crit}
100	0.036691071	0.000572142	$1.9e^{-12}$
110	0.036691071251	0.0005721423	$2.6e^{-12}$
120	0.036691071249	0.00057214231	$3.4e^{-12}$
130	0.036691071247	0.00057214232	$4.4e^{-12}$
140	0.036691071255	0.00057214231	$5.7e^{-12}$
150	0.036691071247	0.00057214232	$7.2e^{-12}$
160	0.036691071247	0.00057214232	$9.1e^{-12}$

Table 3.2.2: Compressible ($M = 2.5$) streamwise parallel Blasius: convergence of the most unstable mode with respect to the spanwise direction N_η for fixed $N_\xi = 15$.

where developing boundary layers are analysed, the application of the previously derived LPPE is handled beside comparison with Neumann and PC boundary closures.

The continuous branch, even if a low convergence rate is observed, represents physical modes. The apparition of branches in spectra is due to modes flowing through the boundaries. For example, the TS waves for a developing boundary layer is travelling from the inlet to the outlet of the domain. It, therefore, implies the TS mode is represented by a continuous branch (section 4). In contrast, for the present case of parallel Blasius, the TS mode is enclosed inside the domain and is not advected within the confinements

of the domain through the boundaries by any group speed ($c_{gr,\mathrm{TS}} = 0$) defined as:

$$c_{gr} = \frac{\partial \omega_r}{\partial k_r}, \tag{3.2.1}$$

where k_r is a real wavenumber in the direction of the advection. The continuous branch depicted by Fig. 3.2.1 represents vorticity modes travelling through the top boundary of the domain (non-zero group speed).

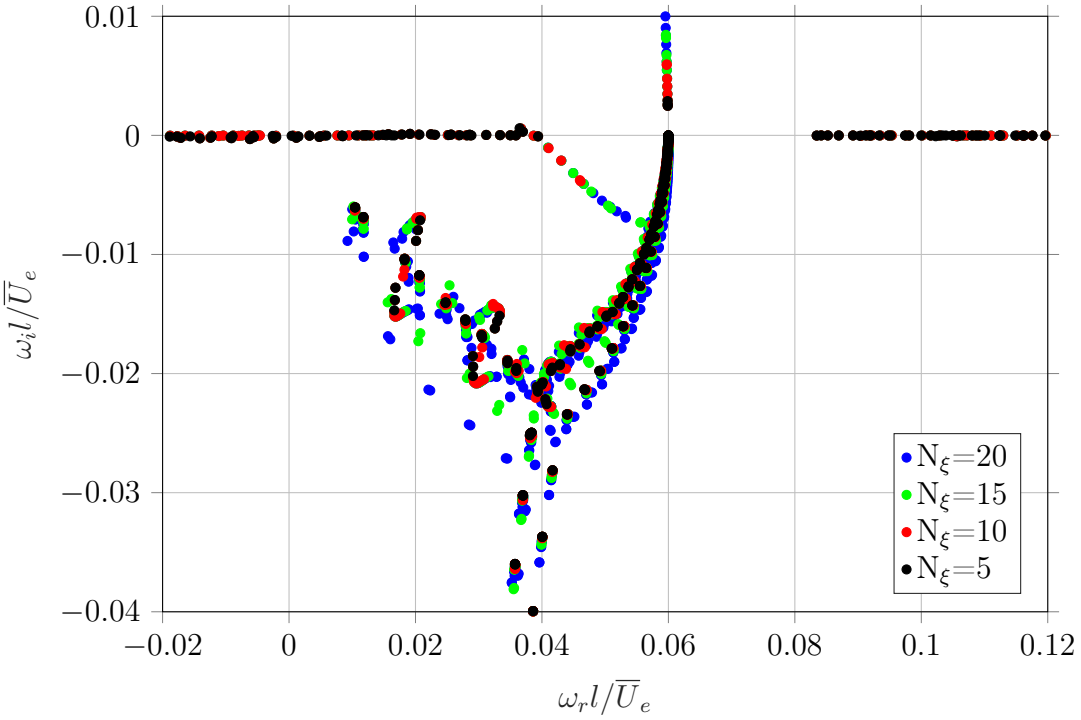

Figure 3.2.2: Compressible ($M = 2.5$) streamwise parallel Blasius: convergence of the BiGlobal spectrum with respect to the spanwise direction N_ξ for fixed $N_\eta = 130$.

N_ξ	$\omega_r l/\overline{U}_e$	$\omega_i l/\overline{U}_e$	ϵ_{crit}
5	0.036	0.0006	$2.5e^{-12}$
10	0.03669	0.000572	$3.6e^{-12}$
15	0.03669107124	0.000572142317	$4.4e^{-12}$
20	0.03669107124	0.000572142317	$5.1e^{-12}$

Table 3.2.3: Compressible ($M = 2.5$) streamwise parallel Blasius: convergence of the most unstable mode with respect to the spanwise direction N_ξ for fixed $N_\eta = 130$.

Additionally, according to Balakumar and Malik [1992], the most dominant part of a mode is evaluated with the following relation:

$$\overline{U}|_{y_{\tilde{q}_{max}}} = c_{ph} = \frac{\omega_r}{k_i}, \tag{3.2.2}$$

where c_{ph} is the phase speed. Considering the asymptotic behaviour of the continuous branch, it implies that the relation described by Eq. (3.2.2) tends to one; the vorticity

modes are dominant in the freestream. Thence, it highlights that the mode is prone to travel across the upper boundary.

A similar convergence analysis is performed with the incompressible boundary layer as depicted in Fig. 3.2.3 for the wall normal direction η and by Fig. 3.2.4 for the spanwise direction ξ. The same behaviour as the compressible case can be observed with a high convergence rate of the discrete modes and a low one for the continuous branch. Moreover, the spurious modes are again present due to the pressure boundary closure. Fig. 3.2.3 clearly shows the linear divergence of the spurious modes when the number of collocation points in the normal direction is increased.

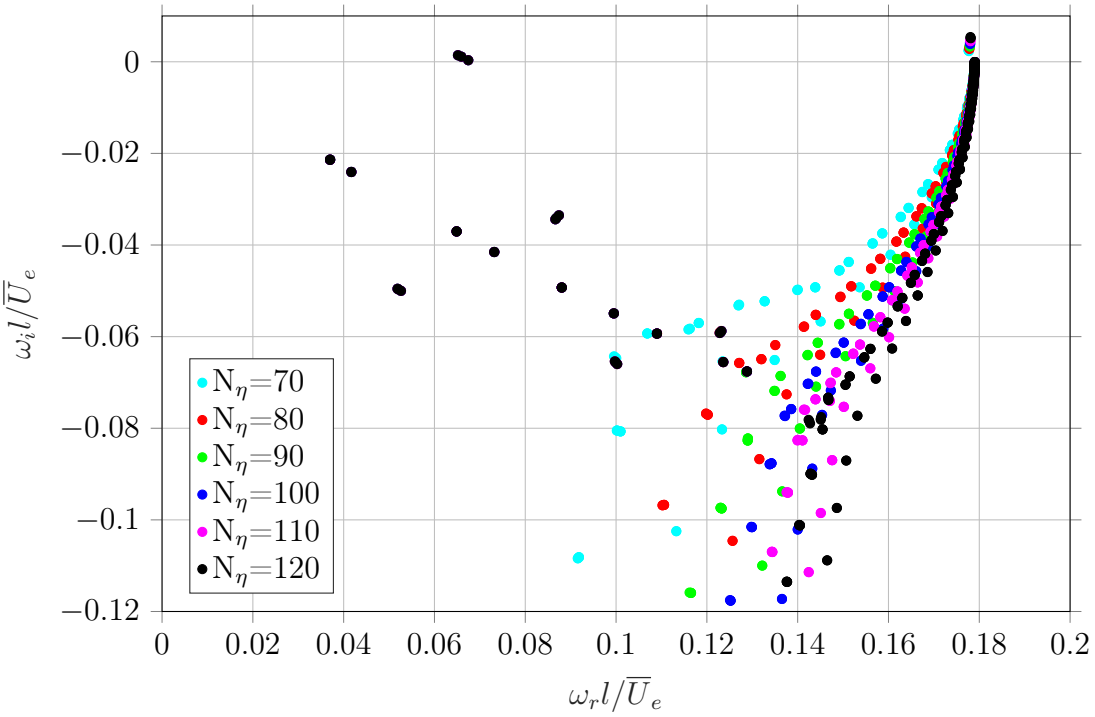

Figure 3.2.3: Incompressible ($M = 10^{-6}$) streamwise parallel Blasius: convergence of the BiGlobal spectrum with respect to the normal direction N_η for a fixed $N_\xi = 5$.

N_η	$\omega_r l/\overline{U}_e$	$\omega_i l/\overline{U}_e$	ϵ_{crit}
70	0.06517800	0.001424787	$6.4e^{-8}$
80	0.06517800	0.001424787	$8.1e^{-8}$
90	0.0651779	0.0014247	$1.0e^{-7}$
100	0.0651779	0.00142478	$2.5e^{-7}$
110	0.0651780	0.00142478686	$1.2e^{-7}$
120	0.0651780	0.001424786857	$1.5e^{-7}$

Table 3.2.4: Incompressible ($M = 10^{-6}$) streamwise parallel Blasius: convergence of the most unstable mode with respect to the normal direction N_η for fixed $N_\eta = 5$.

In Tab. 3.2.3, the convergence with respect to N_η is shown for the most unstable mode. It is converged when the difference between two N_η reaches the order of magnitude of ϵ_{crit}. Therefore, N_η larger than 100 is sufficient for the incompressible case.

Nonetheless, ϵ_{crit} is about 10^{-7} while the compressible Blasius reaches $\epsilon_{crit} = 10^{-12}$. This significant difference is due to the non-dimensional form of the stability equations. For the incompressible formulation, the pressure is not involved while the present compressible stability equations use the non-dimensional pressure $\overline{P} = \frac{1}{\gamma M^2}$. For the incompressible case, with $M = 10^{-6}$, the pressure is extremely large and the numerical evaluation of the eigenvalue problem is ill-posed. It leads to a significantly high Frobenius norm of the matrices A and B, increasing ϵ_{crit}. For this particular reason, even

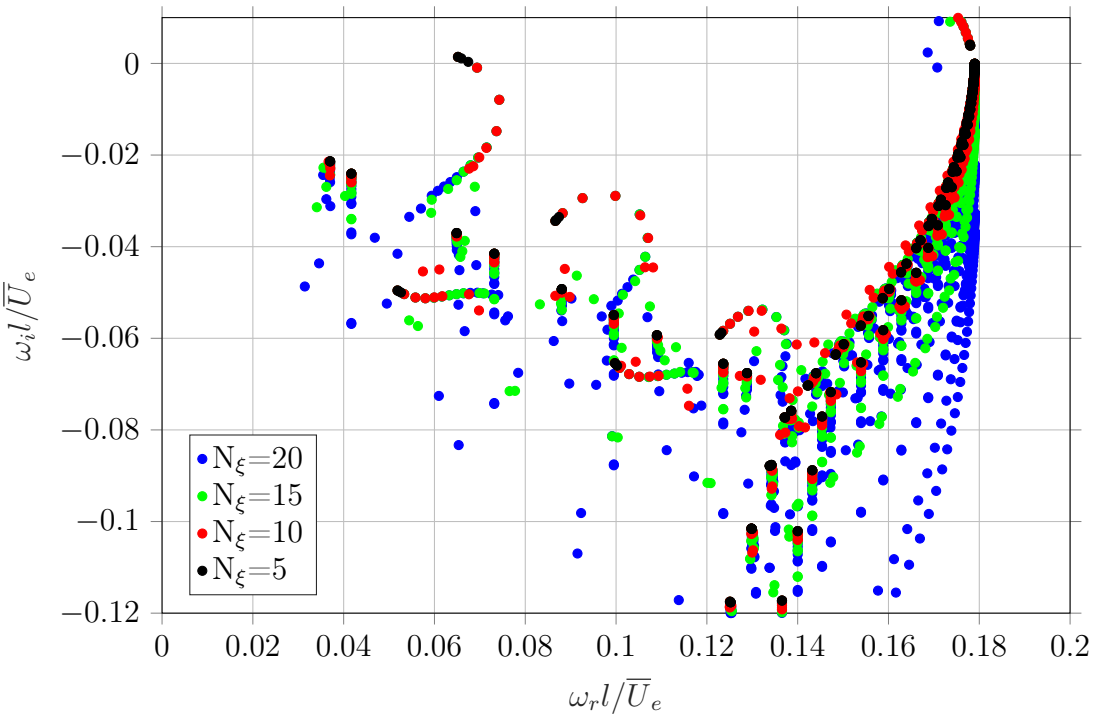

Figure 3.2.4: Incompressible ($M = 10^{-6}$) streamwise parallel Blasius: convergence of the BiGlobal spectrum with respect to the spanwise direction N_ξ for fixed $N_\eta = 100$.

N_η	$\omega_r l/\overline{U}_e$	$\omega_i l/\overline{U}_e$	ϵ_{crit}
5	0.06518	0.00142478	$1.0e^{-7}$
10	0.06518	0.001424787	$1.6e^{-7}$
15	0.0651779	0.001424787	$2.1e^{-7}$
20	0.0651779	0.001424787	$2.5e^{-7}$

Table 3.2.5: Incompressible ($M = 10^{-6}$) streamwise parallel Blasius: convergence of the most unstable mode with respect to the normal direction N_ξ for fixed $N_\eta = 100$.

though the base flow has been computed with $M = 10^{-6}$, the constant pressure used to solve the BiGlobal stability equations is based on $M = 10^{-3}$, reducing ϵ_{crit} from 10^5 to 10^{-7}. A lower value of ϵ_{crit} could be obtained by increasing again the Mach number, but it then leads to non-negligible discrepancies with the stability results of Groot [2013]. The choice of $M = 10^{-3}$ consists of a good compromise between high accuracy (i.e low value of ϵ_{crit}) and consistency with the base flow Mach number (i.e very low subsonic

case). Another approach is to scale the pressure differently, but this would require changing the equations in the current implementation which is here avoided for integrity purposes.

Regarding the discretisation in the z-direction (N_ξ), Tab. 3.2.4 shows that five points are already sufficient to ensure converged results. Such a low value of N_ξ is simply due to the zero spanwise wavenumber of the most unstable mode for the incompressible case ($\beta = 0$). It implies that even three points (two for the boundary conditions and one inside the domain) in z-direction are already sufficient; the wavefronts of the mode are strictly parallel to the base flow plane. Finally, the collocation grid $[N_\xi, N_\eta] \times [120, 5]$ is kept for later mode analyses and code validation.

Considering the two Blasius cases for which the convergence is ensured, the eigenvalue of most unstable mode can be compared with stability analyses reported in the references carried out on exactly the same cases in order to validate the current BiGlobal tool. Tab. 3.2.6 compares the present values obtained for the Tollmien-Schlichting mode with the reported LST data of Mack [1976], Malik [1990], Pinna [2012] and Groot [2013]. The cited authors reported the values of the complex phase velocity ($c_{ph} = \frac{\omega}{\alpha}$) for the incompressible case, with $\alpha = 0.179$. Nonetheless, for sake of consistency, Tab. 3.2.6 shows the complex frequency ω for both incompressible and compressible Blasius boundary layers. It clearly shows that the results are in perfect agreement with the previous analyses and the current BiGlobal tool is able to compute the stability properties of both compressible and incompressible (very low subsonic) cases.

Reference	$M = 2.5$	$M = 10^{-6}$
Current BiG	$0.0366911 + 0.0005721i$	$0.065177999 + 0.00142478i$
Mack [1976]	$0.0367339 + 0.0005840i$	$0.0651739 + 0.001432i$
Malik [1990]	NA	$0.0651739 + 0.0014141i$
Pinna [2012]	$0.0366795 + 0.0005728i$	$0.06517569 + 0.00142484i$
Groot [2013]	$0.0366911 + 0.0005721i$	$0.065178017 + 0.00142484i$

Table 3.2.6: Comparison of the temporal growth rate and frequency of the Tollmien-Schlichting mode with external LST results.

Analysis of modes

Up to this point, the spectra delivered all the existing eigenvalues in the Blasius flow. The growth rate, as well as the frequency, can be directly extracted to have an insight into the temporal stability. However, it does not directly provide spatial information about the modes. Such analysis is briefly performed in the current section in order to give an overview of the spatial behaviour of the TS and the pressure spurious modes. Furthermore, many clusters of discrete modes exist as depicted in Fig. 3.2.1, but it is not considered as a detailed analysis has been conducted by Groot [2013] for exactly the same boundary layer cases.

In Fig. 3.2.5 and Fig. 3.2.6, the eigenfunctions corresponding to the TS mode for compressible and incompressible cases, respectively, are shown. For the former, Fig. 3.2.5 shows clearly the spanwise wavelength of the mode corresponding to $\frac{2\pi}{\beta} = \frac{2\pi}{0.1} \approx 62.83l$. After reaching a maximum, all the variables (even $\tilde{T}$, not shown for sake of brevity),

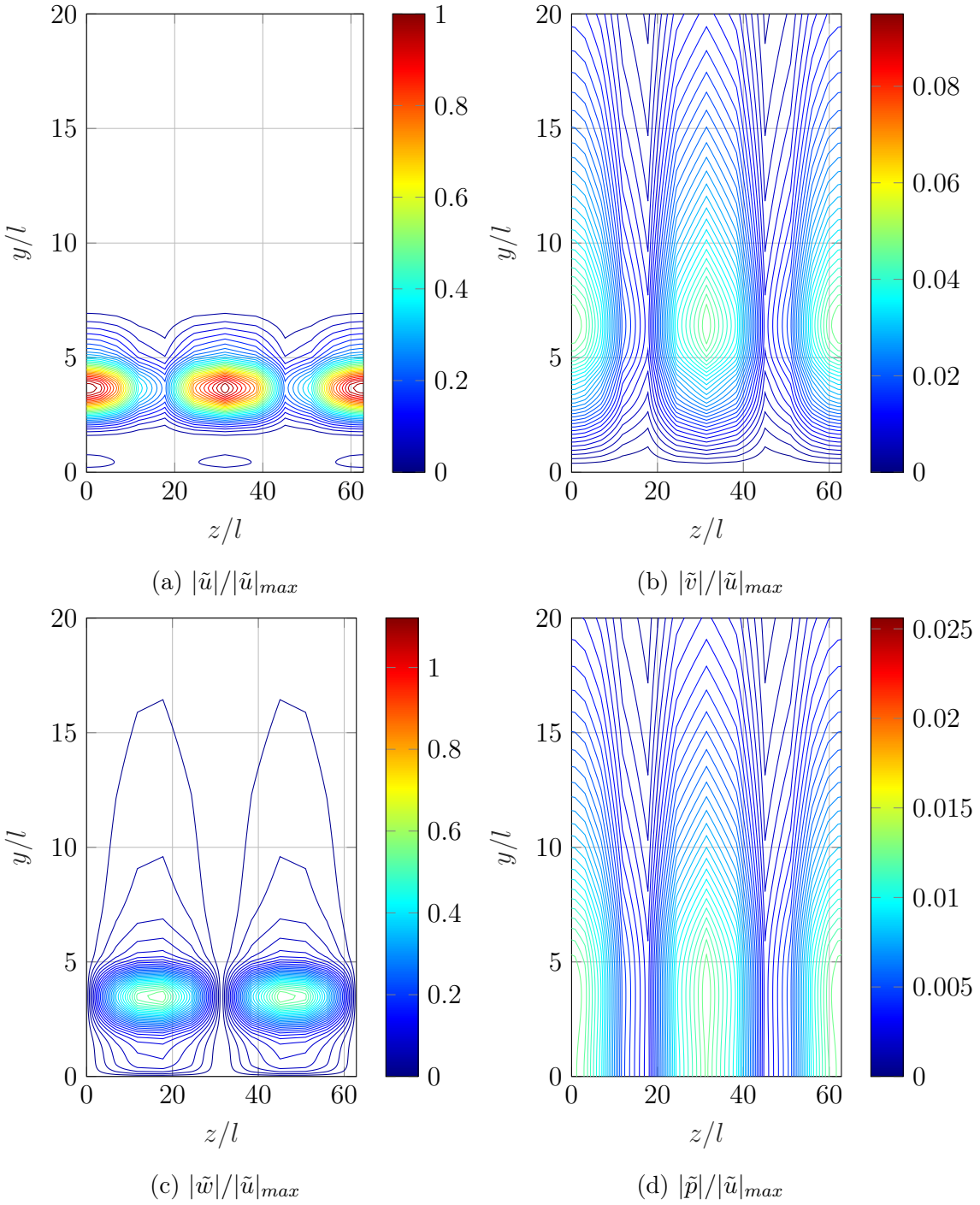

(a) $|\tilde{u}|/|\tilde{u}|_{max}$ (b) $|\tilde{v}|/|\tilde{u}|_{max}$

(c) $|\tilde{w}|/|\tilde{u}|_{max}$ (d) $|\tilde{p}|/|\tilde{u}|_{max}$

Figure 3.2.5: Compressible ($M = 2.5$) with $[N_\xi, N_\eta] \times [160, 15]$: two dimensional contour plot of the Tollmien-Schlichting mode.

the mode decays in the wall normal direction. In Fig. 3.2.7a, where the mode is shown at $z/l = 6.85$, it can be seen in a better way that all the variable tends to zero when $y_{max} \to \infty$. Mathematically, this spatial decay of the Tollmien-Schlichting wave is represented by $e^{-y\sqrt{\alpha^2+\beta^2-(\alpha-\omega)^2M^2}}$. It is therefore important to impose the boundary conditions such that the mode behaves properly at the edge of the domain. Applying

the Neumann condition in the freestream with a too small domain height is generally not able to represent the proper spatial decay due to an enforced zero-gradient at the boundary.
Due to the non-zero β, the z-component of the perturbation velocity, $\tilde{w}$, is not zero. It implies that the wave is oblique and has its front oriented with an angle $\arctan\frac{\beta}{\alpha} = \arctan\frac{0.1}{0.06} = 59.03\,^\circ$ with respect to the streamwise x-axis. In other words, the wave is travelling with an angle of about 59.03° with respect to the streamwise velocity component $\overline{U}$, although $\overline{W} = 0$.

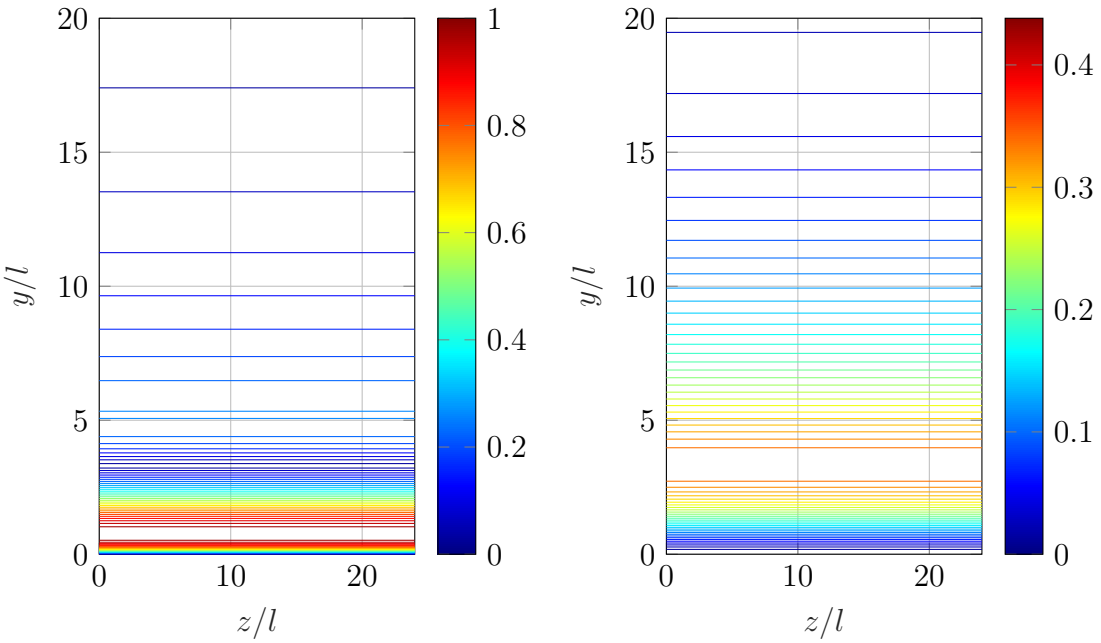

(a) $|\tilde{u}|/|\tilde{u}|_{max}$ (b) $|\tilde{v}|/|\tilde{u}|_{max}$

Figure 3.2.6: Incompressible ($M = 10^{-6}$) with $[N_\xi, N_\eta] \times [120, 5]$: two dimensional contour plot of the Tollmien-Schlichting mode.

The TS mode of the incompressible boundary layer is shown in Fig. 3.2.6 over the entire 2D domain, while Fig. 3.2.7b shows the wave amplitude profile at one spanwise location. For this case, the spanwise wavelength is infinite ($\beta = 0$), yielding a decoupling of the z-momentum equation and then $\tilde{w} = 0$. Therefore, for sake of brevity, only $\tilde{u}$ and $\tilde{v}$ are shown in Fig. 3.2.6.
In the wall-normal direction, the behaviour of the mode is quite similar to the compressible one but with a smaller spatial decay in the freestream. It is justified by the smaller β and Mach number than the supersonic boundary layer case. The incompressible TS wave presents its maximum amplitude close to the wall while its compressible equivalent has a first small increase in amplitude at this location and reaches a maximum higher in the boundary layer. This behaviour is explained with Eq. (3.2.2) derived by Balakumar and Malik [1992] arguing that the phase speed provides information about the location where the mode is the most dominant. For the compressible TS case, $\overline{U}|_{y_{\tilde{q}_{max}}} = c_{ph} = 0.612$ showing that the mode has its main impact in the middle of the boundary layer while for the incompressible case $\overline{U}|_{y_{\tilde{q}_{max}}} = 0.364$; TS mode is dominant closer to the wall.

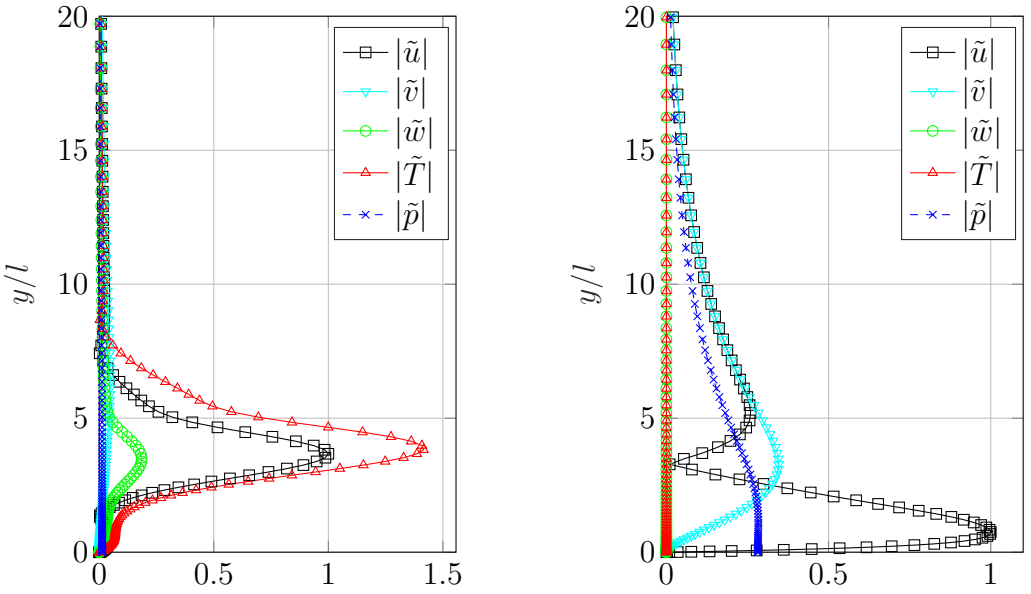

(a) Compressible ($M = 2.5$) at $z/l = 6.85$ with $[N_\xi, N_\eta] \times [160, 15]$.

(b) Incompressible ($M = 10^{-6}$) at any z/l with $[N_\xi, N_\eta] \times [120, 5]$.

Figure 3.2.7: Perturbation components normalised by $|\tilde{u}|_{max}$ of the Tollmien-Schlichting mode.

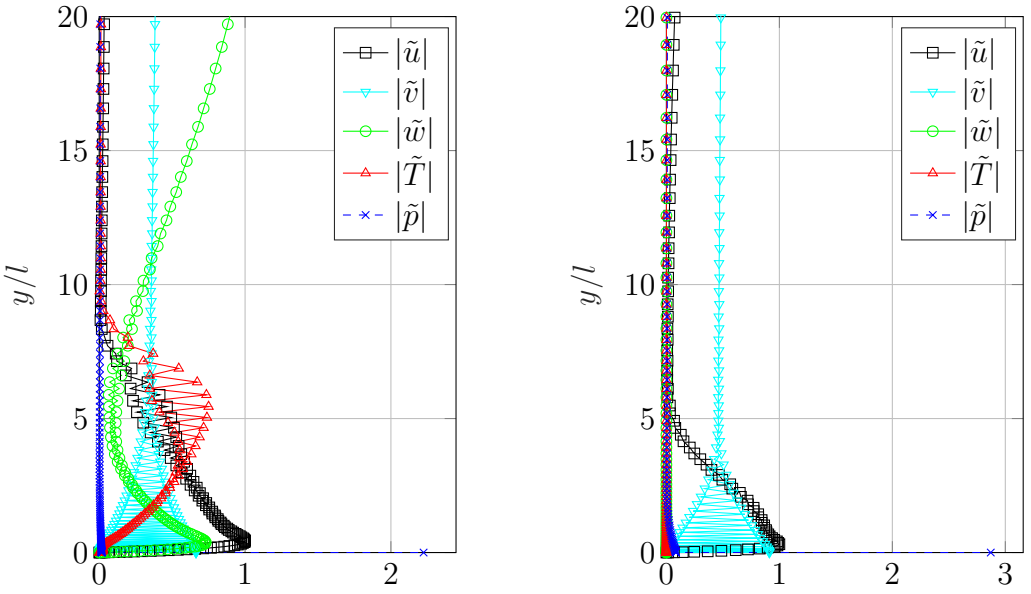

(a) Compressible ($M = 2.5$) at $z/l = 6.85$ with $[N_\xi, N_\eta] \times [160, 15]$.

(b) Incompressible ($M = 10^{-6}$) at $z/l = 12$ with $[N_\xi, N_\eta] \times [120, 5]$.

Figure 3.2.8: Perturbation components normalised by $|\tilde{u}|_{max}$ for the most unstable spurious pressure mode.

Even if they do not represent any physical phenomenon, it is relevant to distinguish the spurious modes from the others. Fig. 3.2.8 shows the most unstable spurious modes for the collocation grids $[N_\xi, N_\eta] \times [160, 15]$ and $[N_\xi, N_\eta] \times [120, 5]$ for the compressible

and incompressible cases, respectively. The oscillatory behaviour of the spurious mode represents clearly its main characteristic. Generally, $\tilde{v}$ is the most sensitive variable and presents high amplitude oscillations close to the wall. Regarding the pressure, the first grid point is overestimated compared to the rest of the field, which is caused by the PC boundary closure relating the first order wall normal derivative of $\tilde{p}$ with the second order wall normal derivative of $\tilde{v}$.

3.2.2 Rotated parallel compressible Blasius ($M = 2.5$)

The previous analyses based on the streamwise parallel Blasius involved only the x-component of the velocity field and therefore, many terms of the BiGlobal equations dropped out due to $\overline{V} = \overline{W} = 0$. In order to verify in another way the stability code, a velocity $\overline{W}$ is added to the base flow such that the streamwise case is rotated with an angle equivalent to $\arctan\frac{\overline{W}}{\overline{U}}$ with respect to the x-axis. This rotation is done to have the wavefronts of the TS mode perpendicular to the flow direction $(\overline{W}, \overline{U})$, which renders the numerical problem in the z-direction trivial, because, again, only the constant amplitude profile is to be resolved. It implies

$$\sqrt{\overline{W}^2 + \overline{U}^2} = 1\,, \qquad \overline{W} = \frac{\beta_s}{\alpha_s}\overline{U}_s\,, \qquad \overline{U} = \frac{\overline{U}_s}{\sqrt{1 + (\frac{\beta_s}{\alpha_s})^2}} \tag{3.2.3}$$

where the subscript s represents the variables computed beforehand for the streamwise parallel Blasius. In addition, the value of α for the assumed spectral direction becomes

$$\alpha = \sqrt{\beta_s^2 + \alpha_s^2} \tag{3.2.4}$$

Quantitatively, the parameters of the rotated parallel Blasius are summarised in Tab. 3.2.7, for the compressible case only. It is not relevant to rotate the incompressible boundary layer, because of $\beta = 0$; the flow direction is already perpendicular to the wavefronts of the TS mode.

Case	M	Re	$\overline{U}_e$	$\overline{V}_e$	$\overline{W}_e$	α	y_i	y_{max}
Streamise	2.5	3000	1	0	0	0.06	6	283
Rotated	2.5	3000	0.514	0	0.858	0.116	6	283

Table 3.2.7: Comparison of the set-up between streamwise and rotated parallel Blasius.

Consequently, the rotation of the flow allows validating in another way the BiGlobal code as the most unstable mode has the same temporal behaviour but more terms are involved in the stability equations. Before comparing ω with the streamwise case, a convergence analysis is carried out in both y and z-directions. Fig. 3.2.9 and Fig. 3.2.10 show the spectrum convergence in the former direction (N_η) for fixed odd and even N_ξ, respectively. A differentiation is done for N_ξ because the continuous branches, except the one with vorticity modes, are not represented in the same way depending if N_ξ is odd or even. For instance, in the range displayed by Fig. 3.2.9 and Fig. 3.2.10, the number of continuous branches is different. This behaviour is analysed later in the current section

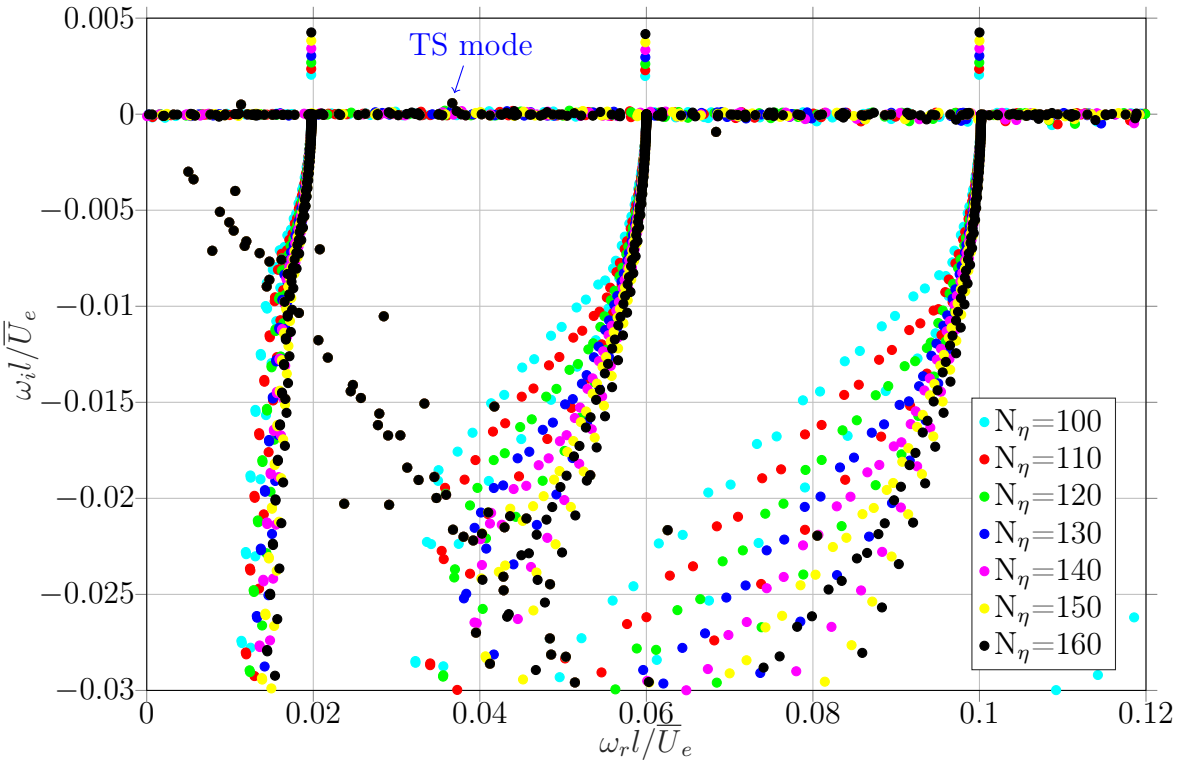

Figure 3.2.9: Rotated parallel Blasius: convergence of the BiGlobal spectrum with respect to the normal direction N_η for a fixed odd $N_\xi = 15$.

N_η	$\omega_r l/\overline{U}_e$	$\omega_i l/\overline{U}_e$	ϵ_{crit}
100	0.0366910712	0.000572142	$2.0e^{-12}$
110	0.03669107125	0.0005721423	$3.4e^{-12}$
120	0.03669107125	0.00057214231	$5.7e^{-12}$
130	0.03669107124	0.00057214232	$9.1e^{-12}$
140	0.03669107125	0.00057214232	$2.7e^{-12}$
150	0.03669107092	0.00057213759	$4.6e^{-12}$
160	0.03669107125	0.00057214232	$7.5e^{-12}$

Table 3.2.8: Rotated parallel Blasius: convergence of the most unstable mode with respect to the normal direction N_η for a fixed odd $N_\xi = 15$.

by considering different N_ξ on a larger spectrum range.

Nonetheless, as depicted in Fig. 3.2.9 and Fig. 3.2.10, the physical modes are not affected by the odd-even distinction. Therefore, the convergence analysis can be properly conducted for this TS mode, which remains the most unstable as expected. Tab. 3.2.8 and Tab. 3.2.9 show that increasing N_η leads to a convergence level with an order of magnitude reaching the critical epsilon for both odd and even N_ξ. There is a small exception with $N_\eta = 150$ which exhibits a quite significant difference compared to the cases with $N_\eta = 140$ and $N_\eta = 160$. No explanation has been found for this small discrepancy and it is neglected since all the other cases show a proper convergence of the results according to the magnitude of ϵ_{crit}.

Considering the convergence in z-direction, the strong dependence on the parity of N_ξ is depicted as well in Fig. 3.2.11 and Fig. 3.2.12. It shows that the vorticity branch with the asymptotic behaviour at $\omega_r l/\overline{U}_e = 0.06$ is converged with respect to all N_ξ cases. On the other hand, the adjacent continuous branches converge with a slow rate as the odd/even N_ξ numerically constraints the possible wavenumbers.

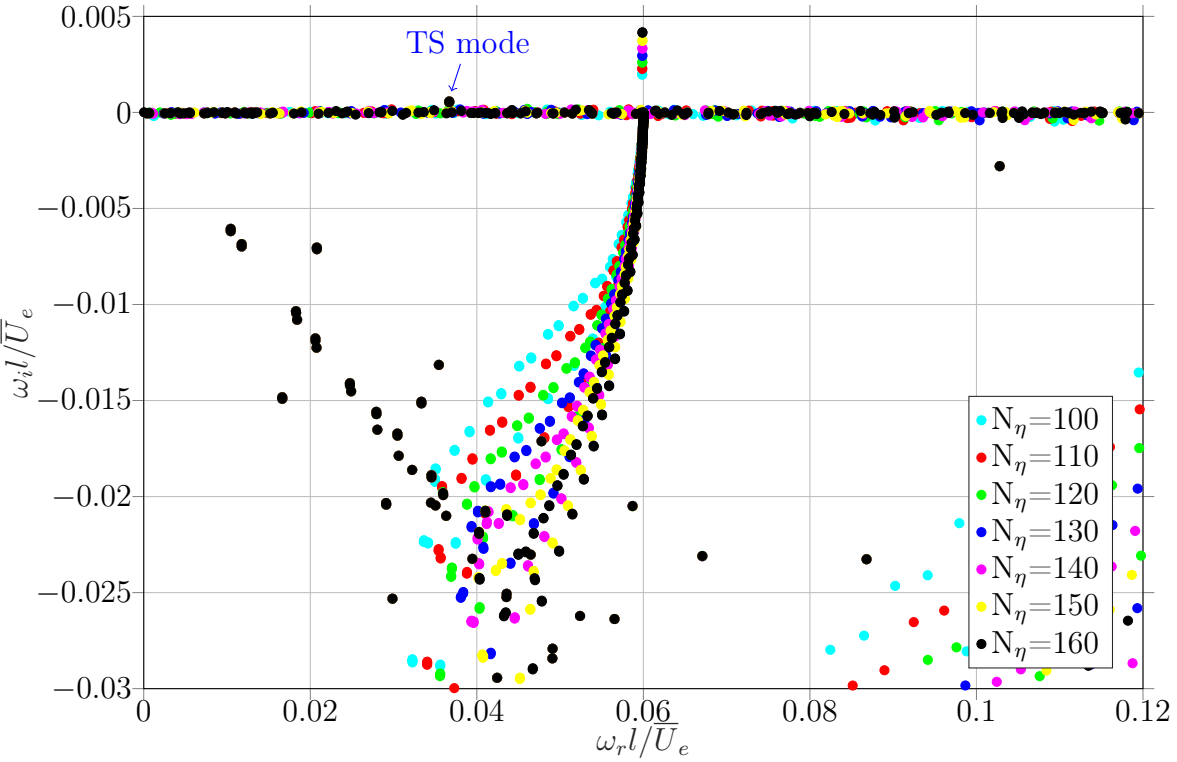

Figure 3.2.10: Rotated parallel Blasius: convergence of the BiGlobal spectrum with respect to the normal direction N_η for a fixed even $N_\xi = 16$.

N_η	$\omega_r l/\overline{U}_e$	$\omega_i l/\overline{U}_e$	ϵ_{crit}
100	0.03669107124	0.00057214199	$2.6e^{-12}$
110	0.03669107138	0.00057214236	$4.4e^{-12}$
120	0.03669107116	0.00057214233	$7.2e^{-12}$
130	0.03669107132	0.00057214217	$2.1e^{-12}$
140	0.03669107108	0.00057214291	$3.5e^{-12}$
150	0.03669107165	0.00057214244	$5.9e^{-12}$
160	0.03669107019	0.00057214165	$9.5e^{-12}$

Table 3.2.9: Rotated parallel Blasius: convergence of the most unstable mode with respect to the normal direction N_η for a fixed even $N_\xi = 16$.

Fig. 3.2.13 and Fig. 3.2.14 show a larger range of the spectra with the odd and even N_ξ. It reveals $N_\xi - 2$ similar branches presenting a low convergence rate. A hypothesis about the existence of such modes is due to the components $\overline{W}$ that induces the mode to travel across the lateral boundaries. Furthermore, changing the number of collocation points in the spanwise direction allows the existence of the modes with a lower smallest

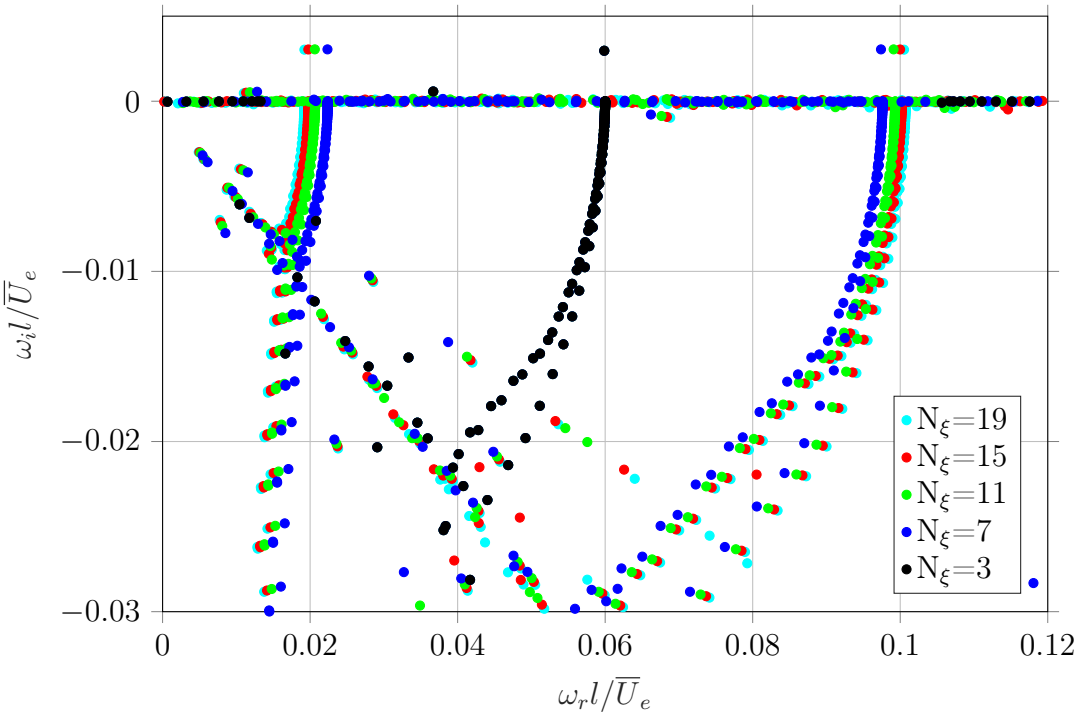

Figure 3.2.11: Rotated parallel Blasius: convergence of the BiGlobal spectrum with respect to the spanwise direction N_ξ (odd) for a fixed $N_\eta = 130$.

N_ξ	$\omega_r l/\overline{U}_e$	$\omega_i l/\overline{U}_e$	ϵ_{crit}
3	0.03669107124	0.000572142317	$1.8e^{-12}$
7	0.03669107124	0.000572142318	$2.9e^{-12}$
11	0.03669107124	0.000572142317	$3.7e^{-12}$
15	0.03669107124	0.000572142317	$4.4e^{-12}$
19	0.03669107124	0.000572142317	$5.0e^{-12}$

Table 3.2.10: Rotated parallel Blasius: convergence of the most unstable mode with respect to the spanwise direction N_ξ (odd) for a fixed $N_\eta = 130$.

N_ξ	$\omega_r l/\overline{U}_e$	$\omega_i l/\overline{U}_e$	ϵ_{crit}
4	0.0366910	0.000572142	$2.2e^{-12}$
8	0.03669106	0.000572142	$3.2e^{-12}$
12	0.036691072	0.000572142	$3.9e^{-12}$
16	0.036691071	0.0005721421	$4.6e^{-12}$
20	0.036691071	0.0005721422	$5.1e^{-12}$

Table 3.2.11: Compressible ($M = 2.5$) rotated parallel Blasius: convergence of the most unstable mode with respect to the spanwise direction N_ξ (even) for a fixed $N_\eta = 130$.

wavenumber β, but the origin of the behaviour is purely numerical and is still unexplained despite the observation by Groot [2013]. Note that the other branches occur symmetrically to vorticity branch $c_{ph} = 1$ and an increase of collocation nodes tends to increase the distance from this axis of symmetry. In addition, a spurious pressure mode

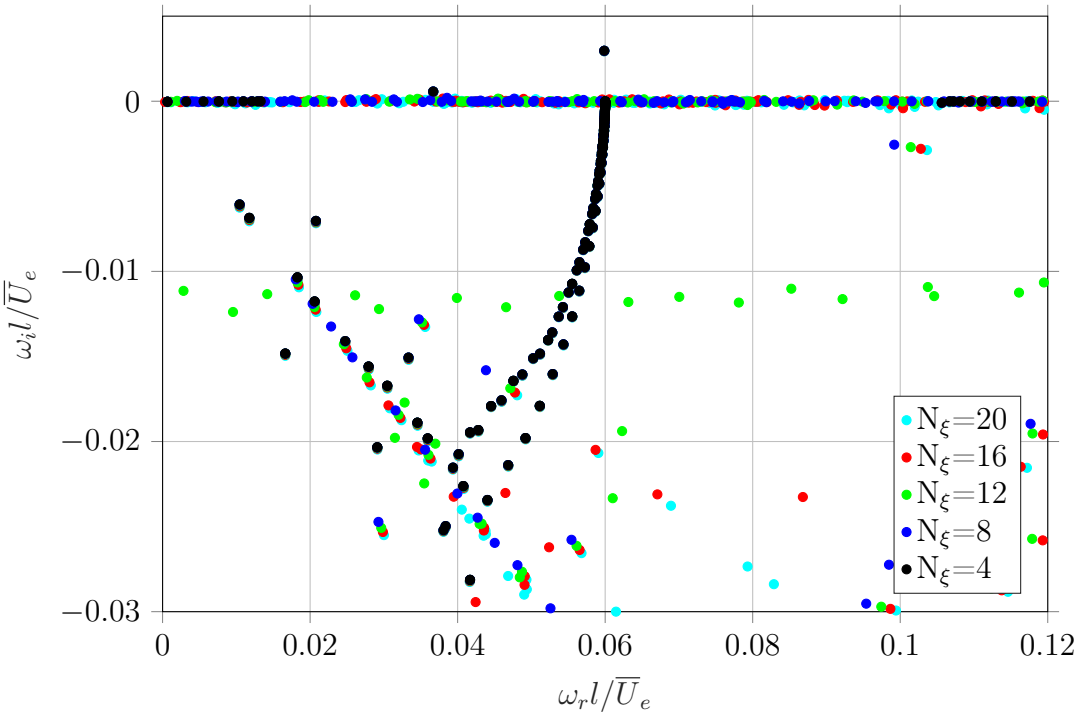

Figure 3.2.12: Rotated parallel Blasius: convergence of the BiGlobal spectrum with respect to the spanwise direction N_ξ (even) for a fixed $N_\eta = 130$.

can be observed on the top of each branch. Additionally, Fig. 3.2.13 and Fig. 3.2.14 depicts other numerical modes represented by horizontal branches clearly visible for the cases $N_\xi = 12, 15, 16$. However, it finally reveals these modes are diverging, towards high imaginary values, when the z-resolution is increased as shown by Fig. 3.2.13 and Fig. 3.2.14. Nonetheless, even if the spectrum is less clean for the rotated Blasius than for the streamwise one, the convergence of the TS mode with respect to N_ξ remains excellent (Tab. 3.2.10 and Tab. 3.2.11) for both even and odd discretisation. As for the incompressible case where $\overline{U}$ is aligned with the direction of the mode propagation, $N_\xi = 3$ is sufficient for the rotated compressible Blasius.

Finally, the temporal growth rate and frequency of the most unstable mode are compared with the previously studied streamwise case in Tab. 3.2.12. It highlights a small difference of 10^{-11} and 10^{-10} for the real and imaginary part, respectively, between the odd and even case of the rotated Blasius. While an absolute difference of about 10^{-12} and 10^{-14} is found between the rotated with an odd N_ξ and the streamwise Blasius. According to ϵ_{crit}, it is confirmed that the odd discretisation provides exactly the same results as the streamwise flow while the even rotated Blasius reveals a very small discrepancy. Although it remains close to the order of magnitude of critical epsilon, the use of an even number for N_ξ is recommended as it resolves more relevant harmonics.

All the different spectra obtained for the parallel Blasius are perfectly adapted to validate the BiGlobal stability tool because of their simplicity as well as the reachable high accuracy. However, it is important to remark that all the different cases have $\overline{V} = 0$; the terms of the BiGlobal equations involving $\overline{V}$ are zeroed. The validation of the current code could therefore be seen as not totally achieved. Nonetheless, regarding

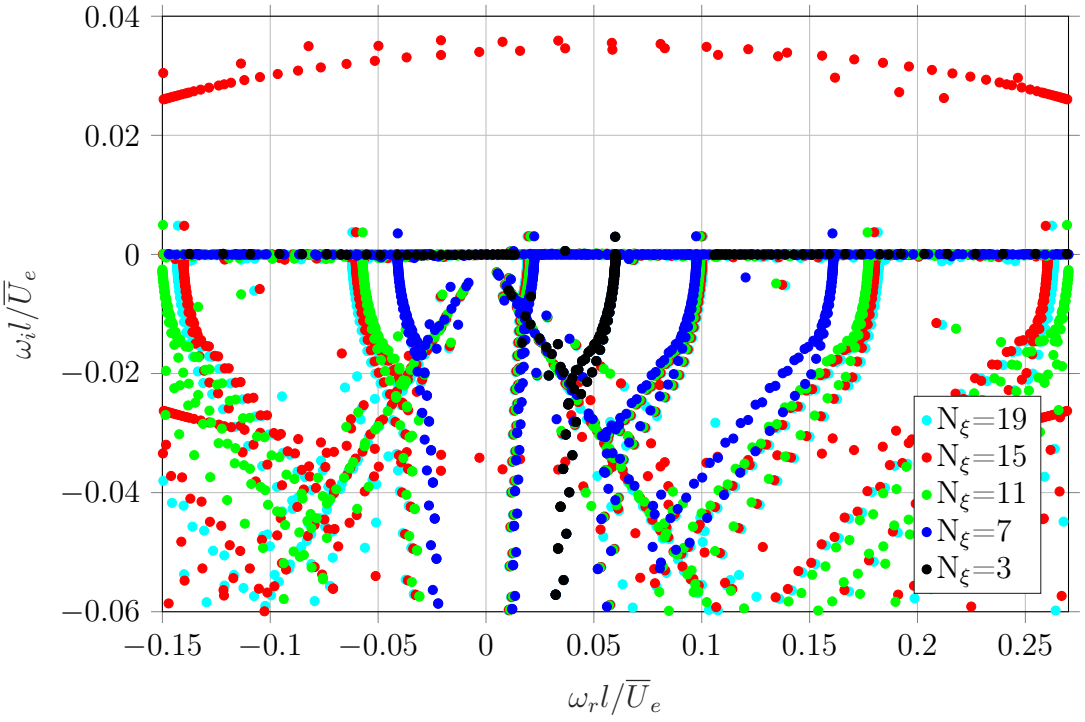

Figure 3.2.13: Rotated parallel Blasius: convergence of the BiGlobal spectrum with respect to the normal direction N_ξ (odd) for a fixed $N_\eta = 130$ (Zoom out).

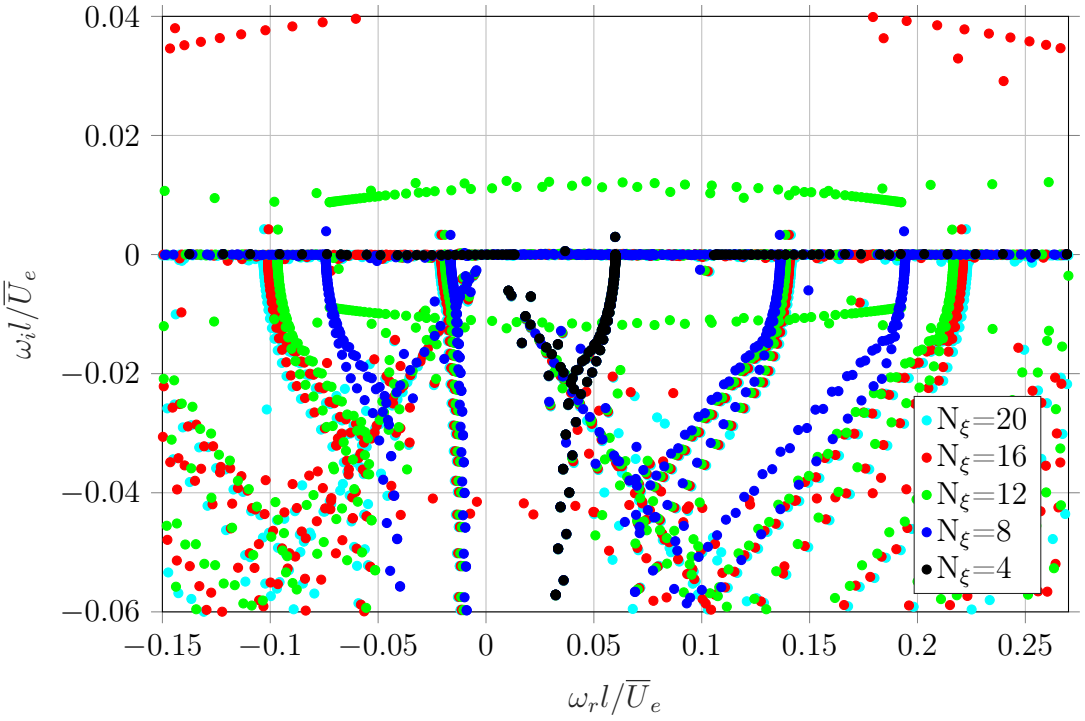

Figure 3.2.14: Rotated parallel Blasius: convergence of the BiGlobal spectrum with respect to the normal direction N_ξ (even) for a fixed even $N_\eta = 130$ (Zoom out).

Case	$\omega_r l/\overline{U}_e$	$\omega_i l/\overline{U}_e$	ϵ_{crit}
Rotated BiG N_ξ Odd	0.036691071245	0.000572142317	$4.4e^{-12}$
Rotated BiG N_ξ Even	0.036691071316	0.000572142169	$4.6e^{-12}$
Streamwise BiG	0.036691071247	0.000572142317	$4.4e^{-12}$

Table 3.2.12: Comparison of the temporal growth rate and frequency of Tollmien-Schlicthing mode with streamwise parallel Blasius with odd and even collocation grids $[N_\xi, N_\eta] \times [130, 15]$ and $[N_\xi, N_\eta] \times [130, 16]$, respectively.

the methodology followed to implement the boundary conditions and the results provided for the parallel Blasius, the only potential source of error is the set of stability equations itself. However, it has been verified with respect to well-validated equations from Pinna and Groot [2014] that also do not involve $\overline{V}$. Therefore, the BiGlobal code developed in the current thesis is undoubtedly valid and can be used for application involving more complex flows.

3.3 Intermediate conclusion

In this chapter, the validation of the BiGlobal solver is handled with the parallel Blasius boundary layer. Due to its well-referenced stability properties for subsonic and supersonic regimes and to its high reproducibility, it consists of an adequate case to validate the code. The high accuracy base flows computed by Groot [2013] with a fourth-order Runge Kutta shooting method are reused. It minimises drastically the discrepancies with respect to that case and gives the opportunity to compare the results up to the eigensolver precision ϵ_{crit}. In order to involve a maximum of terms of the BiGlobal stability equations, one streamwise case and one rotated case of the parallel Blasius are considered.

The first case consists of a boundary layer whose only base flow velocity component is $\overline{U}$, such that it is perfectly aligned with the streamwise direction. One compressible ($M = 2.5$) and one incompressible ($M = 10^{-6}$) base flow are considered to show the ability of the code to solve a broad range. For the $M = 10^{-6}$ case, the reference Mach number for the BiGlobal equations is increased to $M = 10^{-3}$, such that it represents incompressible flows undoubtedly and it ensures a good conditioning of the matrices A and B, yielding a low level of ϵ_{crit}. A convergence analysis reveals that $[N_\xi, N_\eta] \times [160, 15]$ and $[N_\xi, N_\eta] \times [120, 5]$ collocation nodes respectively for the $M = 2.5$ and $M = 10^{-6}$ cases are sufficient to compute the temporal eigenvalue ω of the most unstable discrete mode (Tollmien-Schlichting) up to the precision of the eigensolver. It shows excellent agreement with the literature and particularly with the results obtained by Groot [2013], where a difference of $\mathcal{O}(\epsilon_{crit})$ is found for both flow regimes. In addition, a high convergence rate is observed for discrete modes, while the continuous branch needs a denser repartition of nodes because the former is dominant in the well-resolved boundary layer, while the latter is dominant in the freestream. The divergence of some eigenvalues in the spectrum highlights they are spurious numerical modes whose the eigenfunctions present highly oscillatory behaviour.

The second case uses the stability results from the compressible streamwise boundary layer (with $\beta \neq 0$) to rotate the flow such that the velocity vector $(\overline{U}, \overline{W})$ becomes

perpendicular to the wave crests of the most unstable Tollmien-Schlichting mode. It gives the opportunity to involve other terms of the BiGlobal equations, but the same mode as the streamwise case is retrieved exactly. The convergence analysis reveals differences in the spectrum if N_ξ is odd or even due to the wavenumbers that can be numerically resolved within the domain. The comparison with the streamwise case reveals an excellent agreement for the Tollmien-Schlichting waves and differences of $\mathcal{O}(\epsilon_{crit})$ are found. Selecting an even value for N_ξ is recommended as it exhibits a better agreement with the streamwise boundary layer.

4. Developing Boundary Layer

The following section focuses on the analysis of a low subsonic and a supersonic developing boundary layer. It provides a first insight into stability analysis of streamwise developing flows. It gives the opportunity to understand the different mechanisms that exist in such flows in order to select the best numerical set-up for further more complex configurations where shocks are involved.
The first part focuses on the base flows. Both supersonic and low subsonic cases are evaluated with a compressible boundary layer (CBL) solver marching in space. In addition, the former boundary layer is computed with Direct Numerical Simulation (DNS) to compare with the CBL solver.
In the second part, parameters studies are conducted on the stability results of the developing boundary layers, evaluated by the CBL solver only. The aim is to analyse the behaviour of the eigenvalue spectrum and the related modes with respect to the boundary conditions as well as the domain height. It gives an overview of the different structures present in the spectrum in order to understand the potential influence of the numerical set-up on the results. A convergence analysis on the low subsonic case ends the section.
The last part of the current chapter focuses on physical analyses of the Tollmien-Schlichting (TS) mode with a zero spanwise wavenumber (β) for both low subsonic and supersonic boundary layers. The reconstruction of wave packets related to this convective mode is handled. The streamwise growth rates and wavenumbers are evaluated with different methods. For the supersonic case, the analyses are carried out with the base flows computed with the DNS and CBL solvers. It provides, therefore, an overview of the stability equations sensitivity with respect to the accuracy of the base flows.

4.1 Numerical set-up of the base flows

The physical parameters of both subsonic and supersonic developing boundary layers are summarised in Tab. 4.1.1. The Reynolds numbers define the size of the domain from the leading edge of the flat plate, in the Blasius units l chosen as reference length. The former is selected as length scale for the BiGlobal analyses. Concerning the supersonic case, the flat plate dimensions are set according to the experiments of Giepman [2016]. The aim is to use exactly the same domain as the SWBLI cases for later comparisons. For the subsonic case, the flat plate length is arbitrarily chosen since the main purpose is to conduct a study of the numerical parameters. The supersonic boundary layer is numerically evaluated with an implicit CBL solver, and a DNS solver while the subsonic case is only computed with the former.

Case	Mach	Pr	Re_{in}	Re_{out}	l_{in} [m]
Low subsonic	0.1	0.72	435	949	7.9118×10^{-5}
Supersonic	1.7	0.72	923	2681	2.6372×10^{-5}

Table 4.1.1: Physical parameters of the developing boundary layers.

In regards of the subsonic boundary layer, the low Mach number makes this case to be considered as incompressible. According to Chapman [2000], the compressibility effects can be ignored since the square of the Mach number ($M^2 = 0.01$) is negligible with respect to unity. In addition, the Tollmien-Schlichting modes from stability analysis performed later in the section depict typical incompressible features for the low subsonic case.

4.1.1 Compressible boundary layer solver

The CBL solver uses an implicit finite difference marching in space starting with an Illingworth-Levy transformed Blasius profile (Eq. (3.1.1)) for an upstream located station, $x/l = \mathcal{O}(1)$. The method has been proposed by White [1991] for the evaluation of two-dimensional compressible laminar boundary layers.[1] It assumes that the wall-normal velocity $\overline{V}$ and the streamwise derivatives ∂_x are small with respect to the streamwise velocity $\overline{U}$ and the wall-normal derivatives ∂_y, respectively. Consequently, the compressible NSE for steady developing boundary layer degenerates into:

$$\begin{aligned}
&\text{Continuity:} && \tfrac{\partial}{\partial x}(\overline{\rho}\overline{U}) + \tfrac{\partial}{\partial y}(\overline{\rho}\overline{V}) && = 0, \\
&x\text{-momentum:} && \overline{\rho}\big(\overline{U}\tfrac{\partial \overline{U}}{\partial x} + \overline{V}\tfrac{\partial \overline{U}}{\partial y}\big) && \approx -\tfrac{\partial \overline{P}_e}{\partial x} + \tfrac{\partial}{\partial y}(\overline{\mu}\tfrac{\partial \overline{U}}{\partial y}), \\
&y\text{-momentum:} && \tfrac{\partial \overline{P}}{\partial y} && \approx 0, \\
&\text{Energy:} && \overline{\rho}\big(\overline{U}\tfrac{\partial \overline{h}}{\partial x} + \overline{V}\tfrac{\partial \overline{h}}{\partial y}\big) && \approx \overline{U}\tfrac{\partial \overline{P}_e}{\partial x} + \tfrac{\partial}{\partial y}\big(\overline{k}\tfrac{\partial \overline{T}}{\partial y}\big) + \overline{\mu}\big(\tfrac{\partial \overline{U}}{\partial y}\big)^2,
\end{aligned} \tag{4.1.1}$$

where $\overline{P}_e$ is the inviscid pressure at the edge of the boundary layer evaluated with the Bernoulli equation through

$$\frac{\partial \overline{P}_e}{\partial x} = -\overline{\rho}_e \overline{U}_e \frac{\partial \overline{U}_e}{\partial x} = \overline{\rho}_e \frac{\partial \overline{h}_e}{\partial x}. \tag{4.1.2}$$

Considering a calorically perfect gas, the thermodynamic relations (Eq. (3.1.4)) used for the parallel Blasius remain valid as well as the Sutherland law (Eq. (3.1.5)) for the viscosity. Initially, the only known variables are $\overline{U}_e$, $\overline{\rho}_e$, $\overline{T}_e$ (freestream) and the no-slip and adiabatic conditions are imposed at the wall.
To ensure high accuracy, a third order backwards difference scheme is used in the x-direction, while Chebyshev spectral collocation is applied in the wall-normal direction.

[1] For developing boundary layer, the ξ-and η-direction of the BiGlobal grid denote the streamwise x-and wall-normal y-direction of the base flow.

Both boundary layers are exactly evaluated on the BiGlobal grid to avoid interpolation of the base flow for stability analysis and keep the accuracy as high as possible. Nevertheless, as the solver starts with an initial Illingworth-Levy profile imposed at the most upstream station, the following downstream locations show some dependency with respect to this initial condition. To avoid this effect, the number of points in the streamwise direction has to be extremely large ($N_x \approx 10^5$) such that it is infeasible to use the base flow grid exactly for the BiGlobal due to a memory limit; $N_\xi \times N_\eta = 7500$ is the maximum allowed. To circumvent this issue and to compute a high accuracy solution of the base flow on the BiGlobal grid, even in the streamwise direction, the flow is reconstructed by using only the last station of the CBL solver. Consequently, the CBL solver evaluates N_ξ times a developing boundary layer for which the last x-station corresponds to one streamwise collocation node of the BiGlobal grid. Finally, the base flow grid consists of $N_x = 150$ points in the x-direction and $N_y = 2N_\eta - 1$ in the wall-normal direction where $N_\eta = 50$ reveals already converged results (see section 4.2.3). Such implementation allows having a high accuracy solution for the stability analysis without interpolating the BiGlobal collocation grid on the base flow.

For the incompressible case, three domain heights are used to conduct a parameters study; $y/l \in [0, 25]$,$[0, 50]$ and $[0, 75]$. On the other hand, for the supersonic boundary layer, $y/l \in [0, 25]$ and $[0, 200]$ are used. For both cases, the small domain ($y_{max}/l = 25$) enhances the presence of spurious modes, giving the opportunity to apply different boundary conditions in order to remove them. The highest domain $y/l \in [0, 200]$, used only for the supersonic boundary layer, is exactly the same as for the future SWBLI cases where a significant height is needed to let the separation bubble properly grow in the wall-normal direction. The largest domain is, therefore, considered to compare the different cases (SWBLI, boundary layer; CBL or DNS solvers) and to perform physical analyses.

In order to map the collocation points in the physical space, the two mappings presented in section 2.2.5 are used. The one proposed by Malik [1990] is applied to all the cases in the y-direction except for the supersonic boundary layer with the highest domain. The parameter y_i of the mapping of Malik [1990] is set such that half of the points are mapped in the boundary layer. This implies that $y_i/l = 5$ and $y_i/l = 6$ for subsonic and supersonic cases, respectively. For the domain $y/l \in [0, 200]$, the bi-quadratic mapping is used in order to be again in agreement with the BiGlobal grid of the SWBLI where the separation bubble has to be well-resolved. Therefore, the mapping parameters in the wall-normal direction are $y_{i1}/l = 10$ and $y_{i2}/l = 30$. On the other hand, for the streamwise direction, the bi-quadratic mapping is always applied. For all the cases, except the highest domain, the streamwise direction is equitably divided, i.e. $x_{i1} = 1/3x_{max}$ and $x_{i2} = 2/3x_{max}$. For the supersonic boundary layer with $y_{max}/l = 200$, the parameters of the bi-quadratic mapping are again selected identical to the SWBLI case, such that the grid around the bubble is properly refined in the x-direction. It leads to $x_{i1}/l = 1820$ and $x_{i2}/l = 1995$. All the details about the highest domain (i.e the SWBLI domain) are discussed later in chapter 5.

For the different base flows, the residual levels of the CBL solver are evaluated with

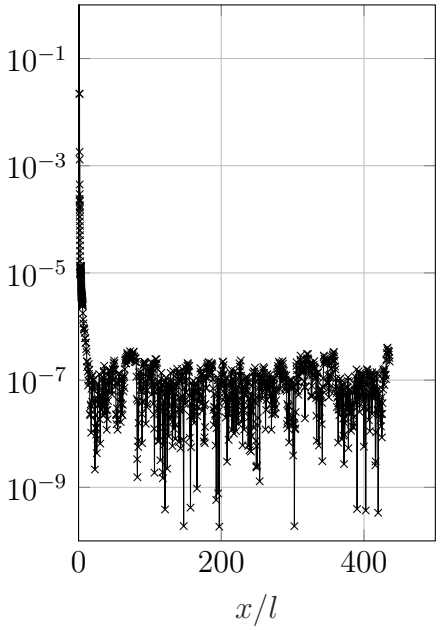

(a) First station from the leading edge $x/l = 435$.

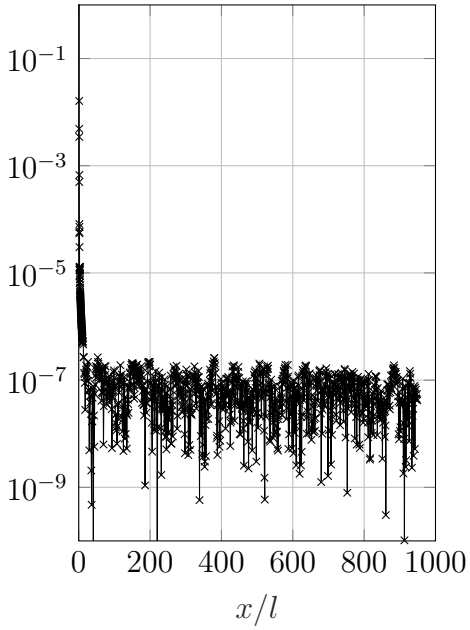

(b) Last station from the leading edge $x/l = 949$.

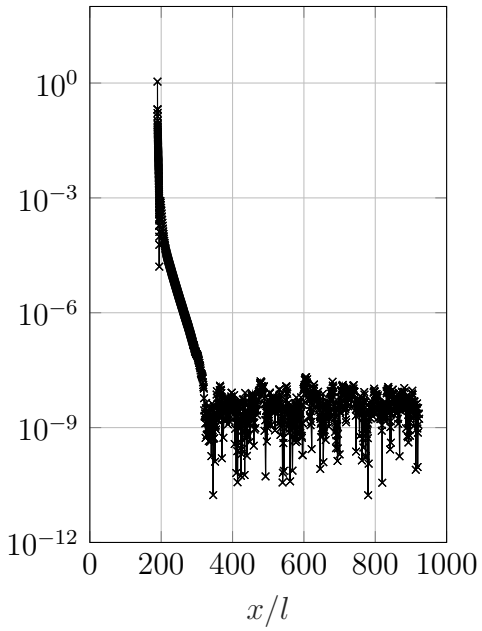

(c) First station from the leading edge $x/l = 923$.

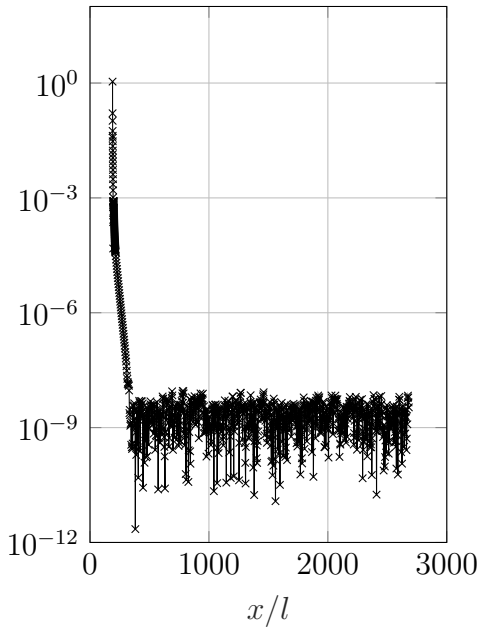

(d) Last station from the leading edge $x/l = 2681$.

Figure 4.1.1: Heat imbalance $|\overline{\mu}\overline{U}_y^2 + \overline{k}_T + \overline{kT}_{yy}|$ of the CBL solver at different streamwise stations. (a,b) for low subsonic case ($M = 0.1$) and (c,d) for supersonic case ($M = 1.7$) with $y_{max}/l = 25$.

the force imbalance and the heat imbalance at the wall. The latter, which reveals the highest residual level, is shown in Fig. 4.1.1 for supersonic and low subsonic boundary layers at the first and the last streamwise station of the BiGlobal domain. Fig. 4.1.1 considers the lowest domain ($y_{max} = 25l$), but the height does not show an influence on the residual behaviour. For the $M = 0.1$ case, the wall heat imbalance reveals an accuracy about 10^{-7}, while the force imbalance, not shown for sake of clarity, is about 10^{-11}. Regarding the supersonic case, both heat and force imbalances exhibit a 10^{-9} residual level.

4.1.2 Direct numerical simulations

The purpose of conducting DNS is to later represent the shock impinging on the developing boundary layer for the SWBLI cases. Having the same simulation without the shock allows, therefore, to carry out a proper comparison between the spectra of the boundary layer and of the SWBLI. The numerical set-up of the DNS case is exactly similar to the SWBLI and detailed justifications can be found in chapter 5. On the other hand, a second boundary layer base flow gives the opportunity to compare the BiGlobal results between DNS and CBL solvers. Using different methods leads to inevitable infinitesimal discrepancies, suggesting an analysis of sensitivity of the stability results.

Due to the resolution fixed in the DNS, the grid cannot be the same as the BiGlobal one. Moreover, the domain size is different in order to avoid the base flow boundary conditions to affect the stability results. Therefore, a spline interpolation between the DNS grid $(x, y)/l \in [758.4, 3121.4] \times [0, 250]$ and the BiGlobal grid $(x, y)/l \in [923, 2681] \times [0, 200]$ is performed. The DNS domain comprises $(N_x \times N_y) = (1000 \times 500)$ points. Physically, the flat plate used for DNS corresponds to the case described by Giepman [2016] with a domain starting at 20mm from the leading edge. The grid distribution is uniform in the x-direction and is hyperbolic for the wall-normal direction. Close to the wall, the entire boundary layer is resolved with $y^+ = 1$. All boundary conditions are based on the Riemann invariant, in order to avoid shock reflections at the boundaries, except at the wall where the no-slip and adiabatic conditions are enforced. In addition to the Riemann condition, a Blasius profile is imposed at the inlet of the domain. The DNS solver is initialised with a boundary layer evaluated at the different streamwise locations with a compressible flat plate self-similarity law.

The current DNS solver, INCA, is based on a finite volume method where the viscous fluxes are evaluated with a second order central scheme while the third order accuracy Harten-Lax-van Leer-Contact (HLLC) solver is used for the convective fluxes. Since it does not reveal to be necessary with the HLLC scheme, limiters are not used to ensure high accuracy. The current numerical set-up allows converging to a residual level of 10^{-14}, based on the governing momentum and energy equations.

Comparison of DNS and CBL base flows

The two supersonic base flows, evaluated with the DNS and the CBL solvers on the highest domain, are compared in Fig. 4.1.2 through the temperature $\overline{T}$, $\overline{U}$ and $\overline{V}$ profiles. Note the different scaling and heights used in Fig. 4.1.2. It reveals that both methods

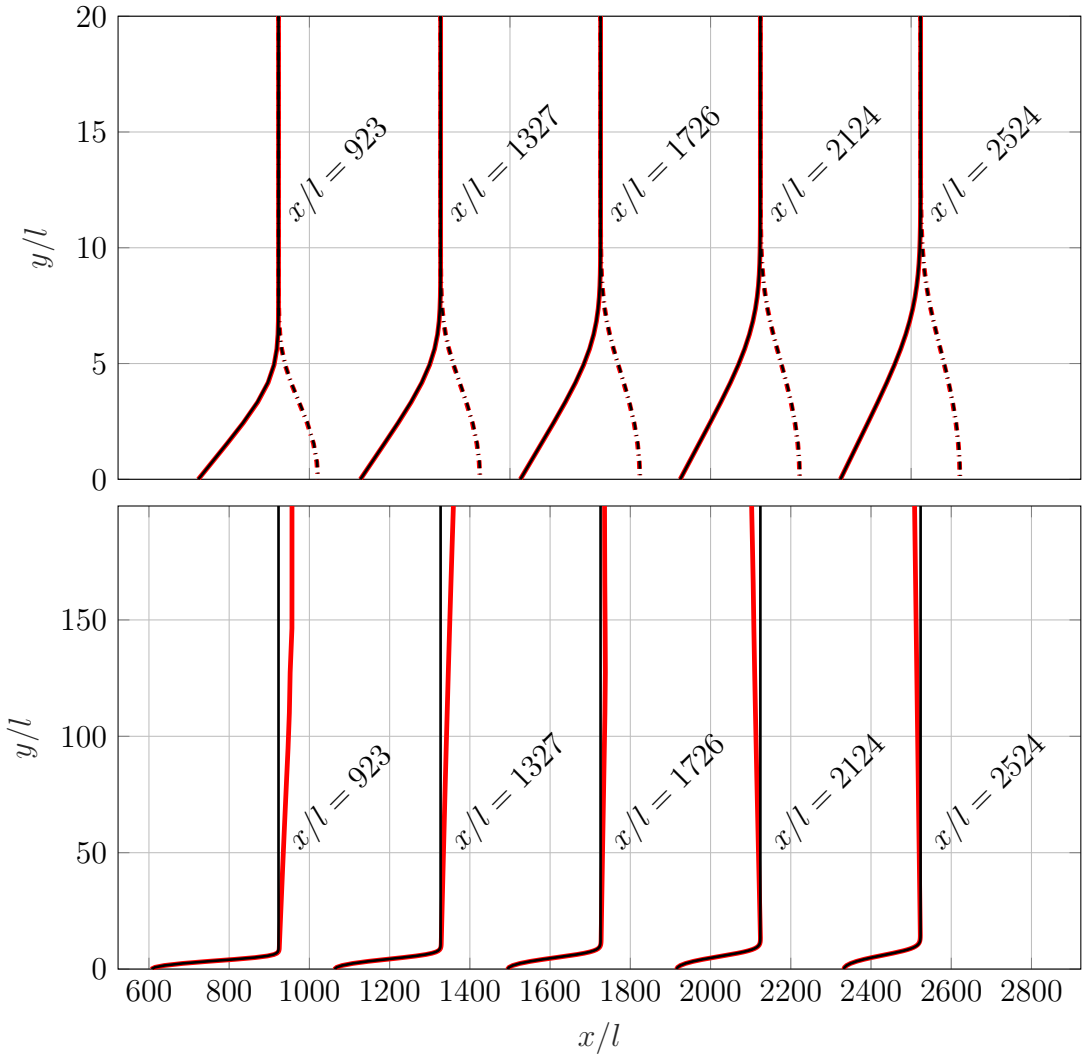

Figure 4.1.2: Supersonic boundary layer ($M = 1.7$): Profiles of $\overline{U}/\overline{U}_e$ (top, continuous line), of $\overline{T}/\overline{T}_e$ (top, dash dotted line), magnified by a factor 200 and of $\overline{V}/\overline{U}_e$ (bottom), magnified by a factor 2×10^5 evaluated with CBL solver (black) and DNS (red). Note the different vertical scales for $\overline{U}/\overline{U}_e$ and $\overline{V}/\overline{U}_e$.

provide very similar results along the entire wall. The largest difference (about 10^{-4}) in the $\overline{U}$ and $\overline{T}$ profiles is located in the region $y/l \in [5, 6.5]$. Regarding the wall-normal velocity $\overline{V}$, the same absolute difference is noticeable in the freestream, while a 10^{-5} difference exists close to the wall. In the freestream, the wall-normal velocity must be constant as it is perfectly represented by the CBL solver whereas the DNS reveals fluctuations. Such behaviour is due to a slight compression wave caused by the growing boundary layer.

Despite the small differences existing in the base flow, the sensitivity of the BiGlobal equations could induce significant discrepancies of the stability results for the CBL and the DNS solvers. Since the dominant part of the TS modes is close to the wall, it is expected that the freestream condition does not influence their representation significantly.

Therefore, the potential discrepancies between the two spectra should mainly be induced by the streamwise velocity as the maximum differences appear in the corresponding shear layer.

4.2 Parameter study on the BiGlobal set-ups

In this section, the stability analyses are carried out with the small domains for incompressible and compressible boundary layers. The aim is to observe the influence of the boundary conditions and of the domain height on the TS modes. For both cases, only the base flows with the implicit solver are used. Performing such parametric study is worthwhile to determine the best numerical set-up for the future SWBLI cases. Finally, a convergence analysis of the temporal spectra is conducted in both directions.

4.2.1 Influence of the boundary conditions

In case of streamwise flows where modes are prone to travel across the inlet and outlet boundary, the choice of boundary conditions is important. Rodriguez [2010], Pinna [2012], Groot [2013] use Robin boundary conditions. This imposes a fixed wavelength at the boundaries in order to represent the modes travelling through and, therefore, it consists of an intermediate solution between the Dirichlet and the Neumann conditions. However, it adds parameters to select and the results must be more or less known a priori. In the present well-known cases of developing boundary layers, assigning such boundary conditions is feasible, but the final aim is to apply a similar set-up to SWBLI where the modes are unknown. An alternative is the Neumann condition applied for each perturbation components at the inlet and outlet boundaries. The drawback of enforcing zero gradient at a boundary is to constrain the modes being constant at this location. Consequently, the overall modes can exhibit biased decay/growth. Furthermore, dealing with waves, the use of the Neumann condition at the inlet/outlet is equivalent to impose the spatial periodicity of the modes in the streamwise direction. Nonetheless, it shows up to be the most adapted for the current developing boundary layers and, later, for the SWBLI. Due to the lack of other possibilities for the inlet and outlet boundaries, the following section focuses on the boundary conditions applied at the top and bottom extremities in order to represent as good as possible the TS modes.

Pressure compatibility condition and spurious modes

At the bottom of the domain, the no-slip condition is imposed by zeroing the velocity and the temperature fields (i.e. Dirichlet condition) to represent the solid wall. The same boundary conditions are applied at the top, similar to the parallel Blasius case. However, there is no physical formulation for the pressure at these locations. An approach proposed by Theofilis and Colonius [2004] consists of imposing the pressure at boundaries by incorporating a staggered grid. The continuity equation is evaluated on Chebyshev-Gauss points, while the momentum and energy equations are evaluated on the Chebyshev-Gauss-Lobatto collocation nodes. The method has been successfully used

by Robinet [2007] and Theofilis and Colonius [2004] but requires interpolation to evaluate the variables on the different node sets, introducing a source of error. Moreover, spurious mode due to the behaviour of the pressure at boundary exists.
Another widely used approach consists of imposing the PC boundary closure but, as already shown with parallel Blasius cases, it introduces spurious modes. In addition to providing a less clean spectrum, they may add a spurious oscillatory component to other physical modes. Therefore, in order to filter them, it is relevant to understand the origin of these modes as well as the dominant factors which influence their presence in the spectrum. The main features of the spurious modes are the oscillations present in the perturbation field, mainly $\tilde{v}$, and the large pressure jump at the first point on the wall. Fig. 4.2.1 depicts one of the pressure mode present in the incompressible spectrum when the PC boundary closure is applied to both top and bottom walls.

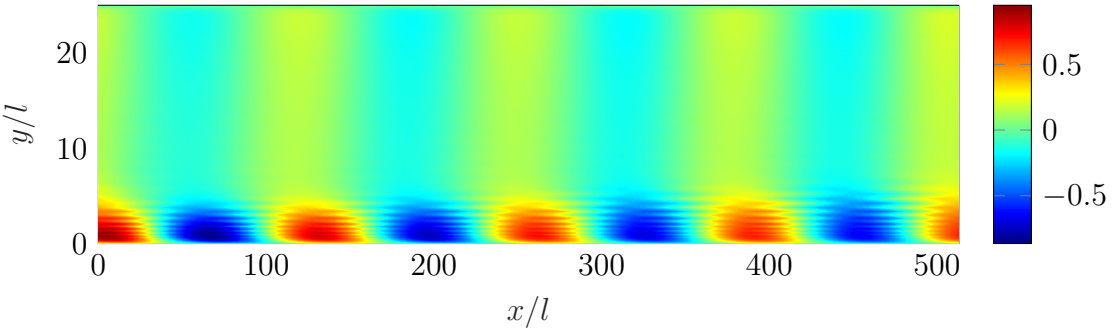

(a) $\Re(\tilde{u})/|\tilde{u}|_{max}$ perturbation.

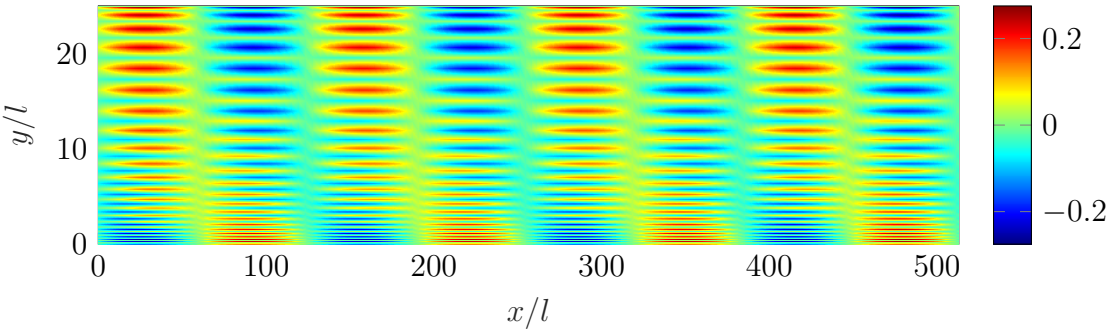

(b) $\Re(\tilde{v})/|\tilde{u}|_{max}$ perturbation.

Figure 4.2.1: Low subsonic boundary layer ($M = 0.1$): contour plot of spurious mode $\omega = 0.0448 + 0.0190i$.

In order to have a better interpretation of the spurious pressure modes, a common characteristic is identified through the Reynolds-Orr energy equation. It is depicted in Fig. 4.2.2, where the largest terms of the BiGlobal equations acting on several spurious modes are shown. The ω_i-budget reveals that the modes are ruled by six contributions. Considering the Stokes assumption for the second viscosity, the diffusive terms $\tilde{v}_{yy}$ are linearly dependent. Consequently, $\tilde{p}_y$ is larger than $|(2\overline{\mu} + \overline{\lambda})/Re\tilde{v}^*\tilde{v}|$ and constitutes the term prevailing in the spurious modes. In point of fact, the pressure gradient $\tilde{p}_y$ is a consequence of the very strong discontinuity of $\tilde{p}$ near the wall, indicating a causal relation with the PC equation (Eq. (2.2.41)). Accordingly, a high correlation (larger than 99.99%) is found between the diffusive terms $\tilde{v}_{yy}$ and the wall-normal pressure gradient

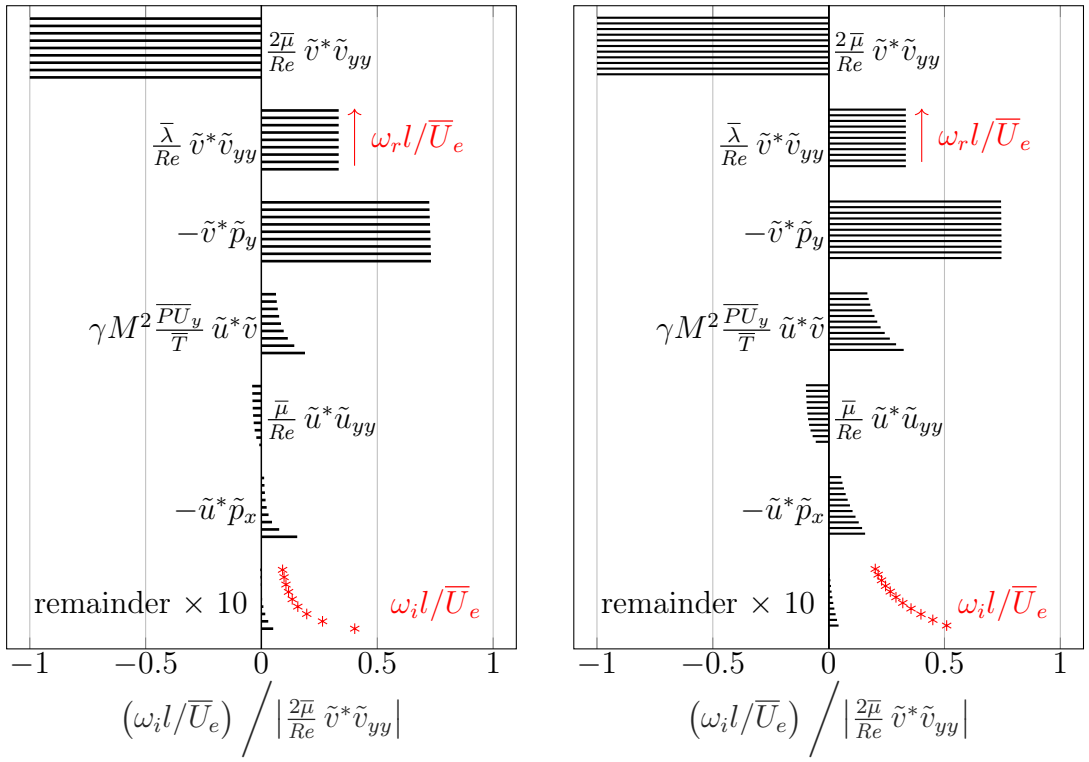

(a) Subsonic boundary layer ($M = 0.1$). (b) Supersonic boundary layer ($M = 1.7$).

Figure 4.2.2: Most dominant Reynolds-Orr balance terms for typical spurious pressure modes: ω_i-budgets normalized by the largest contribution. Imaginary part of eigenvalues themselves ($*$) and increasing real part indicated by the arrows. The remainders are magnified by a factor 10.

revealing a proportionality factor of -0.717 and -0.745 for the subsonic and supersonic case respectively. In the remainder, magnified by a factor ten, other wall-normal derivatives with respect to $\tilde{u}$, $\tilde{v}$ and $\tilde{T}$, are highly correlated ($\geq 99\%$) with the three largest contributions. However, these terms are individually two orders of magnitude smaller than the most significant ones. Additionally, while $\tilde{v}_{yy}$ and $\tilde{p}_y$ are in the y-momentum equation, the Reynolds-Orr energy balance highlights three other large contributions originating from the x-momentum equation. The diffusion $(\overline{\mu}/Re)\tilde{u}^*\tilde{v}$ remains almost constant over the frequency range. On the other hand, approaching the imaginary axis, the Reynolds stress $\gamma M^2 \frac{\overline{P}}{\overline{T}}\,\tilde{u}^*\tilde{v}\overline{U}_y$ and the pressure work $\tilde{u}^*\tilde{p}_x$ increase so to become extremely large when $\omega_r l/\overline{U}_e \to 0$, indicating a strong structural change in the spurious modes where the oscillations are quite small. It justifies that the energy budget does not consider the two spurious eigenvalues close to the imaginary axis as depicted in Fig. 4.2.3 and Fig. 4.2.4. Therefore, the six contributions depicted in Fig. 4.2.2 are the main signature of the remaining spurious modes.
Furthermore, in the spectrum of streamwise case, the spurious modes are easily identifiable by a branch located at an almost constant growth rate as shown in Fig. 4.2.3 and Fig. 4.2.4.

Application of the linearised pressure Poisson equation

According to Theofilis [2017], the use of the LPPE circumvents the previously cited issues for the incompressible BiGlobal and TriGlobal stability problems. The spurious pressure modes then do not occur amongst the eigensolutions, yielding a clean spectrum, while the solution accuracy is preserved. The mathematical approach related to the adaptation of LPPE to the compressible BiGlobal equations can be found in section 2.2.7. In the current section, the effect of the LPPE imposed at wall and freestream is analysed with respect to compressible BiGlobal equations.

First of all, the incompressibility hypothesis underlying the LPPE should be imperatively taken into account. Theoretically, the LPPE can only be applied where the divergence of the instantaneous velocity Q is zero in order to strictly respect the assumption of the Poisson equation for the pressure. Therefore, it can be undoubtedly applied at solid walls where the amplitude of the modes reaches zero. In addition, in the freestream of developing boundary layers, the base flow velocity $\overline{Q}$ is uniform and satisfies the divergence free assumption, while it is invalid for the perturbations variables q'. Despite the divergence free condition being not respected at the top boundary in general, the LPPE is used at this location for both incompressible and supersonic boundary layers in order to complete the parametric study and to determine its impact on the spectrum.

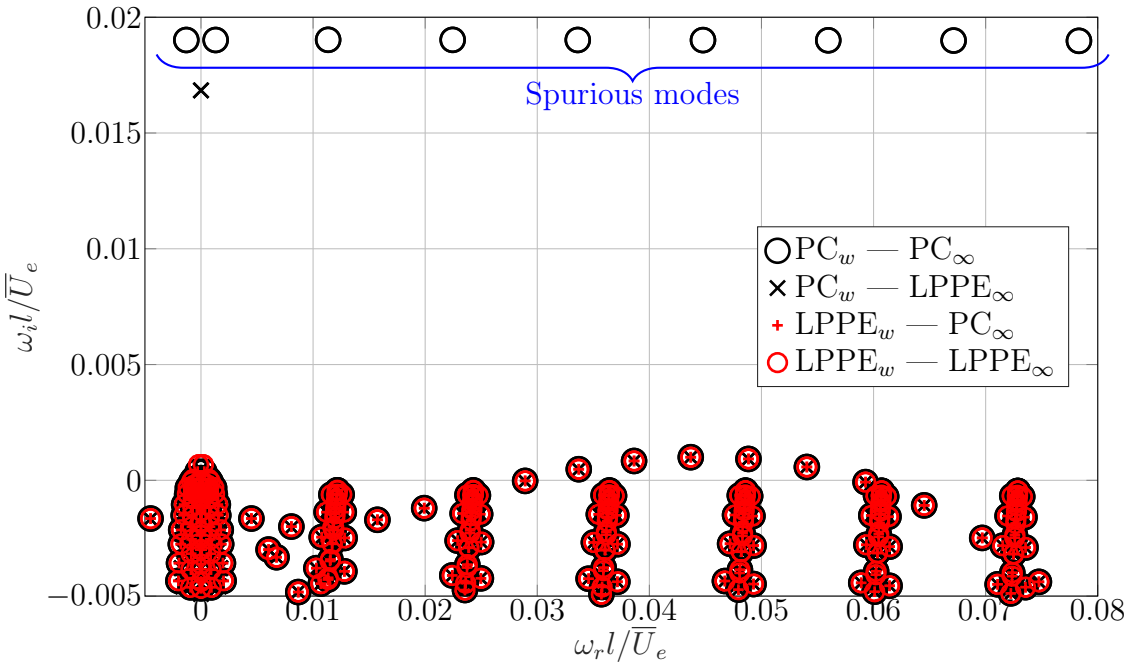

Figure 4.2.3: Low subsonic boundary layer ($M = 0.1$): spectra with PC or LPPE boundary conditions applied at wall (w) or freestream (∞).

The incompressible BiGlobal spectrum, comprising the TS branch, is depicted in Fig. 4.2.3 with the combinations of LPPE and PC boundary conditions. The spurious pressure modes exist only if the PC equations are applied on both boundaries. When the LPPE is applied at least one boundary, the spurious modes are removed. Applying

$y=0$		$y=y_{max}$	$\omega_i l/\overline{U}_e \times 10^4$	$\omega_r l/\overline{U}_e \times 10^2$
PC	—	PC	9.98327	4.36928
LPPE	—	PC	9.98257	4.36927
PC	—	LPPE	9.94716	4.36853
LPPE	—	LPPE	9.97677	4.36926

Table 4.2.1: Low subsonic boundary layer ($M = 0.1$): most unstable Tollmien-Schlichting eigenvalue.

it at both wall and freestream demonstrates that the spurious modes are not caused by the symmetry in the conditions. The use of LPPE instead of the PC boundary closure at the wall induces, as shown in Tab. 4.2.1, an absolute difference of about 10^{-8} for both imaginary and real parts on the most unstable eigenvalue of the TS branch. On the other hand, imposing the LPPE at the freestream boundary has a more significant impact on the results. Tab. 4.2.1 shows an absolute difference of about 10^{-6} and 10^{-5} for the imaginary and real parts, respectively, compared to PC closure. While the eigensolver precision is independent from the boundary condition of the freestream, it reveals $\epsilon_{crit} = 10^{-12}$ and $\epsilon_{crit} = 10^{-10}$ for PC and LPPE applied at the wall, respectively.

The spectrum of the supersonic boundary layer is shown in Fig. 4.2.4, where the LPPE has been applied in the freestream as well. Similarly to the subsonic case, applying the LPPE at one or two boundaries removes the spurious modes from the spectrum. When the LPPE replaces the PC boundary closure at the solid wall, a 10^{-7} absolute difference on both imaginary and real parts of the eigenvalue is distinguishable for the most unstable TS mode. On the other hand, considering the same mode, the impact of the LPPE boundary closure at freestream is about 10^{-5}. It is due to the divergence free condition on the perturbation variables, which is not fully satisfied at this location. Tab. 4.2.2 summarises the $\omega l/\overline{U}_e$ of the most unstable TS mode for different combinations of boundary conditions at wall and freestream boundaries. Finally, it is concluded that the LPPE is effective for both supersonic and subsonic flows, when applied to the solid wall, where the incompressibility hypothesis underlying the Poisson equation is fully satisfied.

$y=0$		$y=y_{max}$	$\omega_i l/\overline{U}_e \times 10^4$	$\omega_r l/\overline{U}_e \times 10^2$
PC	—	PC	1.71563	3.13677
LPPE	—	PC	1.71735	3.13686
PC	—	LPPE	1.84313	3.13931
LPPE	—	LPPE	1.76049	3.13682

Table 4.2.2: Supersonic boundary layer ($M = 1.7$): most unstable Tollmien-Schlichting eigenvalue

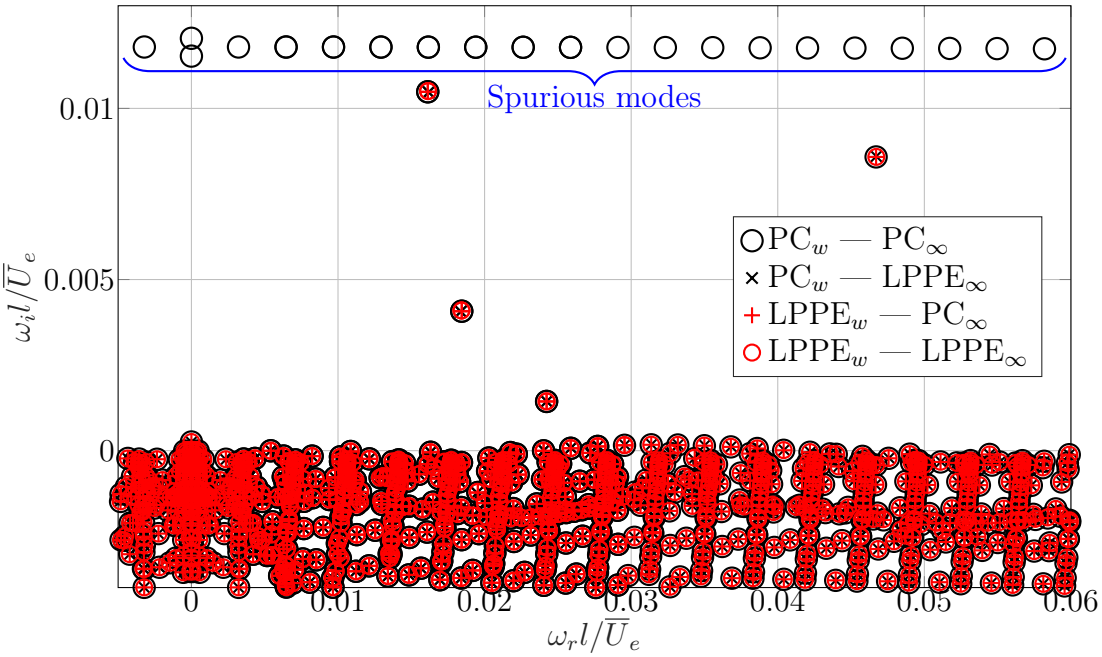

Figure 4.2.4: Supersonic boundary layer ($M = 1.7$): spectra with PC or LPPE boundary conditions applied at wall (w) or freestream (∞).

Neumann conditions

Instead of zeroing the modes amplitude at the freestream boundary, the Neumann condition is used for all the perturbation variables as a separate case. Nevertheless, that boundary condition has to be applied taking care that the resulting decay/growth of the modes as $y \to \infty$ can strongly depend on the domain height. For instance, the TS modes studied in the current thesis have a decay in the freestream which is expressed analytically (Balakumar and Malik [1992]):

$$e^{-y\sqrt{\alpha^2+\beta^2-(\alpha-\omega)^2M^2}}, \qquad \text{for } Re >> 1 \text{ and } Pr = \frac{3}{4}. \tag{4.2.1}$$

Therefore, the Neumann conditions can provide only trusted results if the domain is sufficiently high; the amplitude of the modes at the top boundary has to be close to zero. In the following, the effect of the Neumann condition on the spectrum is analysed for both compressible and incompressible boundary layers with the small domain height $y_{max}/l = 25$.

In Fig. 4.2.5, the influence of the Neumann conditions on the incompressible spectrum is depicted. Similarly to the LPPE, enforcing zero-gradient at the top boundary removes the spurious modes. However, it influences the other (physical) modes as clearly shown by the TS branch. When approaching the imaginary axis, the frequency $\omega_r l/\overline{U}_e$ decreases at the same time as the streamwise wavenumber. The linear relation between both is the group speed $c_{gr} = \partial\omega_r/\partial\alpha_r \approx 0.4$ for the subsonic case. Coupled with Eq. (4.2.1), it shows that reducing the frequency yields to a decrease in the decay rate of the TS modes. Therefore, the decay rate of modes with a small frequency deviates from the theoretical value due to Neumann condition. On the other hand, the combination of the LPPE at the wall and the Neumann condition at the top boundary shows a larger

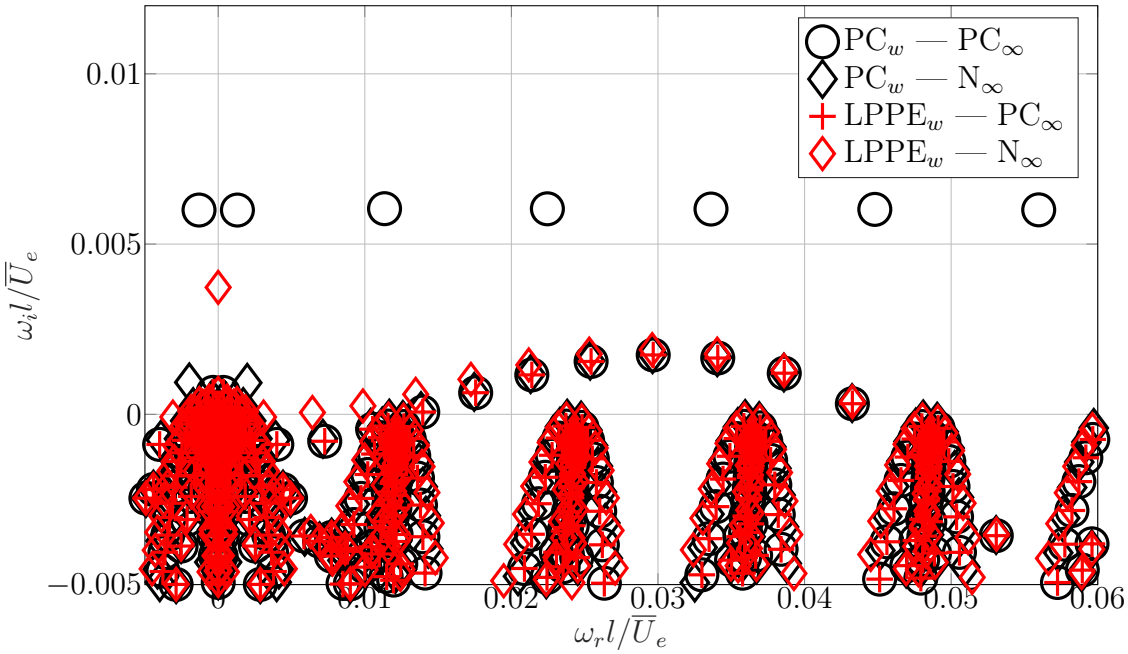

Figure 4.2.5: Low subsonic boundary layer ($M = 0.1$): spectra with PC or LPPE boundary conditions at wall (w). PC or Neumann (N) at freestream (∞).

difference than the combination with the PC at wall and Neumann for the freestream. It is most probably due to the difference existing between the manifestations of $\tilde{p}$ and $\tilde{v}$. These two variables reveal significantly smaller absolute values at the top boundary when the PC closure is applied at the wall for a small domain height. In other words, the small height and the application of the Neumann condition do not allow the TS mode to adapt properly inside the domain itself due to a strong dependency with respect to the boundaries.

Eq. (4.2.1) reveals that the decay becomes smaller with an increasing Mach number. Therefore, for the supersonic boundary layer having the same domain height as the incompressible case, the effect of the Neumann condition becomes significant as depicted in Fig. 4.2.6. Moreover, imposing zero-gradient at the freestream adds other spurious modes that interact with the TS branch. For the current compressible boundary layer, the Neumann condition is clearly not applicable for such a small domain. A combination of PC/LPPE must be used in order to accurately represent the physical behaviour of the TS mode. A similar conclusion has been drawn by Groot [2013] about the freestream boundary conditions for the parallel Blasius. This justifies not to investigate more about the application of such top boundary conditions. Finally, all the stability analyses conducted in following sections use the LPPE at the solid wall and the PC boundary closure for the freestream.

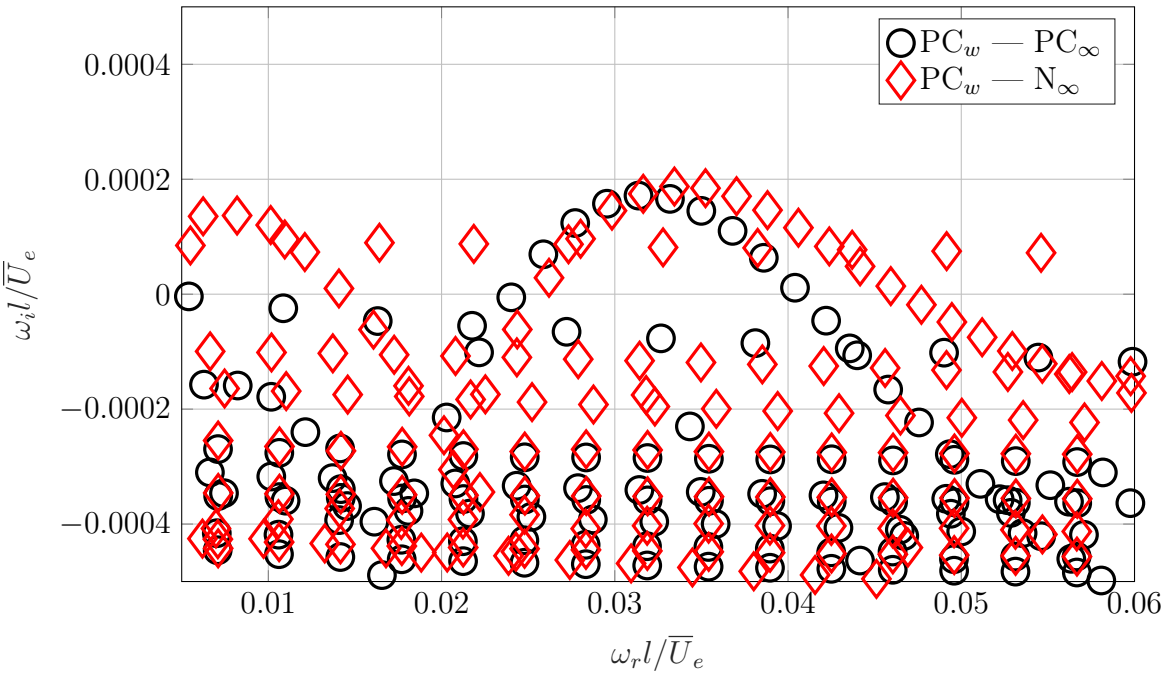

Figure 4.2.6: Supersonic boundary layer ($M = 1.7$): Zoom on TS-waves branches of the spectra with PC or LPPE boundary conditions at wall (w) and PC or Neumann (N) at freestream (∞).

4.2.2 Influence of the domain height

As shown previously by Eq. (4.2.1) for the TS modes, the decay of modes must be respected to represent their physical behaviour properly. In addition to the boundary conditions, it is relevant to analyse briefly the effect of the domain height. In the current section, only the incompressible case is considered because of the cleaner spectrum in the first place, yielding the TS branch easily identifiable. Nevertheless, the conclusions about the domain height are similar for both flow regimes.

In Fig. 4.2.7, three different domain heights are shown with the LPPE applied at the wall and the PC boundary closure at the freestream. It highlights that, even with the Dirichlet condition on the velocity components and the temperature, the behaviour of the TS branch is influenced by the height. By increasing it, a fast convergence of the modes close to the imaginary axis is observed. It implies that theses modes can reach a value sufficiently close to zero at the top boundary of the domain. On the other hand, the modes with a higher frequency content are subject to a larger decay such that the domain height does not have a significant impact on the results.

The same observation can be done in Fig. 4.2.8, where the pressure is imposed with the LPPE closure at the wall, while the Neumann condition is applied at the freestream boundary. A quite fast convergence is found with respect to the increasing height although the growth rate of the low-frequency modes is more over-estimated than with the previous LPPE-PC case. In addition, a new branch crossing the TS modes appears when the domain height is increased. As the related mode shape present oscillations, it is argued that this spurious branch is due to the decreased resolution caused by the increased height.

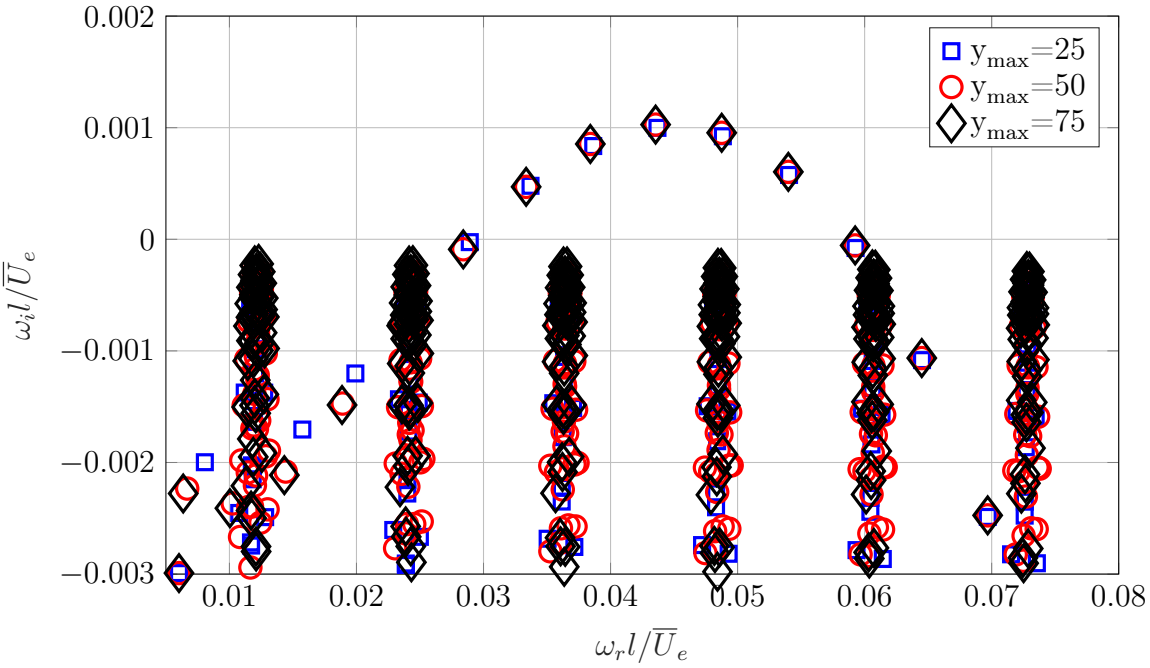

Figure 4.2.7: Low subsonic boundary layer ($M = 0.1$): Spectra for different domain heights with LPPE at wall and PC at freestream.

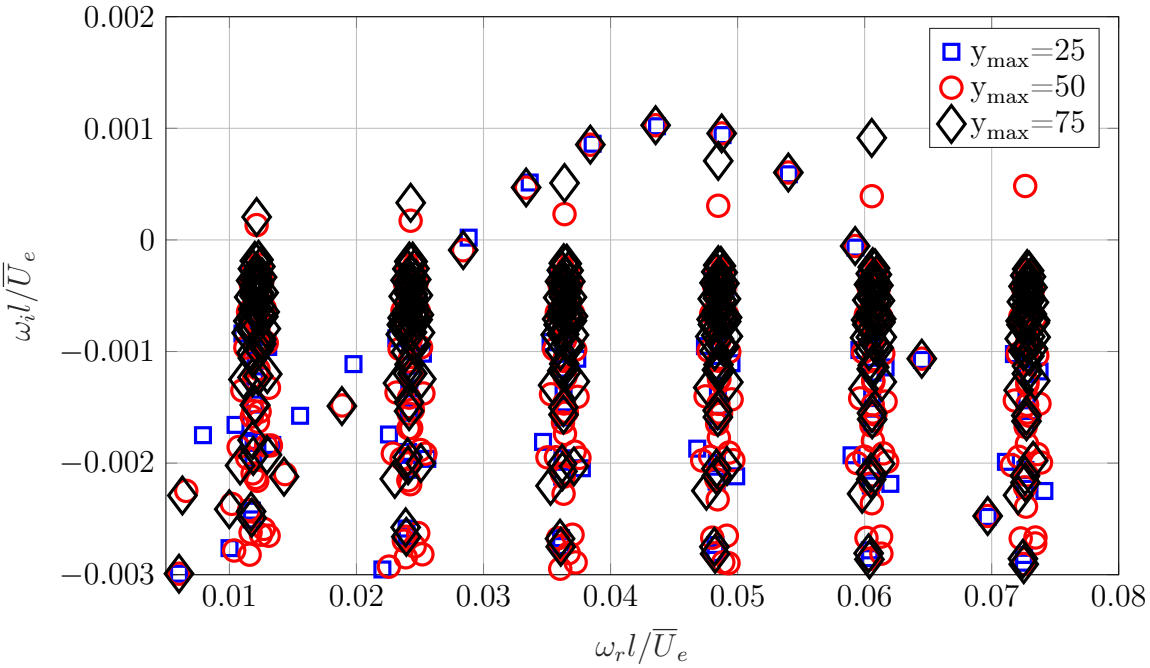

Figure 4.2.8: Low subsonic boundary layer ($M = 0.1$): Spectra for different domain heights with LPPE and Neumann boundary conditions at wall and freestream, respectively.

Finally, in view of the negligible difference existing between $y_{max}/l = 25$ and the other heights for most of the eigenvalues lying on the TS branch, the former is chosen for further consideration in combination with the LPPE at wall and PC at freestream

for the low subsonic case. Selecting such a small domain allows increasing the resolution in the freestream significantly. Concerning the compressible boundary layer, the same set of boundary conditions is chosen, but due to the very low decay of the TS mode, the use of $y_{max}/l = 200$ is justified.

4.2.3 Convergence analysis

In order to ensure accurate results, a convergence analysis is performed. For sake of clarity, only the low subsonic boundary layer is shown in this section but the same conclusions have been drawn for the supersonic case. Moreover, the current case consists of the smallest domain with the LPPE applied at the wall and the PC closure at freestream. The convergence analysis, focusing on the TS branch, is conducted for both x and y-directions. In Fig. 4.2.9, the convergence in the streamwise direction is shown. The y-direction is under-resolved to be able to increase N_ξ from 150 to 200 without exceeding available memory ($\approx$ 150Gb). Increasing N_ξ reveals a linear movement of the spectrum. Therefore, the streamwise resolution should be increased such as $N_\xi > 200$. This lack of convergence of continuous modes in the streamwise direction is a well-known issue by the hydrodynamic stability community (Alizard and Robinet [2007]; Ehrenstein and Gallaire [2005]; Åkervik et al. [2008]) but, nowadays, the computational power does not allow to have a better resolution. Consequently, all the results obtained from streamwise BiGlobal stability are generally under-resolved. It is important to note that the convergence of branches are always slower than the one of discrete modes as clearly shown with the parallel Blasius cases. This is a consequence of the in-/outflow dynamics of the modes.

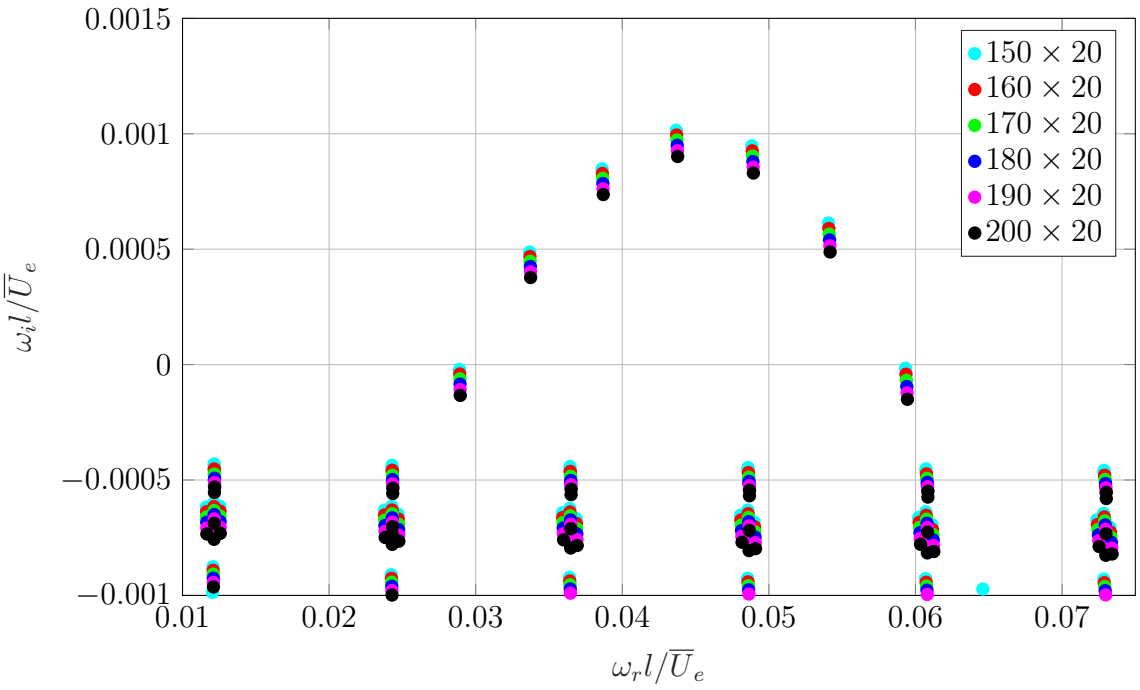

Figure 4.2.9: Low subsonic boundary layer ($M = 0.1$): convergence of the BiGlobal spectrum with respect to the streamwise direction N_ξ for fixed $N_\eta = 20$.

On the other hand, an increase of the number of points in the wall-normal direction, where perturbations are confined in the domain such that they do not outflow, is shown in Fig. 4.2.10 and reveals a higher convergence rate than in the streamwise direction. The difference of the most unstable TS mode between 40 and 50 collocation nodes in the y-direction is about 10^{-7} while the same is observed between 30 and 40 nodes. Consequently, the wall-normal direction is sufficiently resolved. The same conclusion is drawn for the supersonic boundary layer with the smallest domain. All the physical analysis of the next section are based on $(N_\xi, N_\eta) = 150 \times 50$ grids.

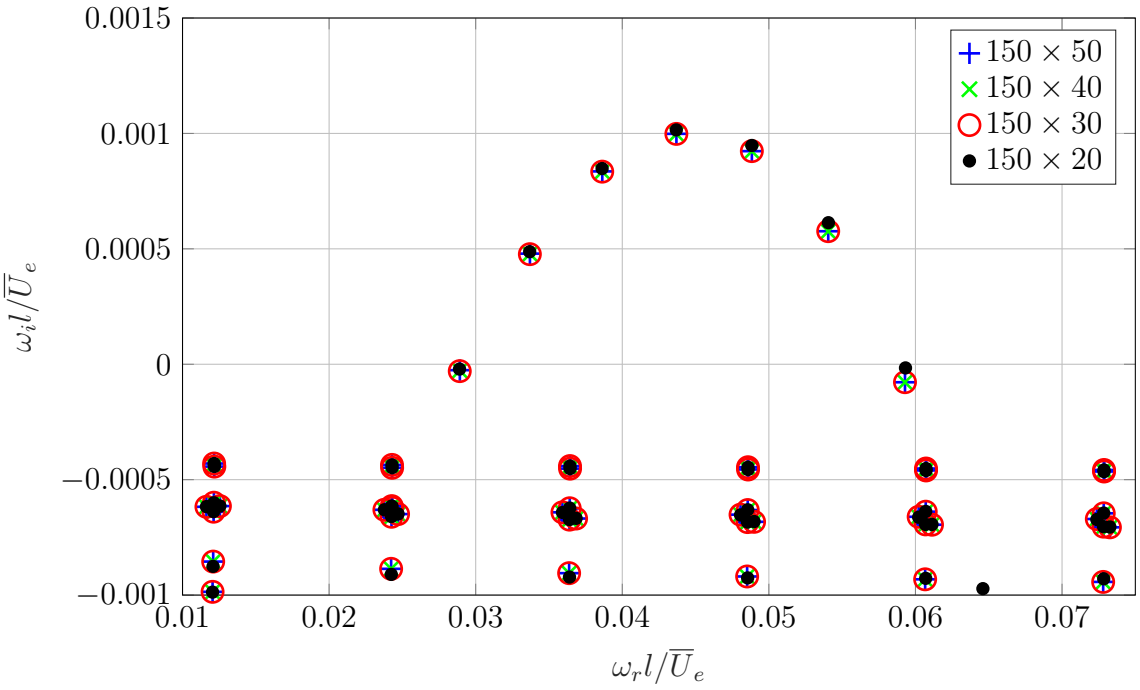

Figure 4.2.10: Low subsonic boundary layer ($M = 0.1$): convergence of the BiGlobal spectrum with respect to the streamwise direction N_η for fixed $N_\xi = 150$.

4.3 BiGlobal stability analysis

In the following section, the TS modes with $\beta = 0$ are analysed with a physical approach for both subsonic and supersonic boundary layers. In addition to the temporal feature ω of the modes, the spatial dimension is treated. Moreover, wave packets related to the TS modes are constructed. Based on the conclusion of the parameter study, the boundary conditions are Dirichlet at wall/freestream for all the perturbations, except LPPE and PC are used for the pressure on bottom and top, respectively. The Neumann condition is used for inlet/outlet. The domain height of the subsonic case is $y_{max}/l = 25$, while $y_{max}/l = 200$ is used for the supersonic case. Finally, the grids have $(N_\xi, N_\eta) = 150 \times 50$ collocation nodes.

4.3.1 Low subsonic boundary layer

In the spectrum depicted by Fig. 4.2.3, the continuous branch of the TS modes is clearly visible and all the temporal features (i.e ω) are directly obtained. However, there is no information about the spatial growth rate $\alpha_i l$ and wavenumber $\alpha_r l$ of each mode lying on the branch; it must be extracted from the two-dimensional modes themselves as described by Alizard and Robinet [2007] and Groot [2013]. Reminding that the perturbation field can be written:

$$q' = \tilde{q} e^{i(\beta z - \omega t)} = |\tilde{q}| e^{i\Theta(x,y)} e^{i(\beta z - \omega t)}, \tag{4.3.1}$$

where $\Theta(x, y)$ is the phase of a mode varying with respect to x and y between $-\pi$ and π. As reminder, β is the assumed constant wavenumber in the spanwise direction. The phase $\Theta(x, y)$ can be evaluated from one mode as follows:

$$\Theta(x, y) = \tan^{-1}\left(\frac{\tilde{q}_i}{\tilde{q}_r}\right). \tag{4.3.2}$$

According to Alizard and Robinet [2007], the dimensional streamwise wavenumber α is computed with:

$$\alpha_r(x) = \frac{\partial \Theta(x, y_{\tilde{q}_{max}})}{\partial x}, \tag{4.3.3}$$

where $y_{\tilde{q}_{max}}$ designates the coordinate y where the considered field $\tilde{q}$ reaches its maximum. On the other hand, the spatial growth rate α_i is evaluated as follows:

$$\alpha_i(x) = -\frac{1}{|\tilde{q}(x, y_{\tilde{q}_{max}})|} \frac{\partial \tilde{q}(x, y_{\tilde{q}_{max}})}{\partial x}. \tag{4.3.4}$$

In the current thesis, only the perturbation field $\tilde{u}$ is used to compute the spatial behaviour of the TS modes. For instance, Alizard and Robinet [2007] used both $\tilde{u}$ and $\tilde{v}$, but it returns exactly the same results.

The values obtained through Eq. (4.3.3) and Eq. (4.3.4) are compared in Fig. 4.3.1 to the spatial LST simulations carried out at each streamwise station of the BiGlobal base flow. At one x-station, providing to the one-dimensional stability equations a single ω of the TS branch and $\beta = 0$ returns the spectrum related to the wavenumbers α. A filter is then applied to identify the unique α related to the TS mode. The method is used at each streamwise location and for each ω of the TS branch in order to resolve the entire mode. Nevertheless, for sake of clarity, not all different ω along the TS branch are shown in Fig. 4.3.1. Note that solving the 2D base flow at different discrete locations with compressible LST equations assumes homogeneity (non-parallel effect) in the streamwise direction and, therefore, some minor differences are expected with the BiGlobal mode, where non-parallel effects are incorporated.

In Fig. 4.3.1, the values of $\alpha_i l$ from the LST are shown, which are always larger than the BiGlobal ones. This is due to the non-parallel effects, taken into account by the latter, which tend to destabilise the boundary layer. The discrepancies on $\alpha_i l$ are also due to different domain lengths used to extract the local spatial behaviour of the BiGlobal modes. A truncated domain avoids interpolating malicious boundary condition effects which are significant at the inlet of the domain. It is depicted in Fig. 4.3.2 and

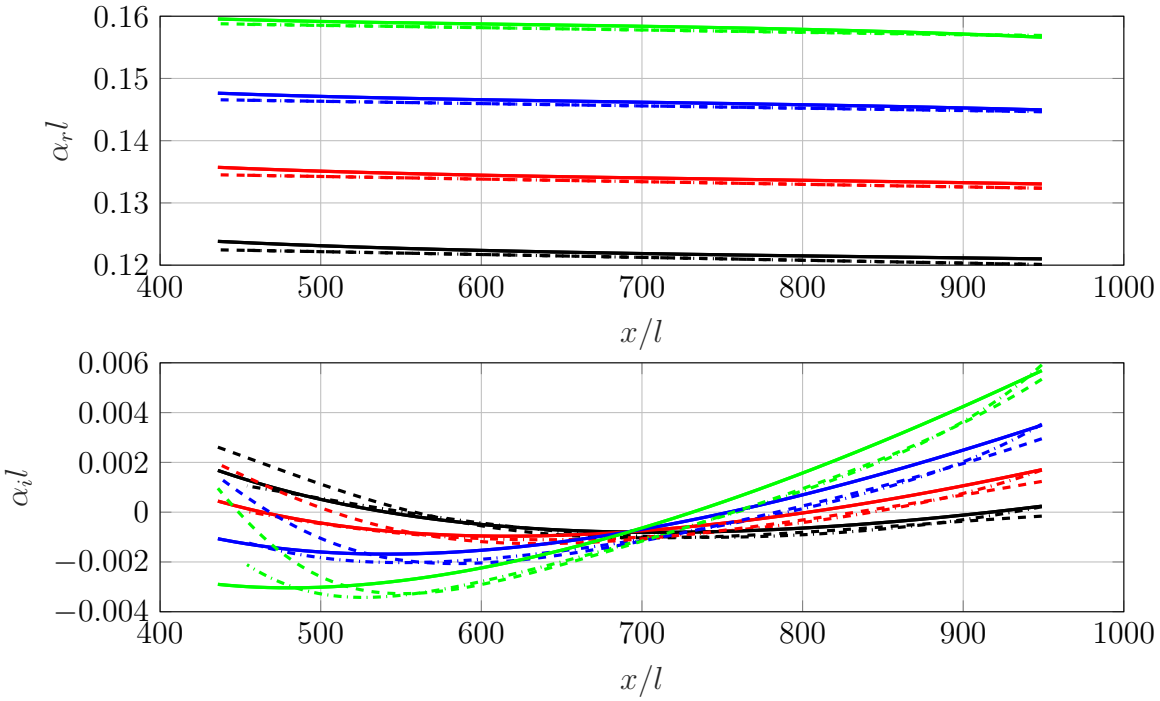

Figure 4.3.1: Streamwise wavenumbers $\alpha_r l$ (top) and growth rates $\alpha_i l$ (bottom) of four TS modes: $\omega l/\overline{U}_e = 0.04369 + 0.000998i$ (black), $\omega l/\overline{U}_e = 0.04884 + 0.000923i$ (red), $\omega l/\overline{U}_e = 0.05405 + 0.000576i$ (blue), $\omega l/\overline{U}_e = 0.05929 - 0.0000779i$ (green). Full domain LST (continuous), truncated domain BiGlobal (dash dotted line) and full domain BiGlobal (dashed line).

Fig. 4.3.3 where the boundary conditions clearly affect the regions before $x/l < 550$. In addition, due to the slight oscillations of $|\tilde{u}|$ in the streamwise direction, a polynomial interpolation is used to smooth the signal as shown by the red curves in Fig. 4.3.2 and Fig. 4.3.3 for two of the TS modes. The interpolation allows performing the derivation described by Eq. (4.3.4) effectively, allowing the computation of the growth rate $\alpha_i l$.

Even if the smoothing method applied on $|\tilde{u}|$ seems to give adequate results, it is dependent on the domain truncation which could be discussable. In this case, the domain has been truncated such that the increase of $|\tilde{u}|$ at the inlet of the domain is removed from the interpolation (i.e. $x/l \approx 455$). It is shown in Fig. 4.3.1 that the results are in good agreement with LST when such truncation is applied. On the other hand, not all TS modes are influenced in the same way by the inlet boundary conditions as depicted in Fig. 4.3.3, where the inflow effects are quite small compared to Fig. 4.3.2. An ideal case would consist of a very long domain where the regions influenced by the boundary conditions are negligible with respect to the rest of the domain that can be resolved accurately with the bi-quadratic mapping.

The spatial growth rate $\alpha_i l$ can also be evaluated with the e^N-method. The approach is generally dedicated to engineering applications, where the location of the transition from laminar to turbulent boundary layer is required. It consists of evaluating the

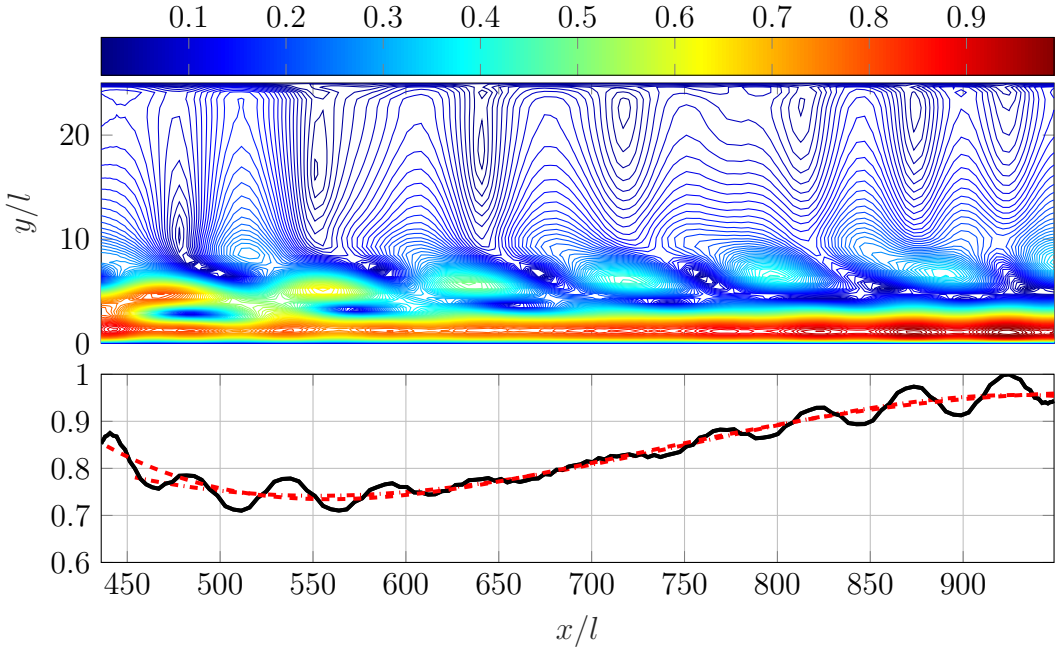

Figure 4.3.2: Two-dimensional perturbation $|\tilde{u}|/|\tilde{u}|_{max}$ of TS mode $\omega l/\overline{U}_e = 0.04369 + 0.000998i$ (top). One-dimensional perturbation $|\tilde{u}_{y_{\tilde{u}_{max}}}|/|\tilde{u}_{y_{\tilde{u}_{max}}}|_{max}$ (bottom) without smoothing (black), with smoothing over the full domain length (dashed line) and truncated domain (dash dotted line).

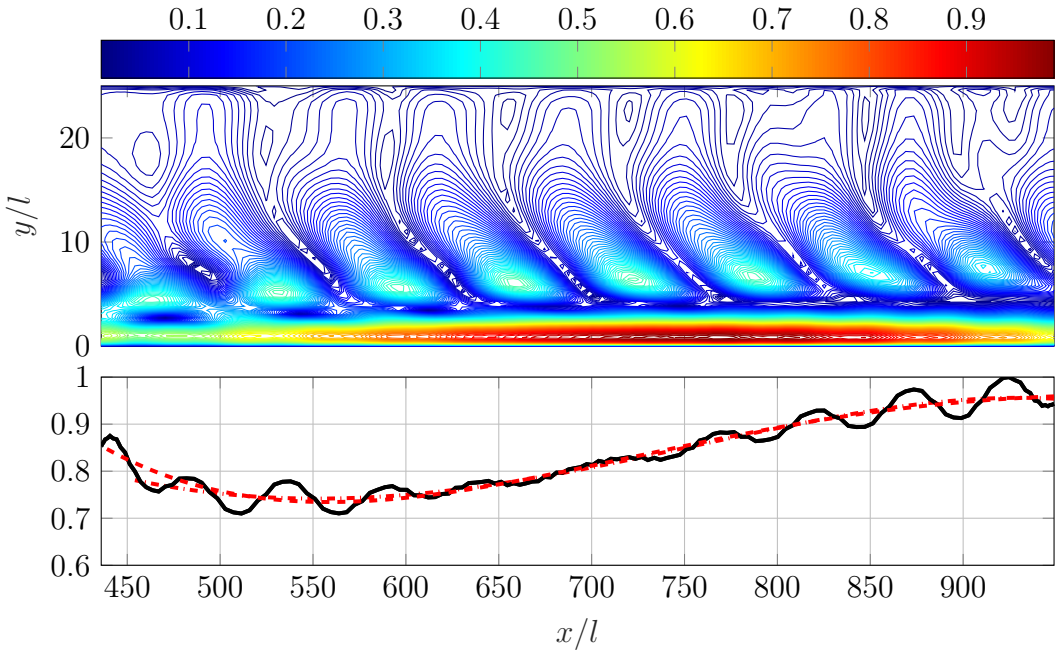

Figure 4.3.3: Two-dimensional perturbation $|\tilde{u}|/|\tilde{u}|_{max}$ of TS mode $\omega l/\overline{U}_e = 0.05929 - 0.0000779i$ (top). One-dimensional perturbation $|\tilde{u}_{y_{\tilde{u}_{max}}}|/|\tilde{u}_{y_{\tilde{u}_{max}}}|_{max}$ (bottom) without smoothing (black), with smoothing over the full domain length (dashed line) and truncated domain (dash dotted line).

cumulative growth in the streamwise direction as follows:

$$e^{N(x)} = e^{-\int_{x_0}^{x} \alpha_i(\hat{x}, y_{\tilde{q}max})d\hat{x}}, \tag{4.3.5}$$

where x_0 is the location where the perturbations become unstable. With the spatial LST, the N-factor is directly obtained by integrating the growth rate $-\alpha_i$ at each streamwise location for the wall-normal station where $|\tilde{q}|$ reaches the maximum. From the BiGlobal mode, according to Groot [2013], $N(x)$ is simply evaluated with:

$$N(x) = \int_{x_0}^{x} \frac{1}{|\tilde{q}(\hat{x}, y_{\tilde{q}max})|} \frac{\partial \tilde{q}(\hat{x}, y_{\tilde{q}max})}{\partial \hat{x}} d\hat{x} = \ln \left| \frac{\tilde{q}(x, y_{\tilde{q}max})}{\tilde{q}(x_0, y_{\tilde{q}max})} \right|, \tag{4.3.6}$$

and, therefore, $e^{N(x)}$ is simply expressed as the absolute value of a perturbation variable $\tilde{q}$:

$$e^{N(x)} = \left| \frac{\tilde{q}(x, y_{\tilde{q}max})}{\tilde{q}(x_0, y_{\tilde{q}max})} \right|. \tag{4.3.7}$$

For flow around airfoils with low freestream turbulences, the transition occurs at the location where e^N is between 9 and 13.

In Fig. 4.3.4, a comparison of the e^N values obtained with LST and BiGlobal is shown for the ten most unstable modes. The advantage of evaluating the growth rate in this alternative form is the avoidance of polynomial interpolation of the BiGlobal results, minimising the error. On the other hand, the LST integration consists of a simple cumulative summation, weighted by the x-spacing, in the streamwise direction. For both BiGlobal and LST approaches, the source of error is then significantly reduced compared to the computation of $\alpha_i l$ previously shown in Fig. 4.3.1. For both cases, $x_0 = 0$ is chosen to compute e^N over the entire domain, although the neutral curve does not lie at the inlet of the domain. The growth is defined up to a multiplicative constant, which can be assessed such that the maximum amplitude of the BiGlobal modes match with the maximum e^N predicted by the LST.

The comparison of LST and BiGlobal in Fig. 4.3.4 shows that the shape and the amplitude of the overall e^N curves are in perfect agreement. Nevertheless, a discrepancy is found regarding the streamwise locations. It is caused by the boundary conditions influencing strongly the most upstream locations of the two-dimensional modes. A shift of $x/l = +20$ is applied to all LST curves in order to correct this impact of the inflow. According to Lesshafft [2017], the influence of the boundary is characterised by the edge velocity $\overline{U}_e$, the viscosity $\overline{\mu}_e$ as well as the pressure. The latter causes a global pressure feedback following a reflection of the pressure waves on the outflow boundary. It finally impacts the inflow such that an equilibrium is reached. However, it remains quite difficult to quantify analytically the exact length influenced by the inlet boundary. In any case, the reader is referred to the article of Lesshafft [2017] for more theoretical approaches about the effect of finite domains on stability results.

In contrast, the phase required for the evaluation of $\alpha_r l$ is not interpolated and the truncation of the domain does not have an influence on these values. Actually, it reveals that the phase is not especially affected by the inflow boundary conditions. As depicted in Fig. 4.3.1, the $\alpha_r l$ computed from the BiGlobal modes are in a very good agreement

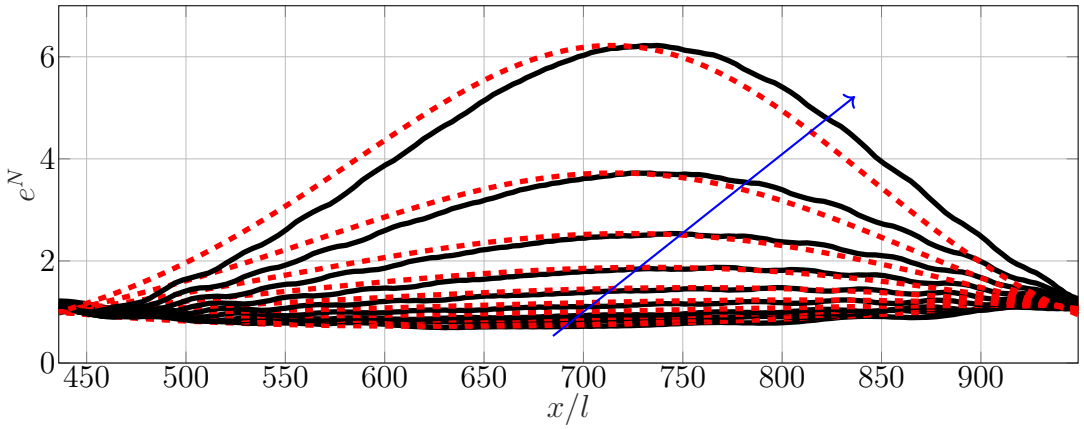

(a) No streamwise shift.

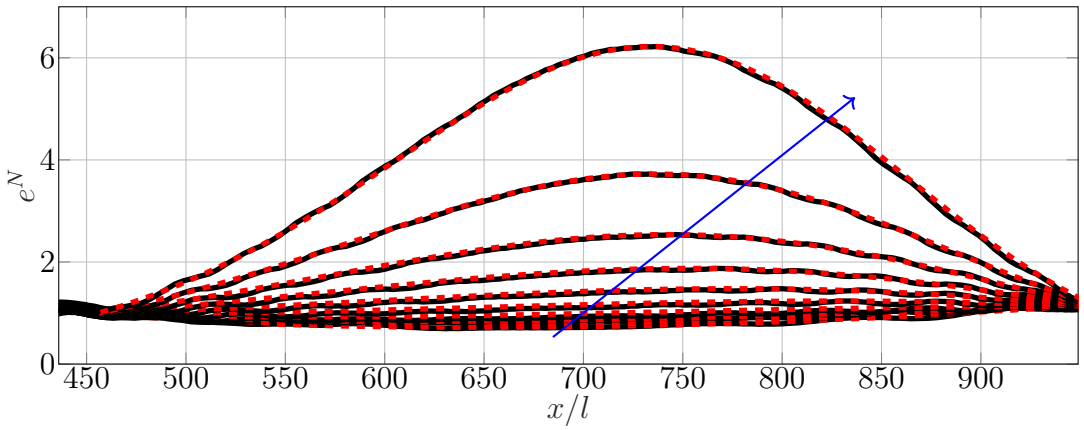

(b) Streamwise shift $x/l = +20$ of LST curves.

Figure 4.3.4: e^N for the ten most unstable TS modes evaluated with the two-dimensional BiGlobal $\tilde{u}$ field (black) and with the sequential spatial LST (red). Blue arrows indicate increasing $\omega_r l/\overline{U}_e$ from 0.0289 to 0.0748 following the branch.

with the values assessed by the LST. Considering the several $\alpha_r l$ related to the TS branch, the mean group speed reads:

$$c_{gr} = \frac{\partial \omega_r}{\partial \alpha_r} = 0.4086. \tag{4.3.8}$$

It is important to emphasize that the derivative of ω_r with respect to α_r along a branch is not perfectly constant. It is observed that c_{gr} tends to increase while the TS modes become more unstable. Consequently, a maximum group speed of about 0.4290 is found for the most unstable TS mode. For this reason, only a mean group speed is evaluated in Eq. (4.3.8) and it indicates the advection speed of a unique wave packet related to the TS mode. To have an actual representation of this convective mode as a wave packet, the Fourier transform is used as follows:

$$q' = \sum_{k=1}^{k=m} a_k \tilde{q}_k e^{-i\omega_k t}, \tag{4.3.9}$$

where m is a certain amount of eigenmodes lying on the branch, ω_k is the complex frequency of one mode k and $\tilde{q}_k$ is the related two dimensional eigenfunction. The

coefficients a_k are chosen such as the perturbation q' imposed at time $t = 0$ satisfies:

$$q' = \sum_{k=1}^{k=m} a_k \tilde{q}_k. \tag{4.3.10}$$

Despite the non-zero growth rate, the modes are assumed orthogonal to write:

$$\langle \tilde{q}_l, q' \rangle = \langle \tilde{q}_l, \sum_{k=1}^{k=m} a_k \rangle = \sum_{k=1}^{k=m} a_k \langle \tilde{q}_l, \tilde{q}_k \rangle = \sum_{k=1}^{k=m} a_k \delta_{lk} = a_l. \tag{4.3.11}$$

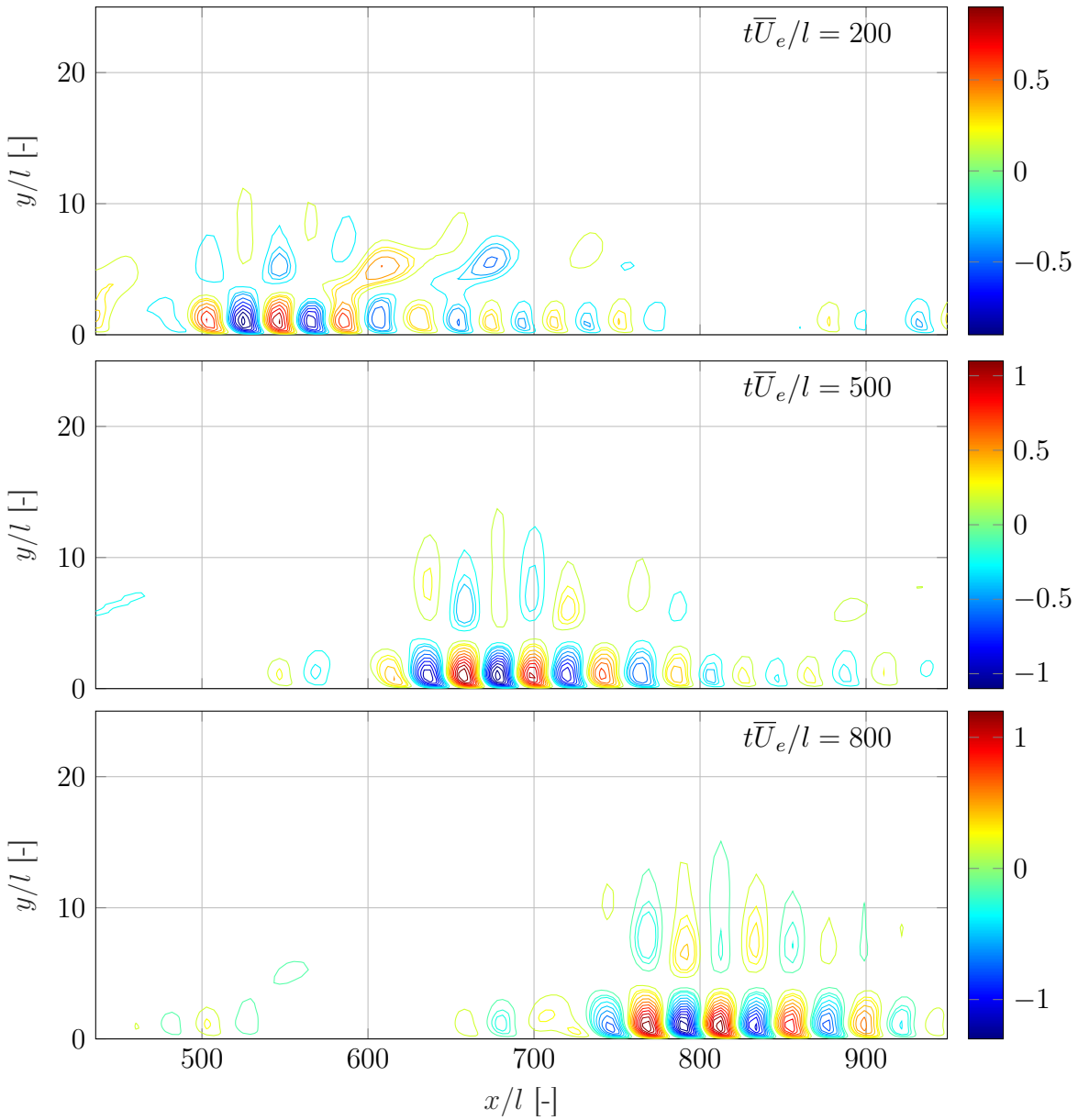

Figure 4.3.5: Low subsonic boundary layer ($M = 0.1$): snapshots at different times $t\overline{U}_e/l$ of the TS wave packet represented by $\Re(\tilde{u})/|\tilde{u}_{t=0}|_{max}$.

In the current case, the perturbation is a Dirac function imposed at location (x_0, y_0) within the domain. Therefore, the coefficients a_k in Eq. (4.3.9) are evaluated with:

$$\begin{aligned} a_k &= \langle \tilde{q}_k, \delta(x-x_0)\delta(y-y_0)\rangle \\ &= \int\int \tilde{q}_k^* \delta(x-x_0)\delta(y-y_0)dxdy \\ &= \tilde{q}_k^*(x_0,y_0), \end{aligned} \tag{4.3.12}$$

where $\tilde{q}_k^*(x_0,y_0)$ is simply the complex conjugate of the eigenfunction $\tilde{q}_k$ at the position specified for the impulsion. With the Fourier transform, it is therefore possible to reconstruct a wave packet related to the TS mode. Fig. 4.3.5 shows a wave packet at three different times $t\overline{U}_e/l$ travelling downstream after a Dirac impulsion imposed at $(x_0, y_0, t\overline{U}_e)/l = (485, 10, 0)$. Note that $\Re(\tilde{u})$ is normalised by $|\tilde{u}|$ at the first time step in order to visualise the physical growth of the mode. Although the actual group speed is a function of the streamwise coordinate x, the mean value $c_{gr} = 0.4086$ is already an excellent indicator of the celerity of the TS wave packet for the current low subsonic boundary layer.

Because of the existence of a branch and the TS mode cannot be represented as an absolute instability in the current reference frame. This representation is achievable if the reference frame moves at the group speed of the convective mode. Such moving frame is obtained by subtracting the mean group speed from the current base flow. In other words, it consists of eliminating the advection contribution linked to the TS modes from the stability equations. For one-dimensional problem (i.e. LST equations excluding non-parallel flow $\overline{V}$), these terms can be totally removed from the stability equations to represent all the convective modes as absolute modes. However, due to the

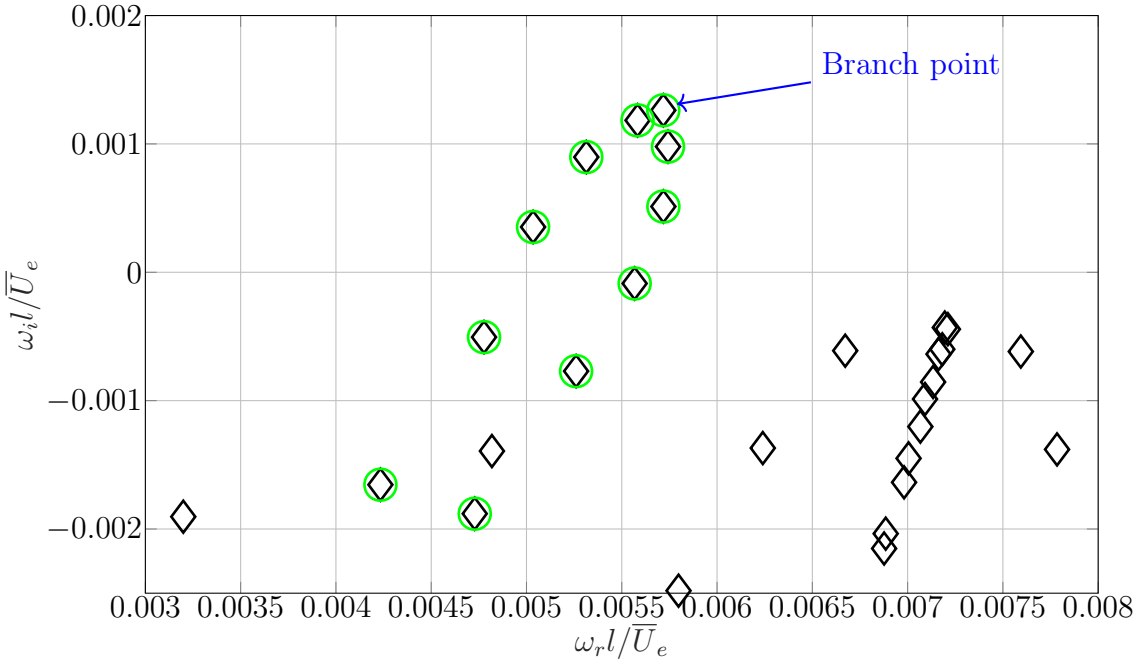

Figure 4.3.6: Low subsonic boundary layer ($M = 0.1$): Spectrum (black diamond) without the mean group speed $c_{gr} = 0.4086$ of the TS mode (highlighted by green circles).

non-separability caused by the two-dimensionality of the BiGlobal equations, it is not possible to remove the advection terms linked to all the modes. Therefore, for 2D cases, it is only possible to represent one convective mode as an absolute mode by considering a reference frame moving at the corresponding group speed. Here, the group speed of the TS branch mode is selected.

Solving the compressible BiGlobal stability equations in the reference frame moving at $c_{gr} = 0.4086$ provides the spectrum depicted in Fig. 4.3.6. It shows that the TS mode appears in the form a cusp. According to Briggs' and Bers' criteria, the presence of a cusp with a branch point at the top indicates that the mode is absolute, in this moving reference frame. The branch point is the most unstable eigenvalue of Fig. 4.3.6 and indicates the growth rate of the TS mode directly. An illustrative example is depicted in Fig. 4.3.7, where the absolute mode related to the branch point $\omega = 0.00572 + 0.001262i$ is shown. Although the inlet boundary condition has small impact on the amplitude of the modes, it clearly shows that a convective instability can be represented by an absolute mode in a moving reference frame. Note that, to have a perfect representation of the TS mode as an absolute mode, the group speed varying with respect to x should be removed from the base flow instead of a mean value. This way, it is expected that the parabola collapses into points aligned below the branch point. We will investigate such

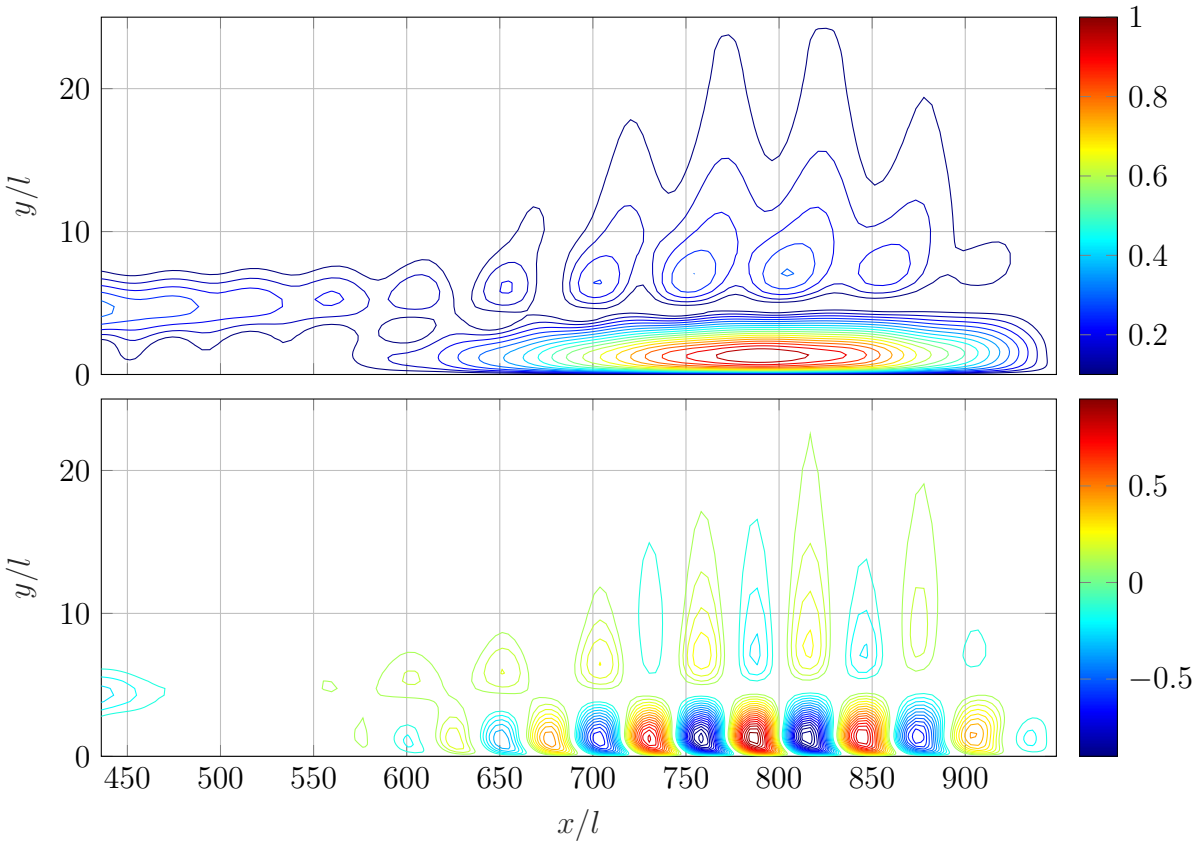

Figure 4.3.7: Low subsonic boundary layer ($M = 0.1$): TS mode represented by $|\tilde{u}|/|\tilde{u}|_{max}$ (top) and $|\Re(u)|/|\tilde{u}|_{max}$ (bottom) as an absolute mode in a reference frame moving at $c_{gr} = 0.4086$.

implementation in further researches about the streamwise stability of developing flows and, up to this point, we conclude that removing the mean speed consists in a major improvement in the representation of convective mode as absolute mode.

4.3.2 Supersonic boundary layer

For the stability of the supersonic boundary layer, the two base flows previously compared are involved to give an insight into the sensitivity of the stability equations. In Fig. 4.3.8, the spectra are shown for a static reference frame and the TS branch is highlighted in blue. In this case, the identification of the branch is challenging and a convergence analysis in the wall-normal direction has been conducted in order to localise the eigenvalues with the higher convergence rate. On one hand, the two different base flows reveal extremely similar spectra as an 10^{-6} absolute different exists for both real and imaginary parts of the modes with a higher frequency content. On the other hand, close to the imaginary axis, the difference becomes almost indistinguishable. In addition, both spectra exhibits slight interaction with other modes which are not associated to the TS ones. For instance, the eigenfunction corresponding to $\omega_r l/\overline{U}_e \approx 0.0188$ has spurious oscillations superimposed on the TS mode.

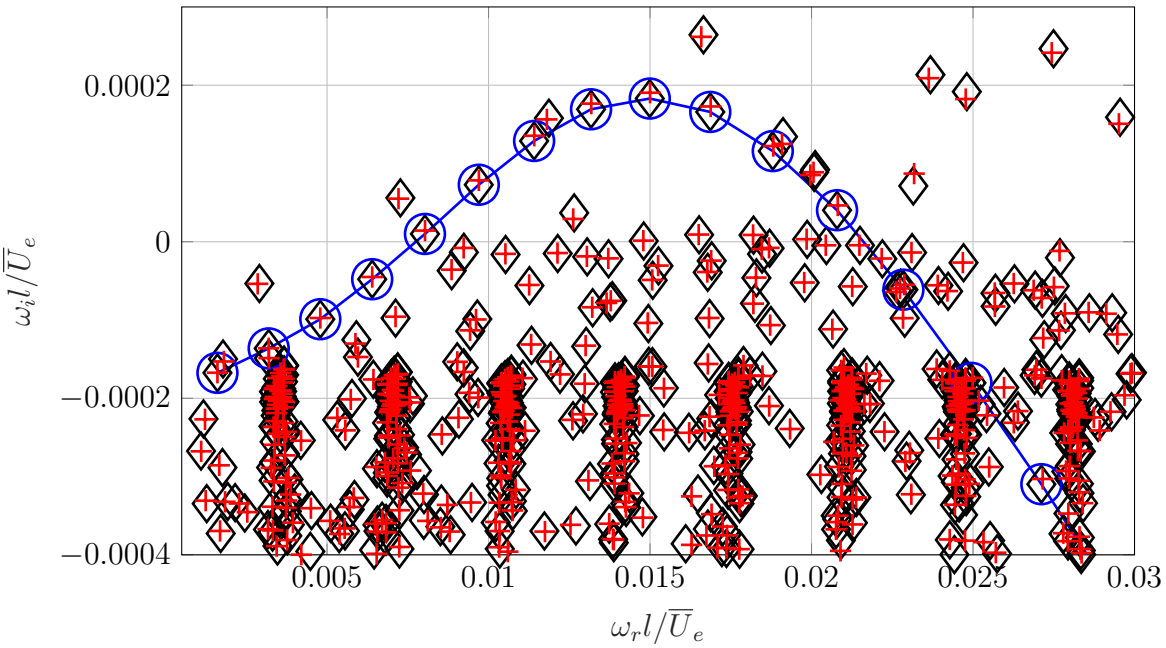

Figure 4.3.8: Supersonic boundary layer($M = 1.7$): spectra for base flows evaluated with CBL solver (red cross) and with DNS solver (black diamond). The TS modes are indicated in blue.

Unfortunately, the complexity of the supersonic TS modes does not give the opportunity to represent the spatial growth rate of each mode lying on the TS branch. The methods used previously for the low subsonic case are not able to provide accurate results due to the strong oscillations of the absolute value $|\tilde{u}|$ or $|\tilde{v}|$. In Fig. 4.3.9, a two-dimensional representation of a TS mode is shown beside the corresponding one-dimensional streamwise variation of $|\tilde{u}_(x, y_{\tilde{u}_{max}})|$. Compared to the incompressible case,

it exhibits strong oscillations in the streamwise direction and a significant influence of the inlet boundary. Even though the smoothing seems effective in Fig. 4.3.9, strong discrepancies are found for $\alpha_i l$ when compared to the LST results due to the polynomial interpolation and the domain truncation sensitivity.

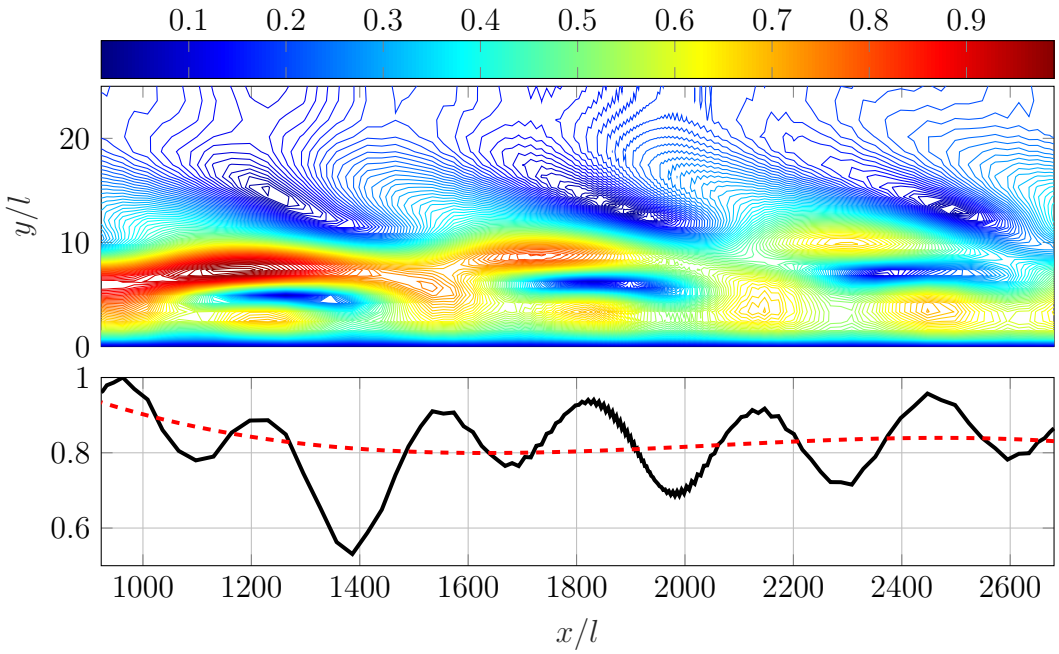

Figure 4.3.9: Two-dimensional perturbation $|\tilde{u}|/|\tilde{u}|_{max}$ of TS mode $\omega l/\overline{U}_e = 0.0097008 + 0.0000784i$ (top). One-dimensional perturbation $|\tilde{u}_{y_{\tilde{u}max}}|/|\tilde{u}_{y_{\tilde{u}max}}|_{max}$ (bottom) without smoothing (black) and with smoothing (red dashed line).

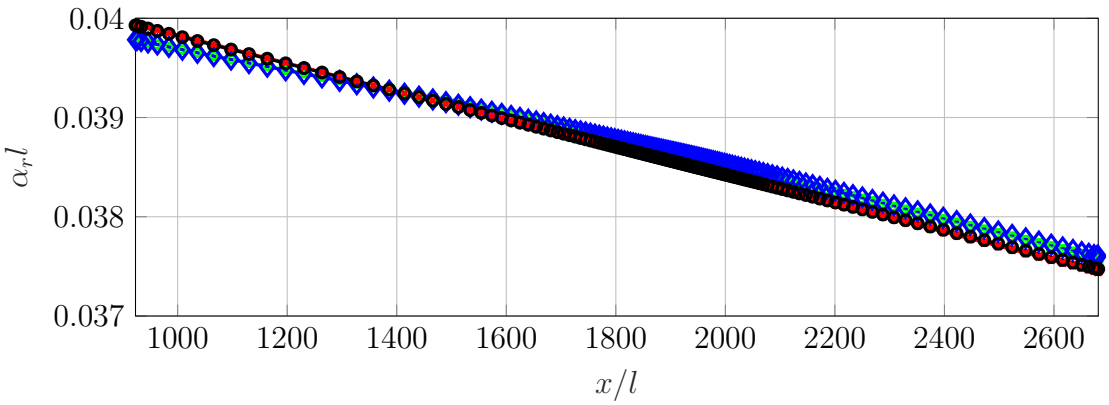

Figure 4.3.10: Streamwise wavenumber $\alpha_r l$ of one TS mode ($\omega l/\overline{U}_e = 0.018818177 + 0.00012228i$ evaluated with CBL-CLST (green square), CBL-BiG (red cross), DNS-CLST (blue diamond) and DNS-BiG (black circle).

Nevertheless, the spatial wavenumbers $\alpha_r l$ can be evaluated in the same way as previously done for the incompressible boundary layer. For sake of clarity, only one wavenumber varying with x is shown in Fig. 4.3.10. Comparing the LST and the BiGlobal results,

it reveals very similar values, up to a 10^{-4} accuracy, for both base flows. In addition, the absolute difference between the wavenumbers computed by the LST-CBL and the LST-DNS is only about 10^{-10} while 10^{-8} is observed between the BiG-CBL and BiG-DNS wavenumbers. Finally, the group speed can be computed using each $\alpha_r l$ with the related ω as shown in Tab. 4.3.1, revealing a 10^{-4} error depending on the case handled.

	BiGlobal	CLST
CBL base flow	0.5245	0.5218
DNS base flow	0.5238	0.5214

Table 4.3.1: Group speed based on the BiGlobal and LST computation using the CBL or the DNS solver for the base flow.

The group speed $c_{gr} = 0.5238$ corresponds to the propagation speed of the TS mode wave packet, shown in Fig. 4.3.11. The packet is constructed exactly in the same way as the low subsonic boundary layer and uses all the modes lying on the branch shown in the spectrum (Fig. 4.3.8). As the TS mode is more complex for supersonic boundary layers than the incompressible equivalent, the travelling wave packet shows several differences compared to the previous case. The inflow is more prone to influence each independent

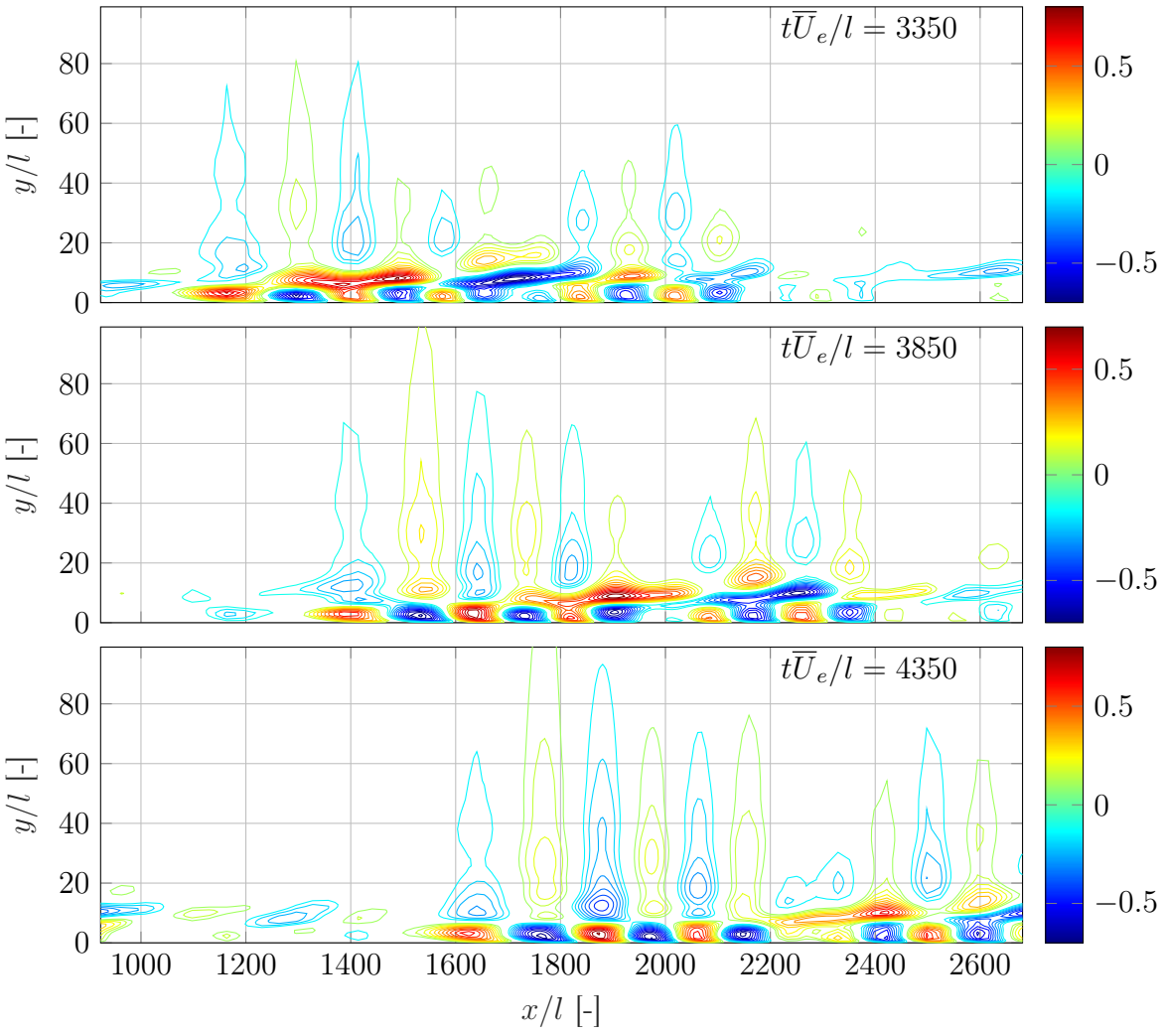

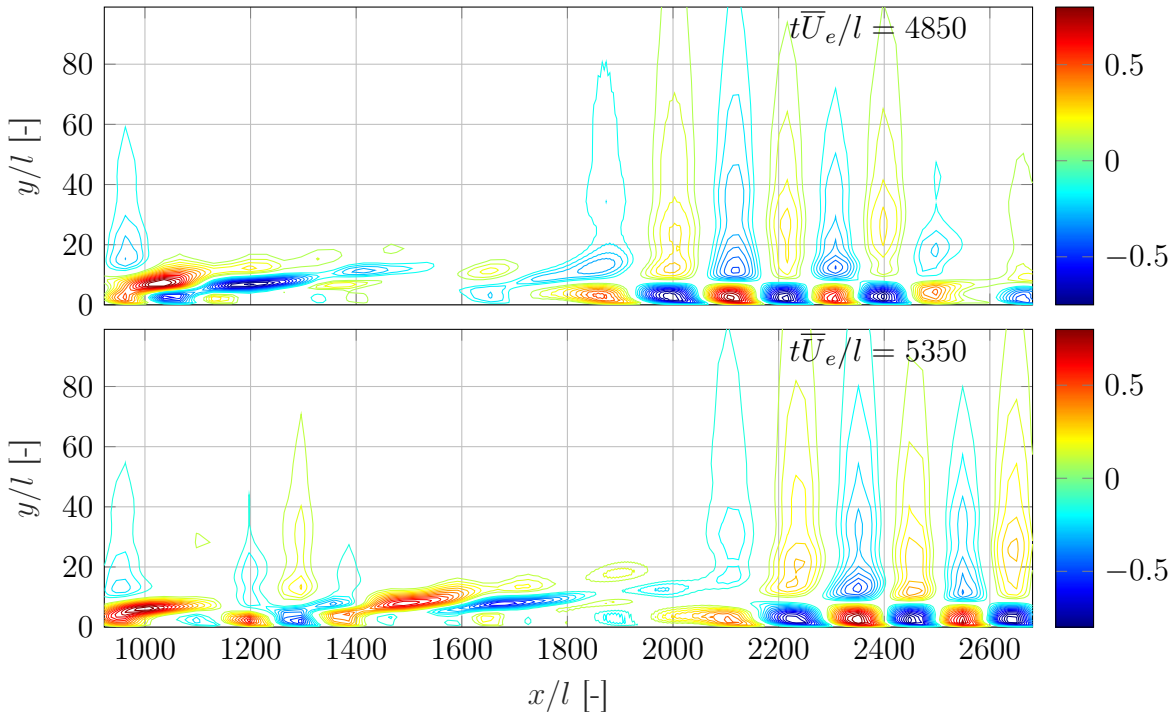

Figure 4.3.11: Supersonic boundary layer($M = 1.7$, DNS): Snapshots at different times $t\overline{U}_e/l$ of the TS wave packet represented by $\Re(\tilde{u})/|\tilde{u}_{t=0}|_{max}$.

mode present on the TS branch. It impacts therefore the overall wave packet as depicted by the first snapshot of Fig. 4.3.11, where the mode is difficult to distinguish. When moving downstream, three regions where the maximal magnitude in the vertical direction are identifiable while the low subsonic boundary reveals only two of them. For the latter, a region close to the wall ($y/l \in [0, \delta_{99}]$ with $\delta_{99} \approx 5$) contains the maximum values of the modes and a second region consists of the characteristic decay of the TS mode in the freestream. Both zones are advected at the same group speed with the whole wave packet. Regarding the compressible boundary layer, an intermediate region, exhibiting a different advection speed than the rest of the wave packet, seems to be generated at the inflow boundary. Moreover, when approaching the inlet or outlet boundaries, the propagation speed of the intermediate part decreases.

On the other hand, it is important to notice that, physically, once the perturbation is applied (Dirac function here), the wave packet is generated and convected downstream with a certain group speed. Therefore, after a time $t \approx c_{gr}L$ with L the domain length, the entire wave packet should have left the computational domain. In the current reconstruction of the TS mode as a convective mode through the Fourier transform, there is a strong assumption about the temporal periodicity of the wave. In the two last snapshots of Fig. 4.3.11, this periodicity is clearly visible as the wave packet travels across the outflow boundary and continues at the inlet of the domain. Such phenomenon is enforced as well by the Neumann condition at the inlet/outlet which imposes the spatial periodicity of all the perturbation waves. Considering that the length of the current domain is about $L/l = 1757$ and the group speed is $c_{gr} = 0.5245$, the period of the wave packet is about $T\overline{U}_e/l = 3350$. Nevertheless, this periodicity is purely due to the problem set-up and the Fourier reconstruction of the wave packet; it does not represent

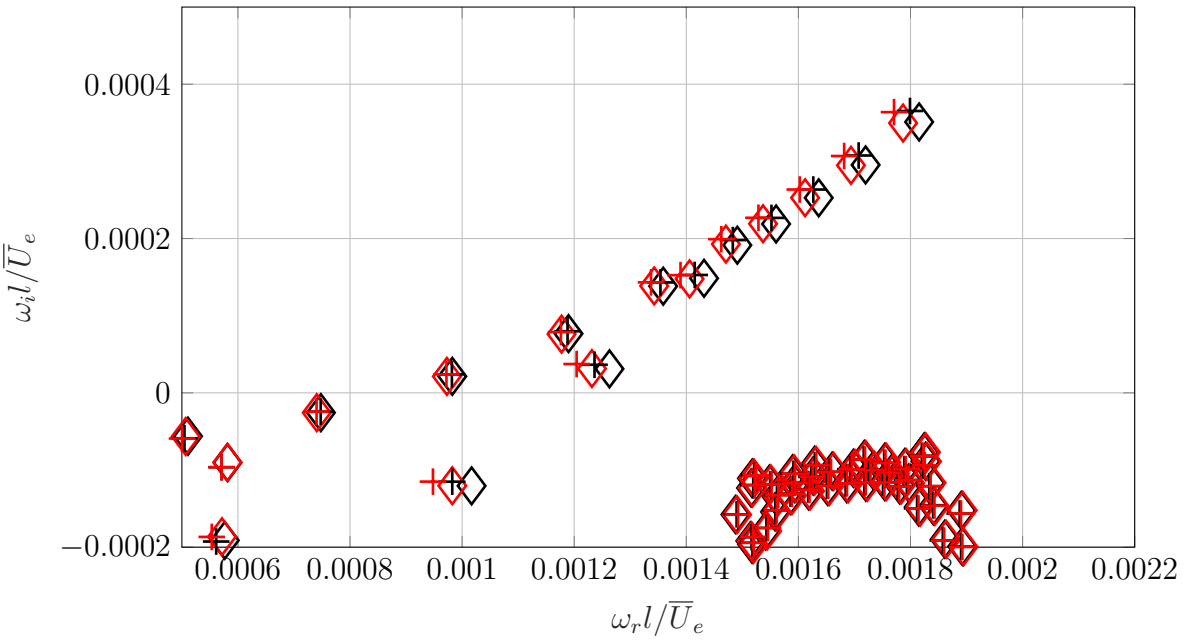

Figure 4.3.12: Supersonic boundary layer($M = 1.7$): spectra with TS group speed from CBL (black, $c_{gr} = 0.5245$) or DNS (red, $c_{gr} = 0.5238$) removed from the base flows evaluated with CBL solver (cross) and with DNS solver (diamond).

any physical process in the case of a simple impulsion at $t = 0$. In other words, except the first period where the wave packet travels across the domain for the first time, the other periods are not physically induced by the impulsion. Nevertheless, in Fig. 4.3.11, the second period is shown instead of the first one for sake clarity. In point of fact, as the amplitude is continuously growing in time, it gives the opportunity to represent the wave packet in a better way by avoiding the low contour level inducing noise in the visualisation.

The representation of the TS mode as an absolute mode instead of a convective one is carried out by removing the advection speed from the streamwise velocity component of the base flow. As shown in Tab. 4.3.1, several group speeds have been computed depending on the method used to evaluate the base flow. Nevertheless, only the BiGlobal group speeds are considered to be subtracted from the two base flows. The resulting spectra are shown in Fig. 4.3.12, where the crosses represent the BiGlobal solutions with the base flow from the CBL solver, while the diamonds indicate the base flow evaluated with the DNS solver. Removing the TS group speed clearly gives similar results as the incompressible case; the TS mode is represented by a cusp with a unique branch point. Although the group speed impacts slightly the frequency of the branch point, it does not influence the temporal growth rates. Fig. 4.3.12 shows that the branch point is closer to the imaginary axis when a smaller group speed is removed. In contrast, as already mentioned with the static reference frame, both frequency and growth rate shows a dependency with respect to the base flow solutions.

Fig. 4.3.13 shows the isolated eigenfunction corresponding to the red diamond branch point of Fig. 4.3.12. In contrast to the subsonic case, where the mode is confined in the interior of the domain, the TS wave of the compressible boundary layer has its location

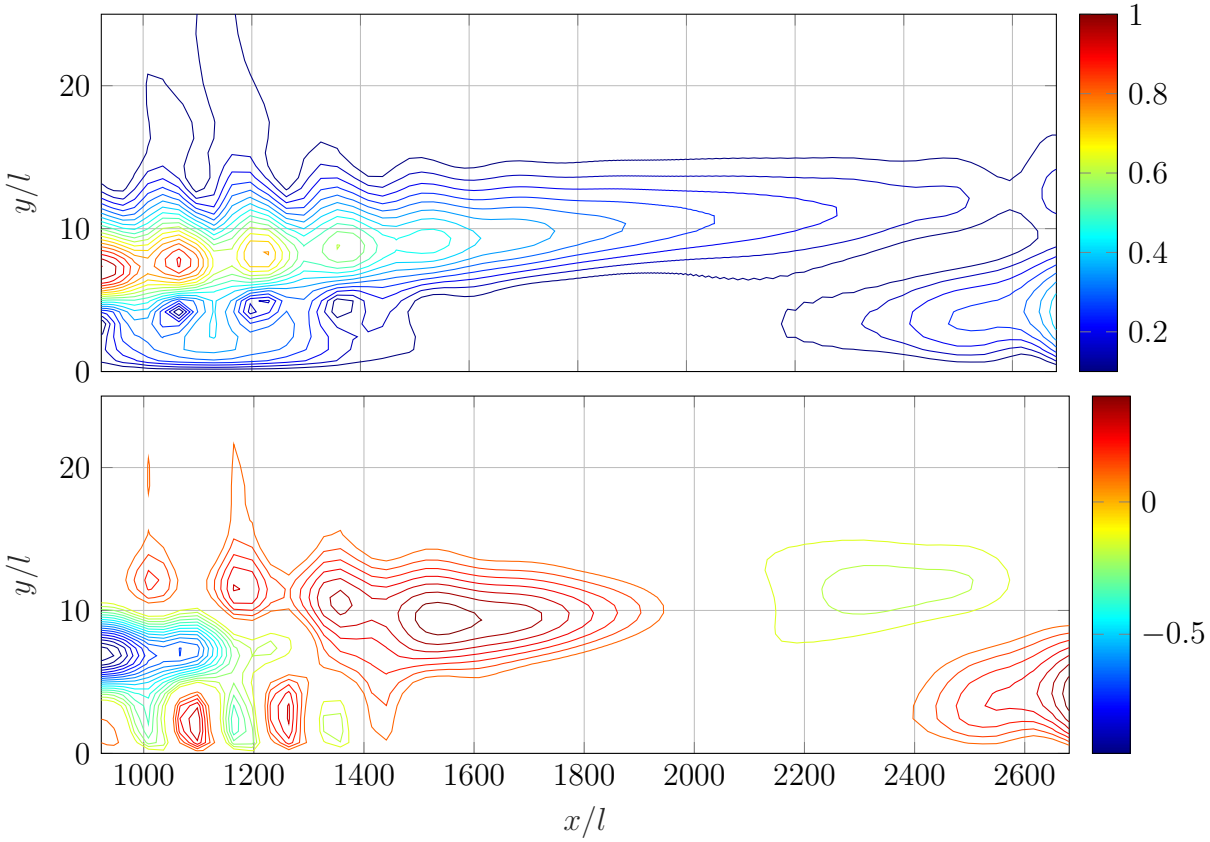

Figure 4.3.13: Supersonic boundary layer ($M = 1.7$, DNS): TS mode represented by $|\tilde{u}|/|\tilde{u}|_{max}$ (top) and $|\Re(u)|/|\tilde{u}|_{max}$ (bottom) as an absolute mode in a reference frame moving at $c_{gr} = 0.5238$.

of maximum amplitude at the inflow boundary, yielding a strong influence of the inlet. Therefore, removing the group speed from the base flow shows that the domain has to be extended upstream in order to ensure the TS mode reaches its minimum amplitude at the boundaries.

Finally, we conclude that removing the group speed from the base flow is undoubtedly effective to perceive the TS mode as an absolute mode for both compressible and incompressible cases. Therefore, using this reference frame for the representation of convective modes is promising for future researches based on the BiGlobal stability equations.

4.4 Intermediate conclusion

This chapter handles the stability of one subsonic and one supersonic developing boundary layer. It aims to provide an insight into more complex stability problems, where the modes travel in the streamwise direction through the inflow and outflow boundaries. Analysing a developing boundary layer poses an introduction to understand the underlying physical and numerical aspects of such stability analyses before considering more complex configurations where shocks are encountered. For both subsonic and supersonic boundary layers, the base flows are computed by a compressible boundary layer (CBL) solver with an implicit marching in space. An additional supersonic case is computed

with a Direct Numerical Simulations (DNS) solver, aiming to analyse the impact of the base flow solution on the stability results. The two methods reveal a good agreement in the velocity and temperature profiles such that only relative errors of $\mathcal{O}(10^{-4})$ are found in the shear layer.

Parameter studies are carried out on the numerical set-ups for the BiGlobal analyses. Different boundary conditions are examined for the freestream boundary in order to ensure the best representation of the decay of Tollmien-Schlichting (TS) waves in the freestream. It reveals that imposing the no-slip and isothermal condition is more appropriate than the Neumann condition on all the variables as it shows less dependency with respect to the domain height. Nevertheless, with the former boundary condition, an additional closure for the pressure term is needed. As the pressure compatibility condition reveals the presence of spurious modes in the unstable half-plane of the spectrum, the linearised Poisson pressure equation adapted from Theofilis [2017] to a compressible BiGlobal framework is employed. It exhibits excellent results compared to the compatibility condition and the spurious modes are effectively removed. Finally, a convergence analysis in both directions is conducted for the incompressible case. It shows that the streamwise direction is under-resolved, while the wall-normal direction is converged, but only small discrepancies are encountered as consequence. Nevertheless, the nowadays computational memory does not give the opportunity to increase the number of collocation nodes in the streamwise direction.

Physical aspects of the TS mode of the subsonic and supersonic boundary layer are handled next. The spatial wavenumbers and growth rates in the streamwise direction are extracted from the two-dimensional mode. For comparison purpose, one-dimensional stability analyses (LST) are carried out at several streamwise location. Although such approach does not take into account the stabilising parallel effects, good agreements for the streamwise growth rates and wavenumbers between the LST and BiGlobal results for the subsonic case are found. In addition, in order to predict the transition with a more practical approach, the N-factor is computed. By applying a streamwise shift to neglect the inflow boundary effects of the BiGlobal modes, very similar results are found between the LST and BiGlobal approaches. On the other hand, the computation of the spatial growth rate for the compressible boundary layer is subjected to the stronger influences of the inlet boundary and to the more complex eigenfunction related to the TS mode. Nevertheless, the evaluation of the streamwise wavenumbers exhibits very similar results between LST and BiGlobal approaches. Finally, a comparison between the supersonic base flow computed with the DNS and the CBL solver reveals relative differences of $\mathcal{O}(10^{-5})$ for the temporal eigenvalues lying on the TS branch.

Finally, as the TS mode is a convective instability, the related wave packet is constructed for both subsonic and supersonic boundary layers. The wave packet is generated by a Dirac impulsion at the inlet of the domain and, based on an assumed orthogonality of the modes present in the branch, the Fourier transform is used to build the entire mode. It travels downstream at group speeds $c_{gr} = 0.4086$ and $c_{gr} \approx 0.52$ for the $M = 0.1$ and $M = 1.7$ cases, respectively. Due to the convective behaviour of the TS wave, the representation in the BiGlobal spectrum as a branch exhibits low convergence rate in the streamwise direction. In contrast, the discrete modes reveal very high convergence rate in general and it consists of an ideal representation of a mode. In order to achieve such representation, the group speed of the TS wave is removed from the base flow of

both boundary layer cases. It implies that the convective mode cannot be advected and the original branch collapses into a cusp with a branch point. It yields a TS mode represented by an isolated eigenfunction whose the growth rate (of the wave packet) is described by the branch point. This simple manipulation of the base flow consists of a major improvement about the convective modes for further work with BiGlobal analyses as the convergence rate in the streamwise direction must be significantly increased.

5. Shock-Wave/Boundary-Layer Interactions

Numerical investigations of the laminar Shock-Wave/Boundary-Layer Interactions (SWBLI) are conducted with DNS and BiGlobal stability analyses. The first section focuses on the numerical set-ups beside a discussion about the ability of spatial discretisation schemes to converge a steady-state solution with shocks. The second section considers three different shock angles impinging on a boundary layer developing over a flat plate and are compared with the original experiments conducted by Giepman [2016] in the TST-27 blowdown transonic/ supersonic wind tunnel of Delft University of Technology. In addition, the results are verified and correlated with several similarity laws based on free interaction theory. Finally, the last section handles the BiGlobal stability of the separation bubble, where a Kelvin-Helmholtz instability and a common characteristic of a steady mode are identified.

5.1 Numerical set-up of the base flow

The laminar SWBLI case has exactly the same numerical set-up as for the supersonic developing boundary layer. The only difference is the introduction of a shock-wave at the top boundary of the domain. The impinging location on the wall is at 51mm from the leading edge of the flat plate, according to the experiments of Giepman [2016]. For the present case, three shock angles are chosen for the analysis of different bubble sizes, providing the opportunity to verify the similarity laws from free interaction theory. Tab. 5.1.1 shows several physical parameters of the SWBLIs, where θ_d is the deflection angle of the wedge to induce the oblique shock and θ_w is the related wave angle evaluated with the Rankine-Hugoniot relation. $p_e = 1/(\gamma M^2)$ is the freestream pressure before the incoming shock, p_2 and p_3 are respectively the pressures behind the incoming shock and behind the entire shocks system. The Blasius length l of the boundary layer imposed at the inlet of the BiGlobal domain $(x, y)/l \in [923, 2681] \times [0, 200]$ is used as reference length (see Tab. 4.1.1 in chapter 4). The dimensions of the DNS grid are $(x, y)/l \in [758.4, 3121.4] \times [0, 1000]$ with $(N_x \times N_y) = (1000 \times 500)$ points uniformly distributed in the x-direction and with a hyperbolic stretching in the y-direction such that $y^+ = 1$ for the first cells above the wall. At this boundary, the no-slip and the adiabatic boundary closures are applied, while Riemann invariant conditions are imposed for the other boundaries to avoid shock reflections. A compressible equivalent of the Blasius boundary layer profile is imposed along the wall as initial condition.

M	θ_d	θ_w	p_e/p_2	p_e/p_3	l[m]	δ_{imp}/l	δ^*_{imp}/l	Re_l	$Re_{x,imp}$
1.7	1°	36.96°	1.05	1.15	2.6372×10^{-5}	8.74	4.1	923	1.8×10^6
1.7	2°	37.93°	1.11	1.22	2.6372×10^{-5}	8.74	4.1	923	1.8×10^6
1.7	3°	38.92°	1.16	1.35	2.6372×10^{-5}	8.74	4.1	923	1.8×10^6

Table 5.1.1: Numerical set-ups for the DNS simulations of the shock-wave/boundary-layer interactions.

The viscous fluxes are computed with a second order central scheme while the third order accuracy Harten-Lax-van Leer-Contact (HLLC) solver is used for the convective fluxes (discussed in the next section). The viscosity and the thermal conductivity are computed with the non-dimensional Sutherland law:

$$\overline{\mu} = \frac{1}{Re_l}\left(\frac{\overline{T}}{\overline{T}_e}\right)^{3/2} \frac{1+\frac{S}{\overline{T}_e}}{\frac{\overline{T}}{\overline{T}_e}+\frac{S}{\overline{T}_e}}, \qquad \overline{k} = \frac{1}{(\gamma-1)M^2 Pr}\overline{\mu}, \tag{5.1.1}$$

where $S = 110.4K$ (effective temperature) and $Pr = 0.72$ the Prandtl number. Finally, it yields a perfect consistency with the supersonic developing boundary layer previously analysed.

In addition, due to a potential transition from laminar to turbulent flow in the post-shock region of the bubble, the Selective Frequency Damping (SFD) method, developed by Åkervik et al. [2006], is used to enforce a steady state solution of the NSE. In the present DNS solver, the encapsulated formulation (Jordi et al. [2014]) of the SFD method (ESFD) is considered. In addition to the avoidance of any modification in the core of the solver, ESFD reveals better performances, since Jones and Sandberg [2011] succeeded to convergence numerical experiments, while conventional SFD failed.

5.1.1 Convective flux reconstruction schemes

The convergence to steady-state solutions, when shocks are encountered, has always been challenging during the last decades and is still the centre of interest of many researchers focusing on discretisation schemes for such problems. Basically, the residual of the governing equations is required to converge fast to machine precision, while a high accuracy near the shock region is desired. The former objective can be easily obtained by using limiter across the shock, leading to a first-order solution in the shock region (shock smearing) and a higher accuracy elsewhere. Consequently, the post-shock oscillations are avoided and the steady solution can be obtained at machine precision. On the other hand, if a high-order method is used to evaluate the shock regions, strong post-shock oscillations or overshoots tend to appear, yielding difficulties for reaching a low residual level. Nowadays, the Weighted Essentially Non-Oscillatory (WENO) schemes, originally presented by Liu et al. [1994], for the reconstruction of the convective fluxes are a good compromise between shock resolving and high-order accuracy. In the current thesis, a third-order accuracy WENO scheme is considered for two reasons.

The first reason is the ability to reach machine precision for steady-state solution with a third-order WENO scheme, while it is challenging with a fifth-order method. The latter does introduce slight post-shock oscillations, causing the residual level high above machine precision. Different investigations have been conducted by Zhang and

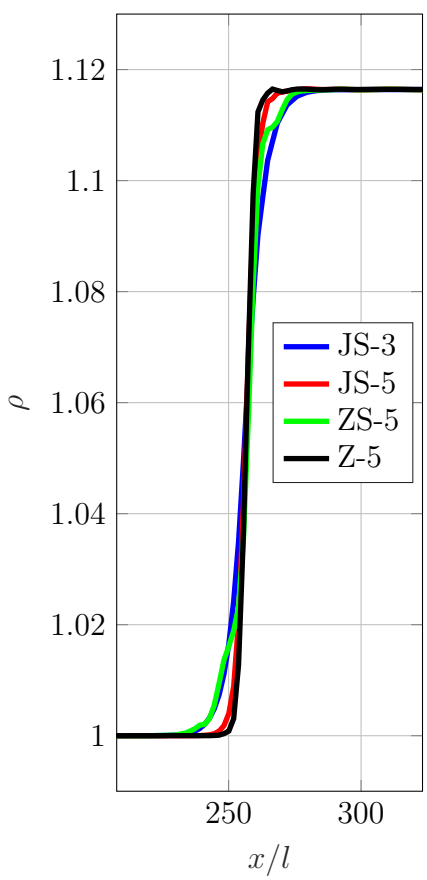

(a) Incident oblique shock-wave.

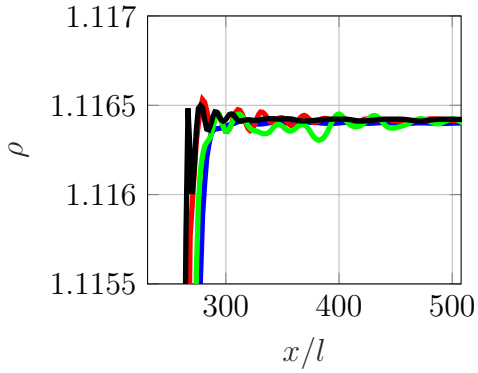

(b) Zoom on the post-shock zone.

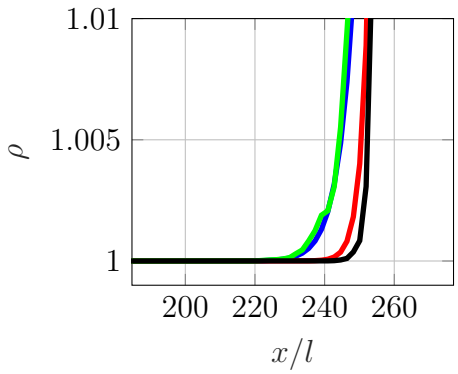

(c) Zoom on the ante-shock zone.

Figure 5.1.1: Density ρ [-] jump across the incident shock-wave at $\theta_d = 3°$ ($p_e/p_3 = 1.35$) with respect to the streamwise direction x/l considering different flux reconstruction WENO schemes.

Shu [2006]; Borges et al. [2008]; Zhang et al. [2011] in order to improve the behaviour of the WENO5 with respect to the reachability of supersonic steady states. Nevertheless, the variants of the WENO5 schemes cannot remove entirely the post-shock oscillations as depicted in Fig. 5.1.1, where JS-WENO (3^{rd} and 5^{th}) stands for the schemes originally presented by Jiang and Shu [1996]. The ZS-WENO scheme, proposed by Zhang and Shu [2006], consists of removing the second derivatives term related to the smoothness indicators. The results showed by Zhang and Shu [2006] are promising but Zhang et al. [2011] reveal that a low residual level can only be reached if the shocks are perfectly aligned with the grid points of the discretised domain. Without alignment, as shown in Fig. 5.1.1, the shock exhibits strong oscillations along a large downstream part. Such behaviour puts the residual level at a minimum of 10^{-5}, largely above machine precision. Borges et al. [2008] introduced another formulation of the WENO5; the Z-WENO scheme. Fig. 5.1.1 clearly shows that the damping of the post-shock oscillations is more efficient than the two other fifth order schemes. Nevertheless, the Z-WENO presents a stronger overshoot in the post-shock region, as highlighted by Zhang and Shu [2006]; Zhang et al. [2011]. Despite the better performances compared to the other schemes, the residual level hangs at 10^{-6} with the Z-WENO scheme. Consequently, we conclude

that the fifth-order WENO schemes cannot ensure a steady state with a low residual level for the current SWBLIs.

The second reason of choosing the WENO3 scheme is related to the sensitivity of the stability equations to the second-order derivatives. A third-order WENO scheme introduces a slight smearing of the shocks while a fifth order induces very abrupt variations and high amplitude oscillations in these regions. Therefore, conducting the DNS with the JS-3 WENO allows reaching a very low residual level in combination with smoothened derivatives in shock region.

5.2 Analysis of the base flow

In the current section, the base flows with the three shock angles are analysed. In Fig. 5.2.1, the streamwise velocity $\overline{U}$ is shown beside the isolines $\overline{U} = 0.9\overline{U}_e$ and $\overline{U} = 0$. It reveals that the three separation bubbles are totally different. When $\theta_d = 1°$, the boundary layer is subjected to a very small adverse pressure gradient and has only a very small upward deflection ($\approx +0.75l$) at the shock impingement. Increasing the deflection angle to $\theta_d = 2°$ increases the length of the bubble. In addition, the bubble exhibits a near-symmetrical structure with respect to the impingement location $x_{imp}/l = 1934$. Nevertheless, note that the velocity field inside the recirculation region is not symmetric.

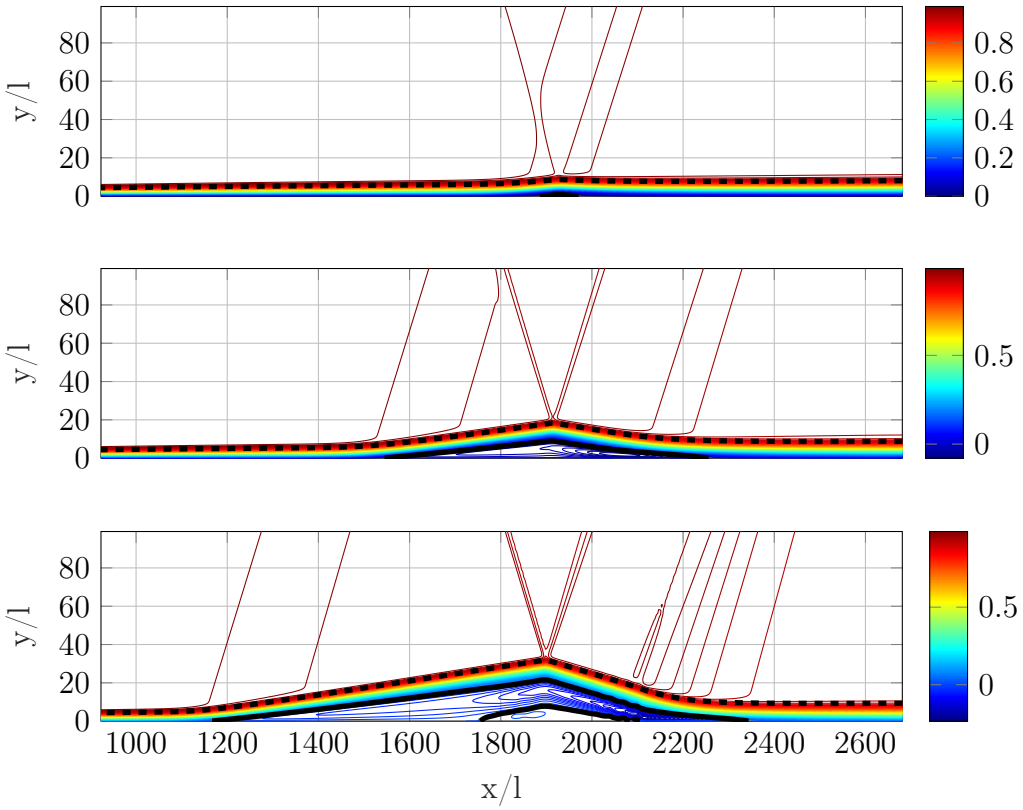

Figure 5.2.1: Streamwise velocity $\overline{U}/\overline{U}_e$ for deflection angles $\theta_d = 1°$ (top), $\theta_d = 2°$ (intermediate) and $\theta_d = 3°$ (bottom). Black dashed lines for boundary layer height $\delta_{\overline{U}=0.9\overline{U}_e}$ and black solid lines for $\overline{U} = 0$ contours.

Due to the bubble dimensions, the flow decelerates quite significantly on the bubble front, while a distinguishable expansion fan accelerates it in the post-shock region. The phenomenon is amplified with $\theta_d = 3°$, which induces a strong pressure gradient at the impinging location. Furthermore, for this large shock angle, a second re-circulation zone appears within the primary bubble. The separation bubble does not have a symmetrical structure, the length between the separation point x_s and x_{imp} is significantly greater than the distance between x_{imp} and the reattachment location x_r. Furthermore, with $\theta_d = 3°$, the back region of the bubbles reveals a time invariant wiggling behaviour which tends to perturb slightly the compression waves of the reattachment. Even though the largest shock strength could induce the transition from laminar to turbulent flow, the SFD method enforces a steady-state equilibrium of the solution.

The wall-normal velocity depicted in Fig. 5.2.2 shows the shock pattern of the SWBLIs. In case of the smallest deflection angle, the velocity is only disturbed around the shock impinging location. The small deflection of the boundary layer renders not distinguishable the compression waves at the reattachment and the expansion wave. Regarding the other cases, the shocks extend within the entire domain such that the whole flow field is strongly perturbed by the compression waves induced by the separation and the reattachment of the boundary layer. Wiggles are observable in the back region of the largest recirculation zone and reveal small stationary vortices close to the reattachment point. Sivasubramanian and Fasel [2015] highlight vortex shedding (i.e.

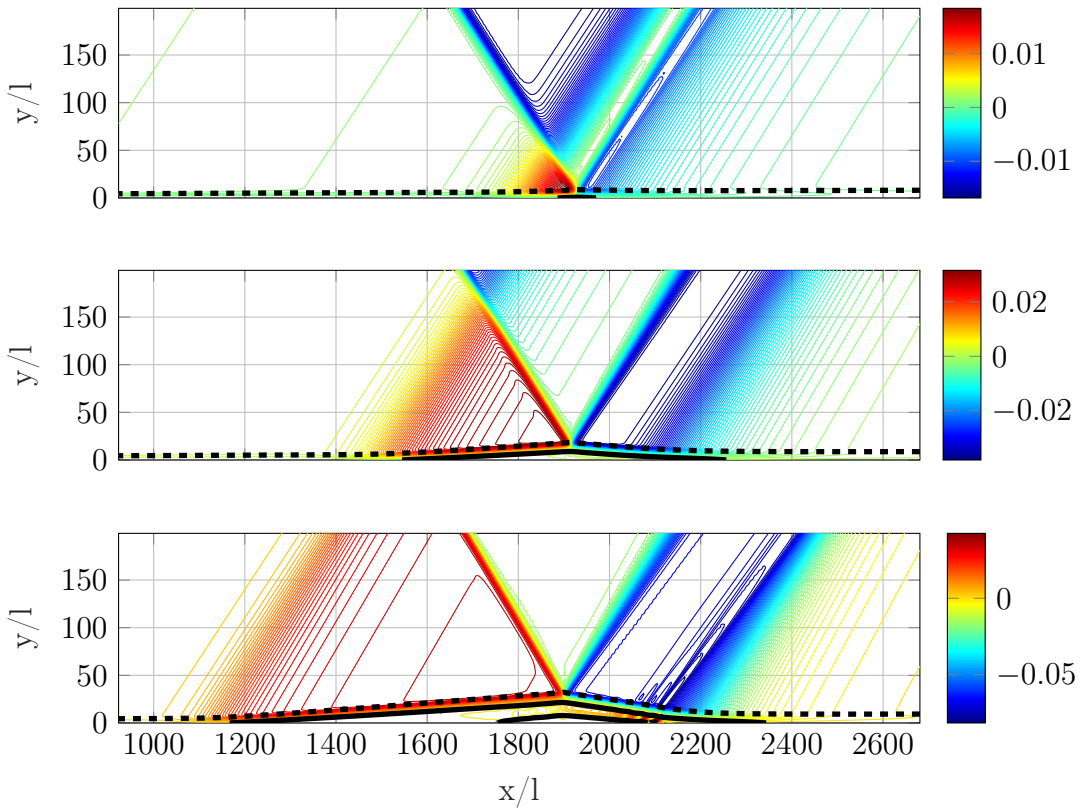

Figure 5.2.2: Wall-normal velocity $\overline{V}/\overline{U}_e$ for deflection angles $\theta_d = 1°$ (top), $\theta_d = 2°$ (intermediate) and $\theta_d = 3°$ (bottom). Black dashed lines for boundary layer height $\delta_{\overline{U}=0.9\overline{U}_e}$ and black solid lines for $\overline{U} = 0$ contours.

the unsteady phenomenon) at the back of the bubble for a laminar SWBLI computed by DNS without enforcing steady-state NSE. In addition, the vortex-like structure influences the compression waves at the rear of the bubble. In his experiments, Giepman [2016] does not notice such vortices, even for shock angles larger than $\theta_d = 3°$.

A comparison between the SWBLI and the undisturbed boundary layer with respect to velocity and temperature profiles at different streamwise locations is suggested in Fig. 5.2.3. The $\overline{U}$ profiles clearly show the regions where the velocity becomes negative at the wall. The separation is characterised by the wall-normal derivative of the streamwise velocity becoming zero first and then negative within the separated region. The largest shock angles shown in Fig. 5.2.3 reveal this feature undeniably, while it is more difficult to visualise for the case with $\theta_d = 1°$, due to the very short bubble. In addition, the SWBLI with $\theta_d = 3°$ induces a second bubble, which is characterised by a counter-clockwise recirculation zone, while the primary separation bubble depicts a clockwise rotation. It

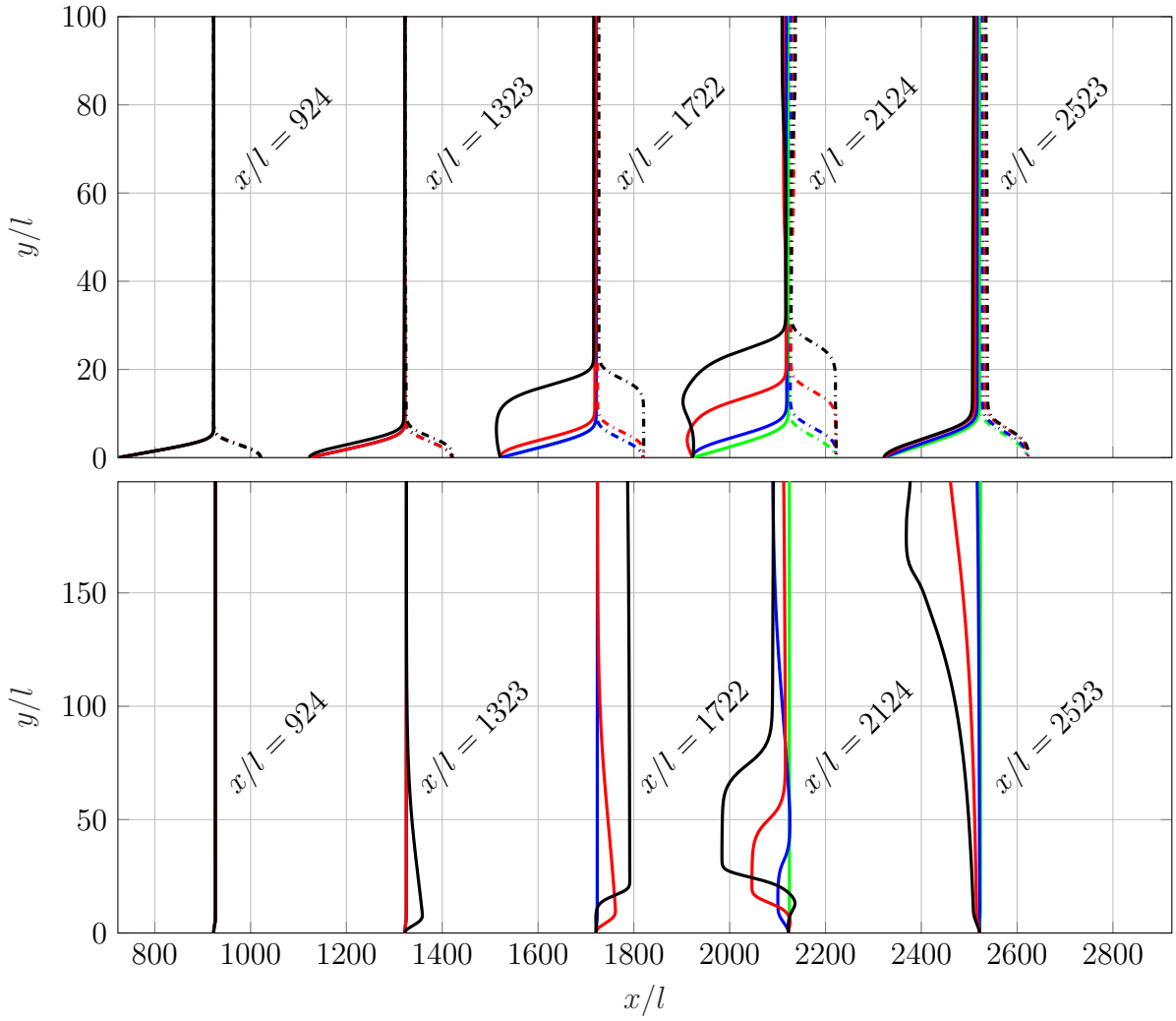

Figure 5.2.3: Profiles of $\overline{U}/\overline{U}_e$ (top, continuous line), of $\overline{T}/\overline{T}_e$ (top, dash dotted line) magnified by a factor 200 and of $\overline{V}/\overline{U}_e$ (bottom), magnified by a factor 200. Undisturbed boundary layer (green) and SWBLI with deflection angles $\theta_d = 1°$ (blue), $\theta_d = 2°$ (red) and $\theta_d = 3°$ (black). Note the different vertical scales for $\overline{U}/\overline{U}_e$ and $\overline{V}/\overline{U}_e$.

is highlighted in Fig. 5.2.3 at $x/l = 2124$, where the streamwise velocity is positive close to the wall. The wall-normal velocity $\overline{V}$, provides complementary information about the rotation of the flow within the bubble. Upstream of the shock impingement, the reversed flow has a positive $\overline{V}$ while a negative contribution is revealed in the downstream part. In addition, the wall normal velocity in the freestream portion is strongly affected by the shocks pattern. The lifting of the boundary layer at the separation point and the induced compression wave yields a positive wall-normal velocity in the freestream as depicted in Fig. 5.2.2 and Fig. 5.2.3.

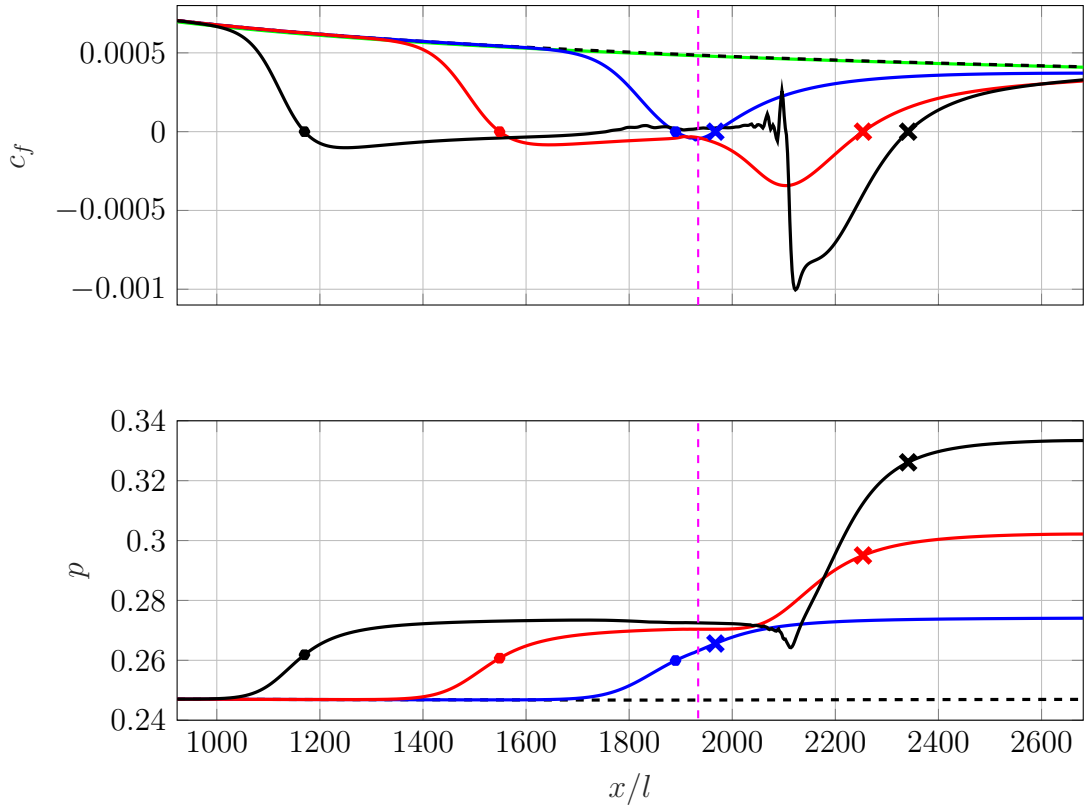

Figure 5.2.4: Friction coefficient (top) and non-dimensional pressure (bottom) along the wall for undisturbed boundary layer (black dashed line for DNS; green line for Eckert [1955]) and SWBLI with deflection angles $\theta_d = 1°$ (blue), $\theta_d = 2°$ (red) and $\theta_d = 3°$ (black). The shock impinging location is indicated by the magenta line. The separation and the reattachment points are indicated by the circles and the crosses, respectively.

The length of the bubbles is evaluated through the skin friction coefficient c_f, cancelling at the separation and the reattachment locations. Fig. 5.2.4 (top) shows the streamwise variation of c_f for all the SWBLI cases and for the undisturbed boundary layer computed with DNS. In addition, Fig. 5.2.4 depicts the theoretical friction coefficient for supersonic boundary layers derived by Eckert [1955]:

$$C_{f,Eckert} = 0.664 \frac{x}{\sqrt{\overline{\mu}_e}} \sqrt{C_r}, \qquad \text{where } C_r = \frac{\overline{\mu}_w \overline{T}_e}{\overline{\mu}_e \overline{T}_w}, \tag{5.2.1}$$

C_r is the Chapman-Rubesin constant (Chapman [1949]) relating the temperature and the viscosity. The subscript e indicates a quantity evaluated at the boundary layer edge

(i.e. freestream), while w refers to the wall. Fig. 5.2.4 shows that the skin friction computed with the DNS solver and with Eq. (5.2.1) are in perfect agreement. On the other hand, as a characteristic of the SWBLI, the skin friction exhibits a negative region where the boundary layer is separated. From the smallest shock angle to the largest, the lengths of the separation are respectively $L_{SB}/l = 77$, $L_{SB}/l = 705$ and $L_{SB}/l = 1170$. For $\theta_d = 3°$, the length of the secondary bubble is $L_{SB_2} = 348$. Furthermore, the friction coefficient within the second bubble exhibits strong oscillations caused by the steady vortex structure.

The streamwise pressure variation, depicted in Fig. 5.2.4, reveals several plateaus. The first plateau represents the constant freestream pressure $1/\gamma M^2 = 0.2471$, the second plateau is related to the separated region and the third gives the freestream pressure after the shock system. Again, the steady vortex structure of $\theta_d = 3°$ induces some oscillations at the end of the second plateau while the secondary bubble yields a slight decrease of the pressure. On the other hand, due to the size of the smallest bubble, the $\theta_d = 1°$ case exhibits only one rise from ante-shock to post-shock pressure. For strong interaction, i.e $\theta_d = 2°$ and $\theta_d = 3°$, the rise in pressure leading to the first plateau is described by the free interaction theory suggested by Chapman et al. [1958].

5.2.1 Free interaction theory

The free interaction theory argues that the increase of pressure p, yielding the first plateau, due the supersonic separation is independent from the mechanism inducing the interaction. Chapman et al. [1958] suggested the following correlation to determine the rise in pressure:

$$\frac{p - p_0}{q_0} \sim \sqrt{\frac{c_{f_0}}{\sqrt{M_0^2 - 1}}}, \tag{5.2.2}$$

where the subscript 0 indicates a quantity evaluated at the onset of the interaction $x = x_0$. In addition, the skin friction coefficient c_{f_0} and the dynamic pressure q_0 are defined as:

$$\tau_{w_0} = \frac{1}{2}\rho_0 U_0 c_{f_0}, \qquad q_0 = \frac{1}{2}\rho_0 U_0^2 = \frac{\gamma}{2} p_0 M_0^2, \tag{5.2.3}$$

with τ_w the wall shear stress and the freestream Mach number M.
Hakkinen et al. [1959] made the difference between the proportionality factors of Eq. (5.2.2) for the pressure at the separation point p_s and at the plateau p_{pl} such that:

$$\begin{cases} \frac{p_s - p_0}{q_0} & = C_{p_s} \quad \approx \mathcal{P}_s \sqrt{\frac{c_{f_0}}{\sqrt{M^2-1}}}, \\ \frac{p_{pl} - p_0}{q_0} & = C_{p_{pl}} \quad \approx \mathcal{P}_{pl} \sqrt{\frac{c_{f_0}}{\sqrt{M^2-1}}}, \end{cases} \tag{5.2.4}$$

where $\mathcal{P}_s = \sqrt{2}$ and $\mathcal{P}_{pl} = 1.65\sqrt{2}$. These relations are empirical. The experiments of Gadd [1953] showed $\mathcal{P}_s = 1.39$, while the correlation of the data provided by Chapman et al. [1958] return $\mathcal{P}_s = 1.19$ and $\mathcal{P}_{pl} = 2$ as highlighted by Hakkinen et al. [1959]. Erdos and Pallone [1963] proposed $\mathcal{P}_s = 1.15$ and $\mathcal{P}_{pl} = 2.08$. Katzer [1989] reveals $\mathcal{P}_s = 1.4$ and $\mathcal{P}_{pl} = 2.3$ with numerical simulations of SWBLI at several Mach and Reynolds numbers. On the other hand, Stewartson and Williams [1969]; Williams [1975] determine,

respectively, $\mathcal{P}_s = 1.45$ and $\mathcal{P}_{pl} = 2.55$ with the triple-deck solutions. This indicates that the coefficients $\mathcal{P}_s$ and $\mathcal{P}_{pl}$ can be slightly case dependent and should be determined through the correlation of numerical or experimental approaches by considering several shock strengths.

Stewartson and Williams [1969] developed a more elaborated theory based on the analysis conducted originally by Chapman et al. [1958]. The aim is to determine a continuous similarity function to describe the region where the free interaction applies, i.e. from x_0 to x_{pl}. Following the procedure summarised by Babinsky and Harvey [2011]; Matheis and Hickel [2015], the x-momentum equation related to the boundary layer reads:

$$\overline{\rho}\overline{U}\frac{\partial \overline{U}}{\partial x} + \overline{\rho}\overline{V}\frac{\partial \overline{U}}{\partial y} = -\frac{dp}{dx} + \frac{\partial \tau}{\partial y}. \tag{5.2.5}$$

At wall $y = 0$, where the no-slip conditions is enforced through $U = V = 0$, Eq. (5.2.5) degenerates into:

$$\frac{dp}{dx} = \frac{\partial \tau}{\partial y}\Big|_w = \frac{\partial \tau_w}{\partial y}, \tag{5.2.6}$$

for which the integration along the wall in the streamwise direction yields:

$$p(x) - p_0 = \int_{x_0}^{x} \frac{\partial \tau_w}{\partial y} dx. \tag{5.2.7}$$

In addition to the quantities introduced by Eq. (5.2.3), a non-dimensional length s is considered:

$$s = \frac{x - x_0}{L} = \frac{x - x_0}{x_s - x_0}, \tag{5.2.8}$$

with $L = x_s - x_0$ a characteristic length of the interaction. Therefore, the non-dimensional form of Eq. (5.2.7) reads:

$$\frac{p(s) - p_0}{q_0} = \frac{L}{\delta_0^*} c_{f_0} \int_{x0}^{x} \frac{\partial(\tau_w/\tau_{w_0})}{(\partial y/\delta_0^*)} dx = \frac{L}{\delta_0^*} c_{f_0} f_1(s), \tag{5.2.9}$$

where $f_1(s)$ is the first similarity function. On the other hand, Stewartson and Williams [1969] argue that the boundary layer is subjected to a deflection φ caused by the separation. According to Chapman et al. [1958], the linearised supersonic wave equation relating the pressure and the flow direction in the outer inviscid flow is applied to evaluate the deflection angle as follows:

$$\frac{d\delta^*(x)}{dx} = \varphi(x) - \varphi_0 \approx \frac{\sqrt{M_0^2 - 1}}{\gamma M_0^2} \frac{p(x) - p_0}{p_0} = \sqrt{M_0^2 - 1} \frac{p(x) - p_0}{q_0}. \tag{5.2.10}$$

Introducing the non-dimensional quantities in Eq. (5.2.10), the second equation relating the pressure rise in the free interaction region is written:

$$\frac{p(s) - p_0}{q_0} = \frac{L}{\delta_0^*} \left(\frac{d(\delta^*(s)/\delta_0^*)}{ds} \right) = \frac{L}{\delta_0^*} f_2(s), \tag{5.2.11}$$

with $f_2(s)$ the second similarity function. Finally, the correlation function $\mathcal{F}$ is defined as:

$$\mathcal{F} = \sqrt{f_1(s) f_2(s)} = \sqrt{\frac{p(s) - p_0}{q_0} \frac{\varphi - \varphi_0}{c_{f_0}}}, \tag{5.2.12}$$

and provides, therefore, a continuous relation to evaluate the free interaction region. In comparison, $\mathcal{P}$ from Eq. (5.2.4) only gives the correlation $\sqrt{2}\mathcal{F}$ for the separation point and the plateau:

$$P_s = \sqrt{2}\mathcal{F}_s \qquad \text{and} \qquad P_{pl} = \sqrt{2}\mathcal{F}_{pl} \tag{5.2.13}$$

Furthermore, note that Eq. (5.2.10) used by Chapman et al. [1958] considers a uniform incoming flow and, therefore, the similarity law cannot be applied, for instance, to nozzles where the curvature of the wall yields non-uniformities in the outer flow. To circumvent this limitation, Carrière et al. [1969] proposed the universal function:

$$\widetilde{\mathcal{F}} = \sqrt{\frac{p(s) - p_0}{q_0} \frac{\nu_0(s) - \tilde{\nu}(s)}{c_{f_0}}}, \tag{5.2.14}$$

where ν is the Prandtl-Meyer function:

$$\nu(s) = \sqrt{\frac{\gamma+1}{\gamma-1}} \arctan\left(\sqrt{\frac{\gamma-1}{\gamma+1}\left(M^2(s)-1\right)}\right) - \arctan\sqrt{M^2(s)-1}, \tag{5.2.15}$$

computed for the undisturbed boundary layer (ν_0) and for the shock-induced separation ($\tilde{\nu}$). The variation of the Mach number $M(s)$ in the streamwise direction is evaluated as follows:

$$M^2(s) = \frac{2}{\gamma-1}\left[\left(\frac{p_0}{p(s)}\right)^{\frac{\gamma-1}{\gamma}}\left(1 + \frac{\gamma-1}{2}M_0^2\right) - 1\right], \tag{5.2.16}$$

assuming an isentropic compression process. In the present case of flat plate flow, the universal similarity function $\widetilde{\mathcal{F}}$ is, therefore, in perfect agreement with $\mathcal{F}$. A comparison between the three shock angles of the current SWBLI is depicted in Fig. 5.2.5, where several characteristic values are shown. Note that the interaction onset is determined with the methodology proposed by Matheis and Hickel [2015] and consists of selecting x_0 where:

$$\frac{\delta(x)}{p_w(x)} \frac{dp}{dx}\bigg|_w \approx 10^{-5}, \tag{5.2.17}$$

with $\delta(x)$ the height of the undisturbed developing boundary layer. Fig. 5.2.5 shows a good correlation exists between $\mathcal{F}$ and $\widetilde{\mathcal{F}}$ for all the shock strengths, except $\theta_d = 1°$ for the plateau region. The dissimilarity between $\theta_d = 1°$ and the largest angles is due to very small separation bubble induced by the shock at $\theta_d = 1°$. In Fig. 5.2.4, the plateau representing the pressure within the bubble saturates rapidly into the last plateau related to the downstream pressure of the entire shock system. Such a weak separation does not verify the underlying strong shock assumption of free interaction theory. Therefore, the plateau for $\theta_d = 1°$, approximated by the similarity law in Fig. 5.2.5, is not representative of the actual constant pressure in the bubble. On the other hand, before $\mathcal{F}_{pl}$, the similarity functions evaluated for all the shock angles are in excellent

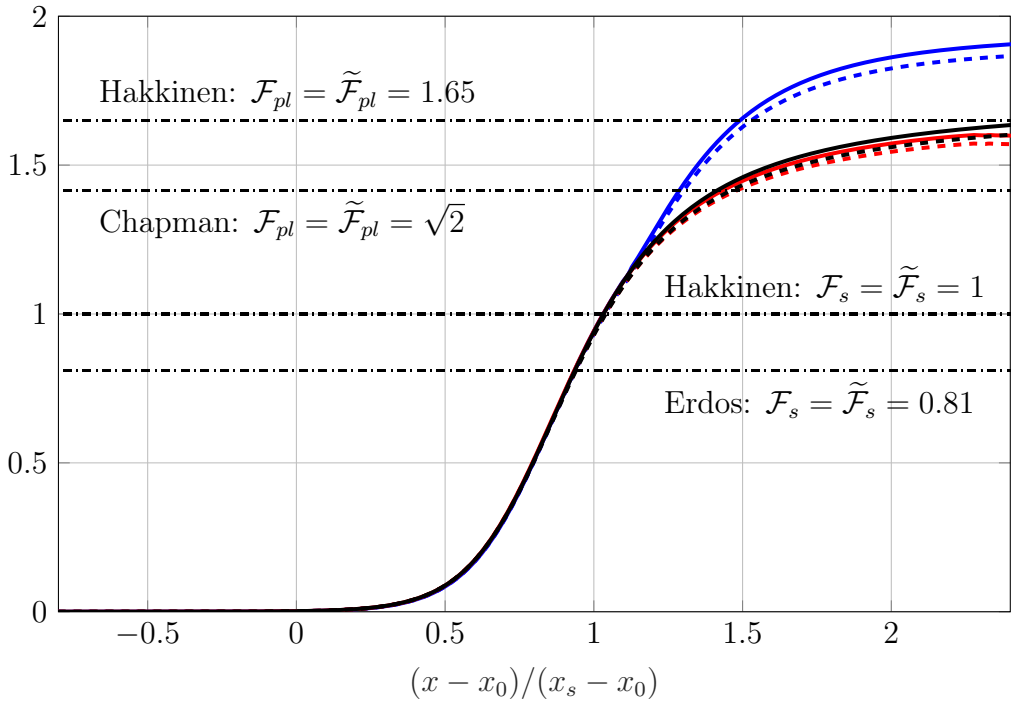

Figure 5.2.5: Similarity functions $\mathcal{F}$ (solid line) and $\widetilde{\mathcal{F}}$ (dashed line) for $\theta_d = 1°$ (blue), $\theta_d = 2°$ (red) and $\theta_d = 3°$ (black) with several values from the literature (dash dotted lines) for the separation (subscript s) and the plateau (subscript pl) converted from $\mathcal{P}$.

agreement. At the separation point ($s = 1$), $\mathcal{F}_s = 0.942$ is found for both $\theta_d = 1°$ and $\theta_d = 2°$ while the case $\theta_d = 3°$ reveals $\mathcal{F}_s = 0.940$. In regards of the universal function, $\widetilde{\mathcal{F}}_s = 0.934$ is observed for the smallest angles and $\widetilde{\mathcal{F}}_s = 0.928$ for the largest shock angle.

In order to estimate ultimately the bubble length in case of laminar SWBLI, Katzer [1989] proposed the use of a similarity law to determine the pressure rise due to the shock leading to an incipient separation, p_{inc}:

$$\frac{p_{inc} - p_0}{q_0} = \mathcal{P}_{inc}\sqrt{\frac{c_{f_{imp}}}{\sqrt{M^2 - 1}}}, \tag{5.2.18}$$

where $\mathcal{P}_{inc} = 2\sqrt{2}$ as stated by Greber et al. [1958], while Rizzetta et al. [1978] show $\mathcal{P}_{inc} = 1.57\sqrt{2}$ with the triple-deck theory. In his own numerical experiments, Katzer [1989] found $\mathcal{P}_{inc} = 1.85\sqrt{2}$. Note that the skin friction coefficient $c_{f_{imp}}$ is measured at the impinging location of an undisturbed boundary layer, leading to small dissimilarity with previous analyses, where c_{f_0} was used. Eq. (5.2.18) does not need the location of the beginning of the interacting region and is more practical to use as only one undisturbed boundary layer solution is required. Finally, the similarity law derived by Katzer [1989] for the length of laminar separation bubbles reads:

$$\frac{l_{SB}}{\delta^*_{imp}} M^3 \sqrt{\frac{C_r}{Re_{x,imp}}} = 4.4 \frac{p_3 - p_{inc}}{p_e}, \tag{5.2.19}$$

where p_3 is the pressure downstream of the entire shock system. In Fig. 5.2.6, the different lengths recorded by Giepman [2016] are compared to the current DNS and the

similarity law of Eq. (5.2.19) with the two $\mathcal{P}_{inc}$ based on the work of Greber et al. [1958] and Rizzetta et al. [1978] in order to provide a bounded interval. The DNS results are in excellent agreement with respect to the analytical formulation such that the slope reveals an intermediate value $\mathcal{P}_{inc} \approx 1.72\sqrt{2}$, close to the value $\mathcal{P}_{inc} \approx 1.85\sqrt{2}$ observed by Katzer [1989]. Nonetheless, the experimental data of Giepman [2016] shows strong discrepancies with respect to both similarity law and DNS. While the experimental bubble with $\theta_d = 1°$ is twice as large as the DNS one, the two other largest bubbles are definitely underestimated. The low seeding density due to the sub-millimeter laminar boundary layer thickness and the wall reflections in the reversed flow region cause these measurement errors in the experiments, as briefly highlighted by Giepman [2016]. In addition, the TST-27 blowdown transonic/supersonic wind tunnel of Delft University of Technology exhibits freestream fluctuations, yielding a flow not strictly steady which can reduce the length of the separation bubble.

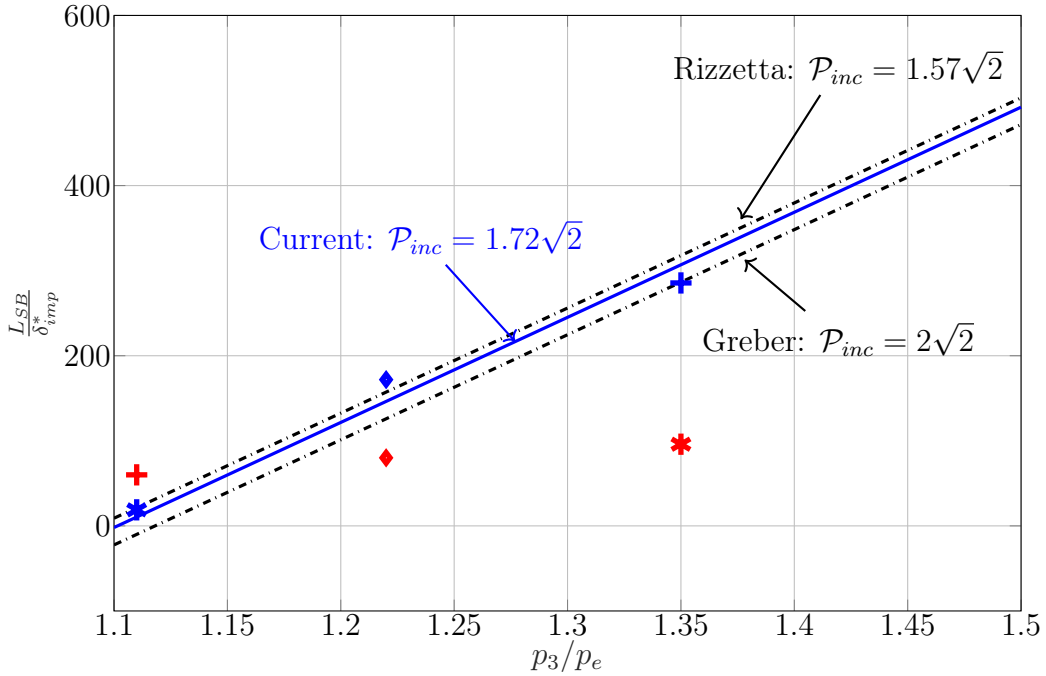

Figure 5.2.6: Comparison of the bubble length (normalised by δ^*_{imp}) predicted by similarity law (black lines) with experiments (red) of Giepman [2016] and current DNS (blue) for the three deflection angles: $\theta_d = 1$ (star), $\theta_d = 2°$ (diamond) and $\theta_d = 3°$ (cross).

The angle of flow deflection α_{SB} due the boundary layer separation is evaluated by Giepman [2016] with:

$$\alpha_{SB} = \arctan\left(0.5 C_{p_{pl}} \sqrt{M^2 - 1}\right), \tag{5.2.20}$$

and relies on the pressure rise of the first plateau $C_{p_{pl}}$ evaluated with the free interaction theory. Giepman [2016] computed $\alpha_{SB} = 1.8°$ with $\mathcal{P}_{pl} = 1.65\sqrt{2}$ (Hakkinen et al. [1959]) for the experimental SWBLI with $\theta_d = 3°$. Giepman [2016] revealed excellent agreements between Eq. (5.2.20) and the measured recirculation zone although the bubble length does not match with the similarity law. It concludes that the experiments significantly underestimate the height of the reversed flow in the same way as the length. In regards to the current DNS, the flow deflections are computed with respect to all the SWBLI cases

as depicted in Fig. 5.2.7. Furthermore, several $\mathcal{P}_{pl}$ values provided by the literature for the empirical plateau pressure are considered. Fig. 5.2.7 shows that the parameter $\mathcal{P}_{pl}$ (blue curve), chosen by Giepman [2016] provides an overestimated deflection angle for all θ_d while it showed good agreement with the experimental $\theta_d = 3°$. This could be caused by the evaluation of the friction coefficient, for Eq. (5.2.4), which depends on the onset of the interaction region. Due to the underestimated bubble length in the experiments, the skin friction of the undisturbed boundary layer case is significantly smaller than the one from DNS. Consequently, with a fixed $\mathcal{P}_{pl} = 1.65\sqrt{2}$, Eq. (5.2.20) returns a smaller deflection angle for the experiments than for the numerical simulations. In contrast, $\mathcal{P}_{pl} = 2$ provides a deflection angle in perfect agreement with the current DNS for $\theta_d = 3°$. Nevertheless, even with $\mathcal{P}_{pl} = 2$, small discrepancies are found for the two smallest shock angles. Such observations are consistent with the slight overestimation of the bubble length depicted in Fig. 5.2.6. Finally, Fig. 5.2.7 clearly depicts the triangular shape of the bubble, which becomes more curved towards the bubble centre when the shock strength increases.

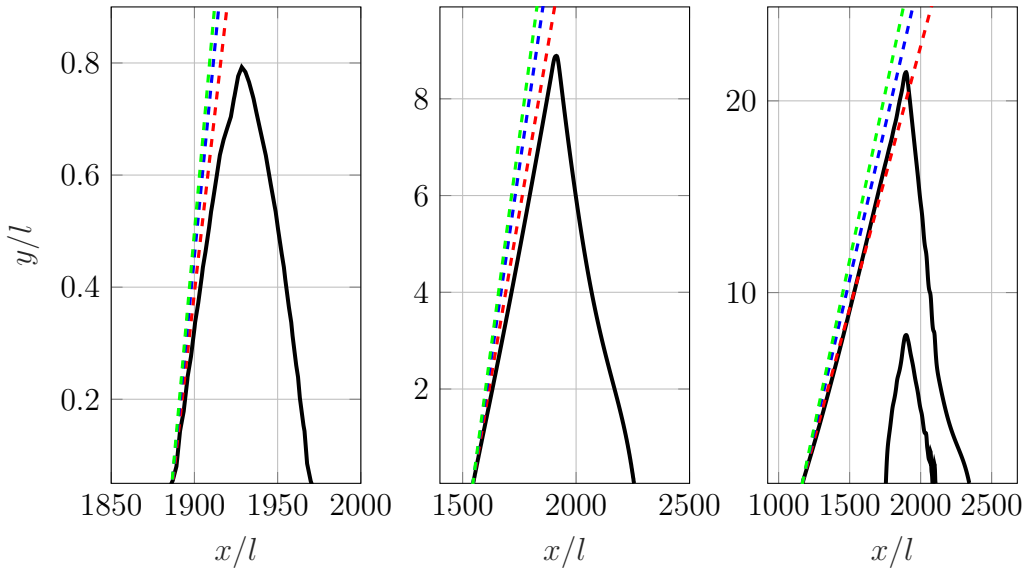

Figure 5.2.7: Separation bubbles for $\theta_d = 1$ (left), $\theta_d = 2°$ (middle) and $\theta_d = 3°$ (right) with theoretical flow deflections α_{SB} for $\mathcal{P}_{pl} = 2$ (red), $\mathcal{P}_{pl} = 1.65\sqrt{2}$ (blue) and $\mathcal{P}_{pl} = 2.55$ (green).

5.3 BiGlobal stability analysis

In this section, the numerical set-up used for the BiGlobal approach is discussed and is followed by the stability analyses. The first aim is to identify the most dominant convective mode present in the SWBLI with an intermediate shock angle and, second, to characterise a typical steady global mode exhibited by the separation bubble at $\theta_d = 2°$ and $\theta_d = 3°$. The SWBLI with $\theta_d = 1°$ is not handled as the small separation does not provide strong modification of the modes already observed in the undisturbed developing boundary layer. In addition, the resolution of the BiGlobal grid is not sufficient to

distinguish the existence of a global mode in the small confinement of the bubble.

5.3.1 Numerical set-up

The number of collocation nodes in the x and y-directions is $(N_\xi \times N_\eta) = (150 \times 50)$ lying in the domain defined by the dimensions $(x, y)/l \in [923, 2681] \times [0, 200]$. The bi-quadratic mapping is applied in both directions such that the regions with the largest shear stress are significantly resolved, because these regions are the main origins of the instabilities. As the majority of the stability analyses are conducted with $\theta_d = 2°$, it consists of the reference case for the selection of the parameters for the bi-quadratic mapping:

$$\begin{cases} x_{i1}/l = 1820 \\ x_{i2}/l = 1995 \end{cases}, \qquad \begin{cases} y_{i1}/l = 10 \\ y_{i2}/l = 30 \end{cases}. \tag{5.3.1}$$

It results in a refinement of the shear layer around the separation bubble as depicted in Fig. 5.3.1 by a high density of collocation nodes in this particular region. In order to compare the spectra directly, the same grid arrangement has been used for the two other SWBLI cases even though it does not consist of an optimal node repartition due do dissimilar bubble sizes. Finally, the DNS base flow is interpolated with a spline method over the grid used for the BiGlobal analysis.

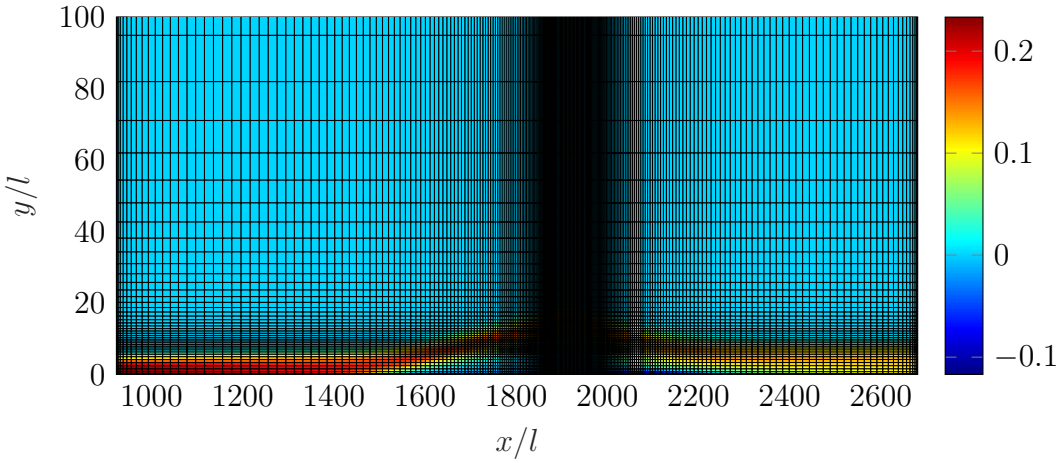

Figure 5.3.1: BiGlobal collocation grid superimposed on the shear stress $\overline{\mu}\partial\overline{U}/\partial y$.

5.3.2 Convective instabilities

The analyses in the current section are conducted with a infinite spanwise wave length (i.e $\beta = 0$) for comparison purpose with the supersonic boundary layer previously investigated. The convective instability observed for the developing boundary layer was the TS mode and arises as a branch in the BiGlobal spectrum. The introduction of a shock impinging on the boundary layer tends to change the characteristics of this convective mode branch as depicted in Fig. 5.3.2. Note that the branches are isolated from the rest of the spectra for sake of clarity. The circles continuing the branch for

$\theta_d = 2°$ indicate that the Nyquist limit of the current domain is reached. It implies that the grid size in the streamwise direction does not sufficiently resolve larger wavenumbers.

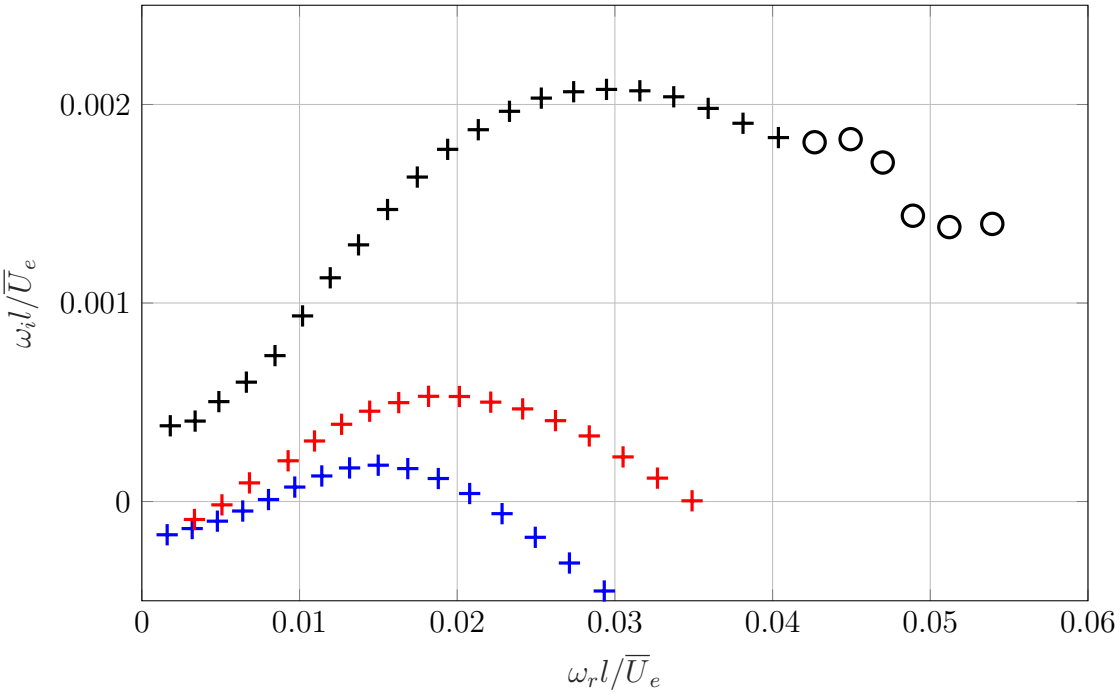

Figure 5.3.2: Tollmien-Schlichting branch for undisturbed supersonic boundary layer (blue), SWBLI with $\theta_d = 1°$ (red) and SWBLI with $\theta_d = 2°$(black). The black circles indicate the reached Nyquist limit.

When the shock strength is increased, all the eigenvalues present on the branch have a larger imaginary part, the entire branch becomes more and more unstable. A shock angle of $\theta_d = 1°$ yields a slight lift of the branch with only a very small amplification of the TS mode found in the eigenfunctions. The behaviour of the TS mode is, therefore, very similar to the supersonic boundary layer. From $\theta_d = 1°$ to $\theta_d = 2°$, the spectrum reveals a strong increase of the growth rate of the entire branch. Moreover, the convective mode is subjected to non-negligible structural changes such as the TS instability evolves into a Kelvin-Helmholtz (KH) instability over the bubble. As mentioned by Rist [2005] about incompressible laminar bubbles, the shift from TS to KH modes occurs smoothly when the shear layer is lifted from the wall. The former is a viscous instability existing only close to the wall in the boundary layer, while the latter is an inviscid, pressure driven, process. It takes place in free shear layers where the velocity profile contains an inflection point. Nonetheless, Rist [2005] showed that the shift from TS to KH modes can only be distinguished if the shear layer of the boundary layer is sufficiently distant from the wall; the deflection of the boundary layer due to the separation bubble has to be large enough. The convective eigenfunctions of $\theta_d = 1°$ do not lift up from the wall and thus cannot be labelled as KH modes. The inverse process from KH to TS waves is also a possibility as highlighted by Masahito et al. [1996] with the separation bubble over a backward step.

For $\theta_d = 2°$, the evolution of the wave packet related to the branch is shown in

Fig. 5.3.3 and Fig. 5.3.4 for an initial impulsion at $(x_0, y_0, t\overline{U}_e)/l = (973, 2, 0)$. From the generation of the perturbation to $t\overline{U}_e/l = 1000$, the wave packet simply travels downstream with a slight decay in amplitude. In addition to the first main structure above the boundary layer, a second smaller structure exist within the boundary layer and propagates downstream at a lower speed. When the first structure crosses the impinging shock, a part of the perturbation enters the shear layer and the second perturbation is amplified when reaching the separation point. At $t\overline{U}_e/l = 1250$, the bubble exhibits an absolute mechanism, propagating the first structure upstream and downstream of the shock within the shear layer. At the same instant, the second structure perturbs the reversed flow region at the separation location and a third structure appears before the reattachment of the boundary layer. Finally, the entire wave packet amplified by the bubble is observable at $t\overline{U}_e/l = 1500$. Moreover, the typical features of the KH waves are visible at $t\overline{U}_e/l = 1750$ and at $t\overline{U}_e/l = 2000$. Namely, the maximum amplitude of the modes is reached exactly where the shear has its highest value. The peak of the KH wave packet amplitude is followed by smaller parts near the wall and in the freestream. It differentiates the KH instabilities from the TS instabilities, where the maximum amplitude occurs close to the wall and decays exponentially in the freestream only.

At $t\overline{U}_e/l = 2250$, the wave packet reveals structural features associated to the TS and KH waves at the same time. The former appeared in the separated region, where the shear layer is lifted, while the latter becomes dominant after reattachment. Similar shifting has been observed by Masahito et al. [1996] with an incompressible flow over a backward facing step, exhibiting KH waves over the separated region and TS waves after the reattachment. It confirms the close link existing between the instabilities. Finally, the generated wave packet leaves the bubble with an amplitude increased by a factor of 30 with respect to the initial amplitude measured at $(x_0, y_0, t\overline{U}_e)/l = (973, 2, 0)$. The separation bubble acts, therefore, as a perturbation amplifier.

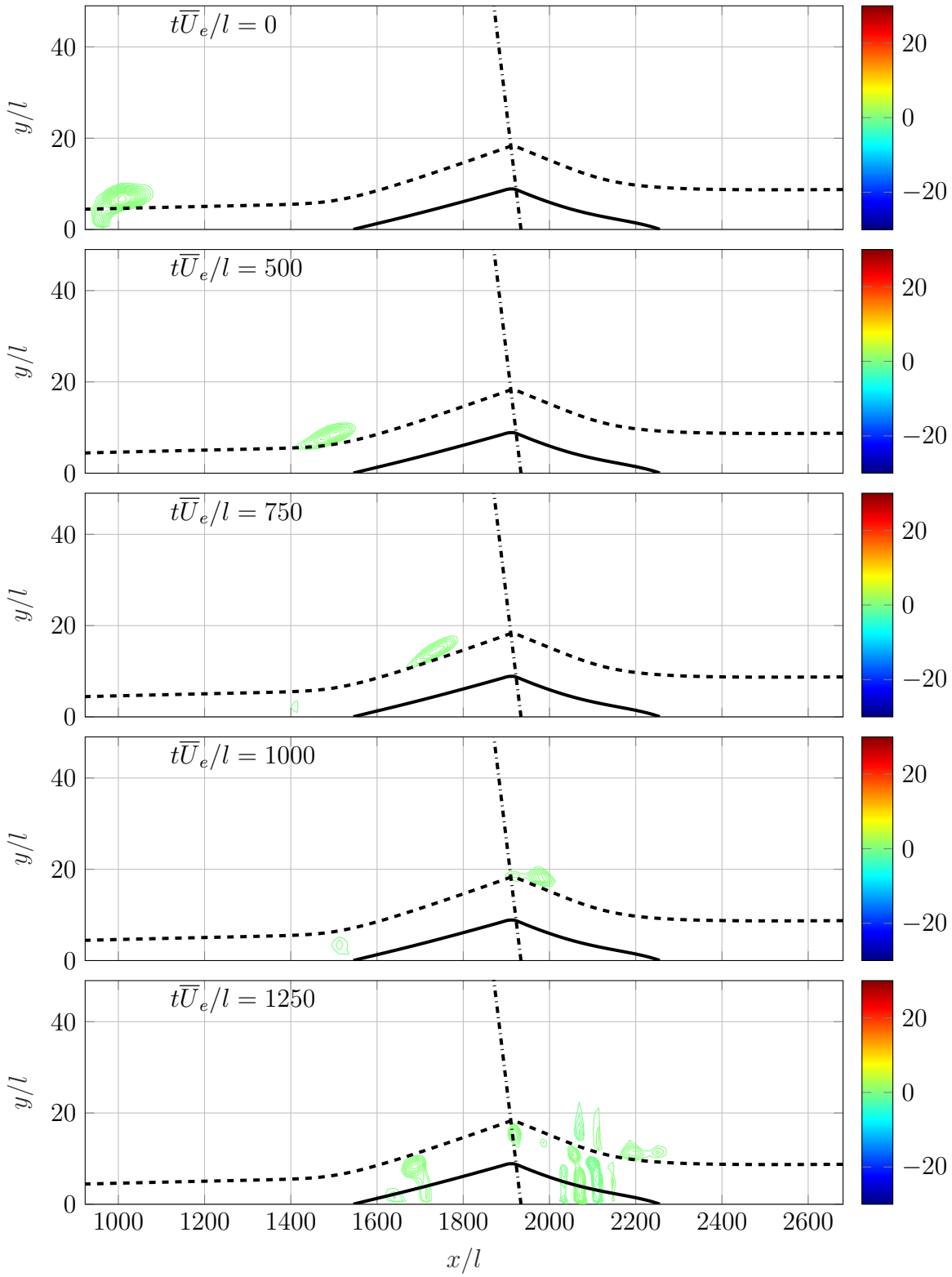

Figure 5.3.3: Snapshots at different times $t\overline{U}_e/l$ of the convective instability as a wave packet represented by the phase $\Re(\tilde{u})/|\tilde{u}_{t=0}|_{max}$ with separation bubble (solid line), $\delta_{\overline{U}=0.9}$ (dashed line), and incident oblique shock (dash dotted line).

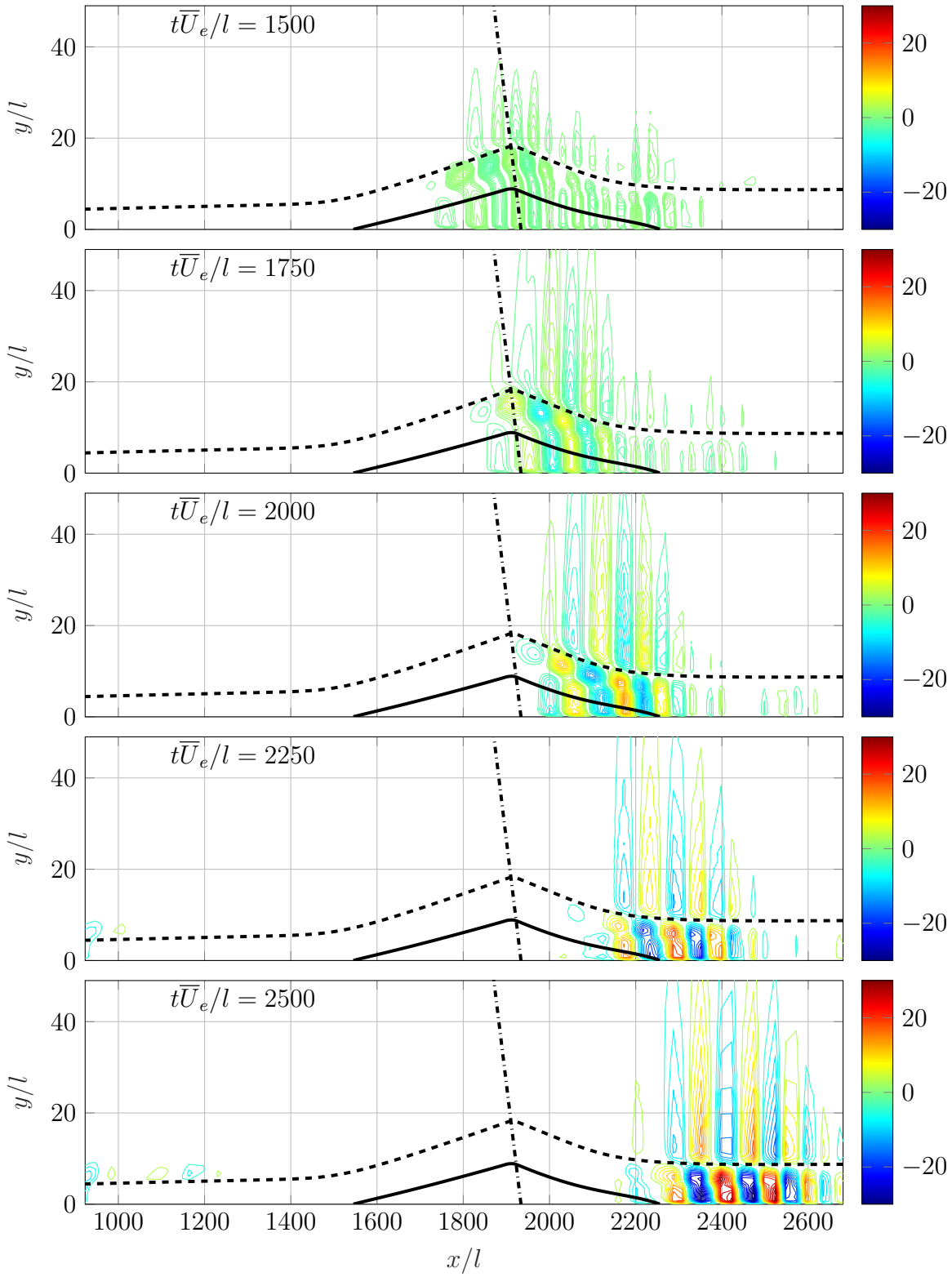

Figure 5.3.3: Snapshots at different times $t\overline{U}_e/l$ of the convective instability as a wave packet represented by the phase $\Re(\tilde{u})/|\tilde{u}_{t=0}|_{max}$ with separation bubble (solid line), $\delta_{\overline{U}=0.9}$ (dashed line), and incident oblique shock (dash dotted line).

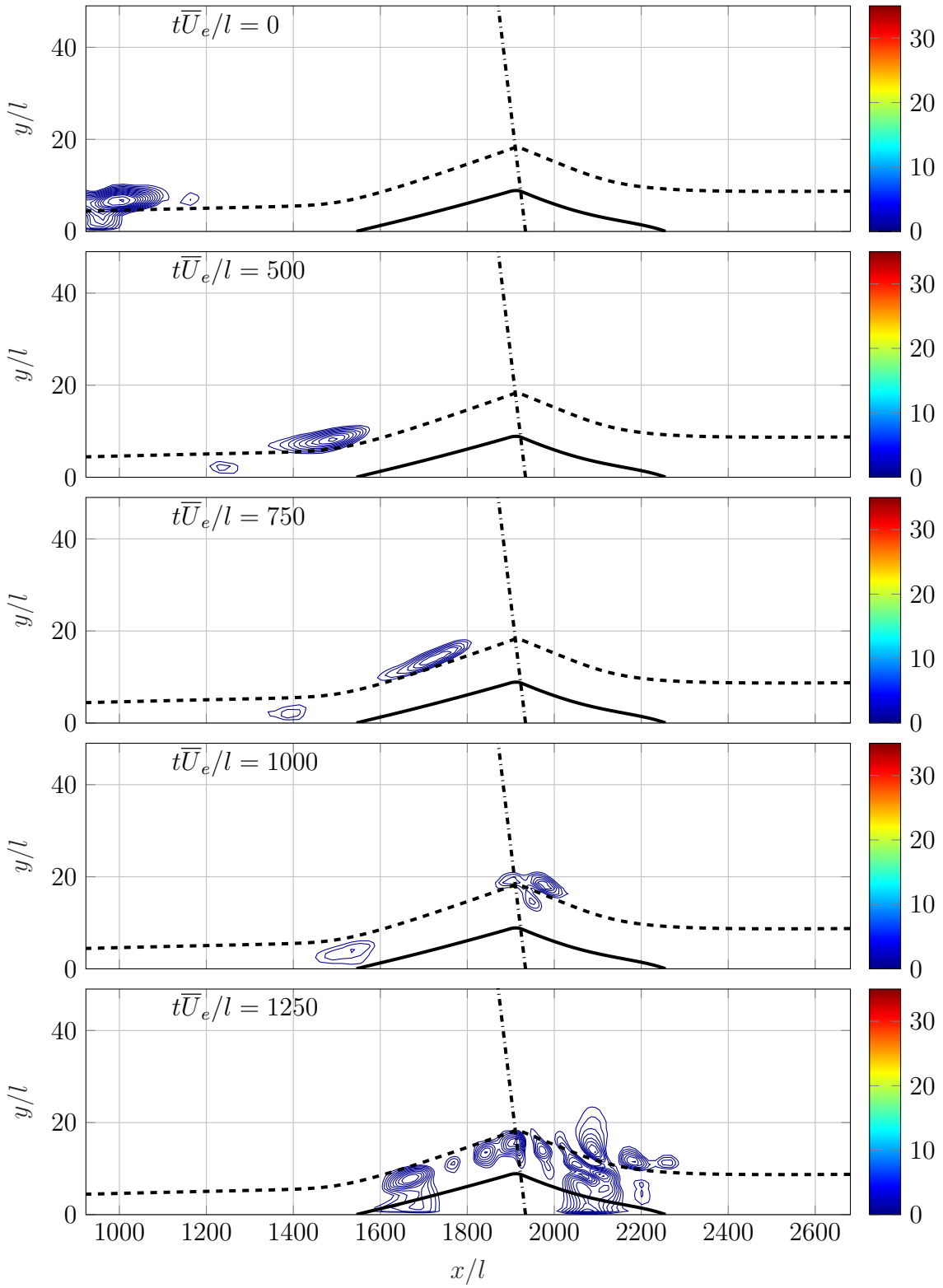

Figure 5.3.4: Snapshots at different times $t\overline{U}_e/l$ of the convective instability as a wave packet represented by the amplitude $|\tilde{u}|/|\tilde{u}_{t=0}|_{max}$ with separation bubble (solid line), $\delta_{\overline{U}=0.9}$ (dashed line), and incident oblique shock (dash dotted line).

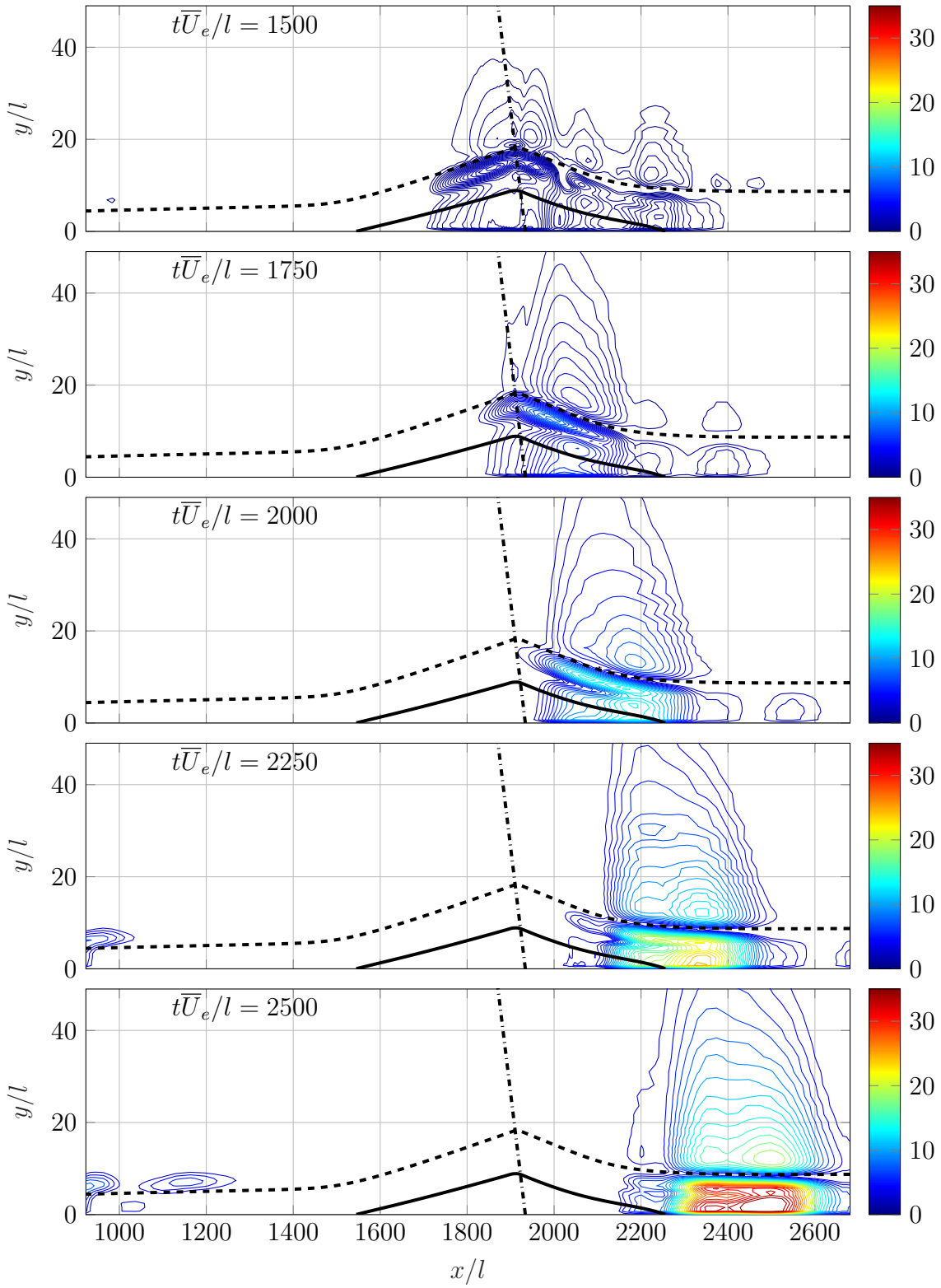

Figure 5.3.4: Snapshots at different times $t\overline{U}_e/l$ of the convective instability as a wave packet represented by the amplitude $|\tilde{u}|/|\tilde{u}_{t=0}|_{max}$ with separation bubble (solid line), $\delta_{\overline{U}=0.9}$ (dashed line), and incident oblique shock (dash dotted line).

The determination of the most dominant of the 111 terms in the BiGlobal momentum equations relies on the Reynolds-Orr energy budget (Schmid and Henningson [2001]). It is depicted in Fig. 5.3.5 for the TS-KH branch of the undisturbed boundary layer and the SWBLI with $\theta_d = 2°$. The ω_i-budget provides information about the physical phenomena inducing the temporal instability of the mode through the production or destruction of perturbation energy, while the ω_r-budget gives the contribution to the dispersion of the modes, i.e. representative of the advection speed of the convective waves. Due to the difference of the growth rates between the SWBLI and the boundary layer, all terms contributing to the ω_i-budget of the SWBLI are one order of magnitude higher than for the boundary layer. Regarding the supersonic boundary layer, Fig. 5.3.5 reveals a different energy budget for the mode $\omega_r l/\overline{U}_e \approx 0.0188$ of the TS branch, which is subjected to an interaction with a spurious mode as mentioned in section 4.3.2. Although shown for sake of completeness, this spurious mode is not considered in the analysis.

The ω_r-budget highlights that the terms $\gamma M^2 \frac{\overline{P}}{\overline{T}} \tilde{u}^* \tilde{u}_x \overline{U}$ and $\gamma M^2 \frac{\overline{P}}{\overline{T}} \tilde{v}^* \tilde{v}_x \overline{U}$ are ruling the dispersion of the modes. The perturbation variables $\tilde{u}$ and $\tilde{v}$ are mainly advected by the streamwise velocity $\overline{U}$. These two advection terms confirm that the KH and TS instabilities are convective modes. In the ω_i-budget, the advection term $\gamma M^2 \frac{\overline{P}}{\overline{T}} \tilde{u}^* \tilde{u}_x \overline{U}$ has significantly different behaviours on the growth rate if the boundary layer is subjected to a shock. For the SWBLI case, dominated mainly by KH instabilities, it has a destabilising effect on the mode. In contrast, the TS waves exhibited by the developing boundary layer are subjected to a stabilising effect from the advection term $\gamma M^2 \frac{\overline{P}}{\overline{T}} \tilde{u}^* \tilde{u}_x \overline{U}$. In addition, both TS and KH modes exhibit an advection of $\tilde{u}$ ($\gamma M^2 \frac{\overline{P}}{\overline{T}} \tilde{u}^* \tilde{u}_y \overline{V}$) in the wall-normal direction which is stabilising for the KH waves while it destabilises the TS waves. The two terms related to the gradient of the perturbation pressure are tedious to analyse in term of instability growth $\omega_i l \overline{U}_e$. Nonetheless, from the ω_r-budget, $-\tilde{u}^* \tilde{p}_x < 0$ can be seen as an increasing perturbation pressure in the streamwise direction that works against $\tilde{u}$, yielding in a slowdown of the dispersion of the velocity perturbation. The same interpretation is valid for $-\tilde{v}^* \tilde{p}_y$ in the wall-normal direction. The two pressure balances act in the same way on the mode of the undisturbed boundary layer and the SWBLI.
The $\gamma M^2 \frac{\overline{P}}{\overline{T}} \tilde{u}^* \tilde{v} \overline{U}_y$ reaction term involved in the TS-KH branch represents the Reynolds stress due to the intense shear related to $\overline{U}_y$. As highlighted by the ω_i-budget, it is the main contribution to the growth rate of both KH and TS modes. The dominating presence of the Reynolds stress reveals a destabilising effect, that can be related to later turbulence production extracting energy from the base flows. Finally, the growth rate is dictated by the diffusive term $\frac{\overline{\mu}}{Re} \tilde{u}^* \tilde{u}_{yy}$ which represent both diffusive transport and dissipation. Nevertheless, the former quantity cancels over the interior of the domain and, therefore, the ω_i-budget shows that energy is dissipated through viscosity, yielding a stabilising effect. The dissipation process is significantly higher for the TS mode than the KH modes and it justifies that the latter is an inviscid instability while the former is due to the viscous effect within the boundary layer.

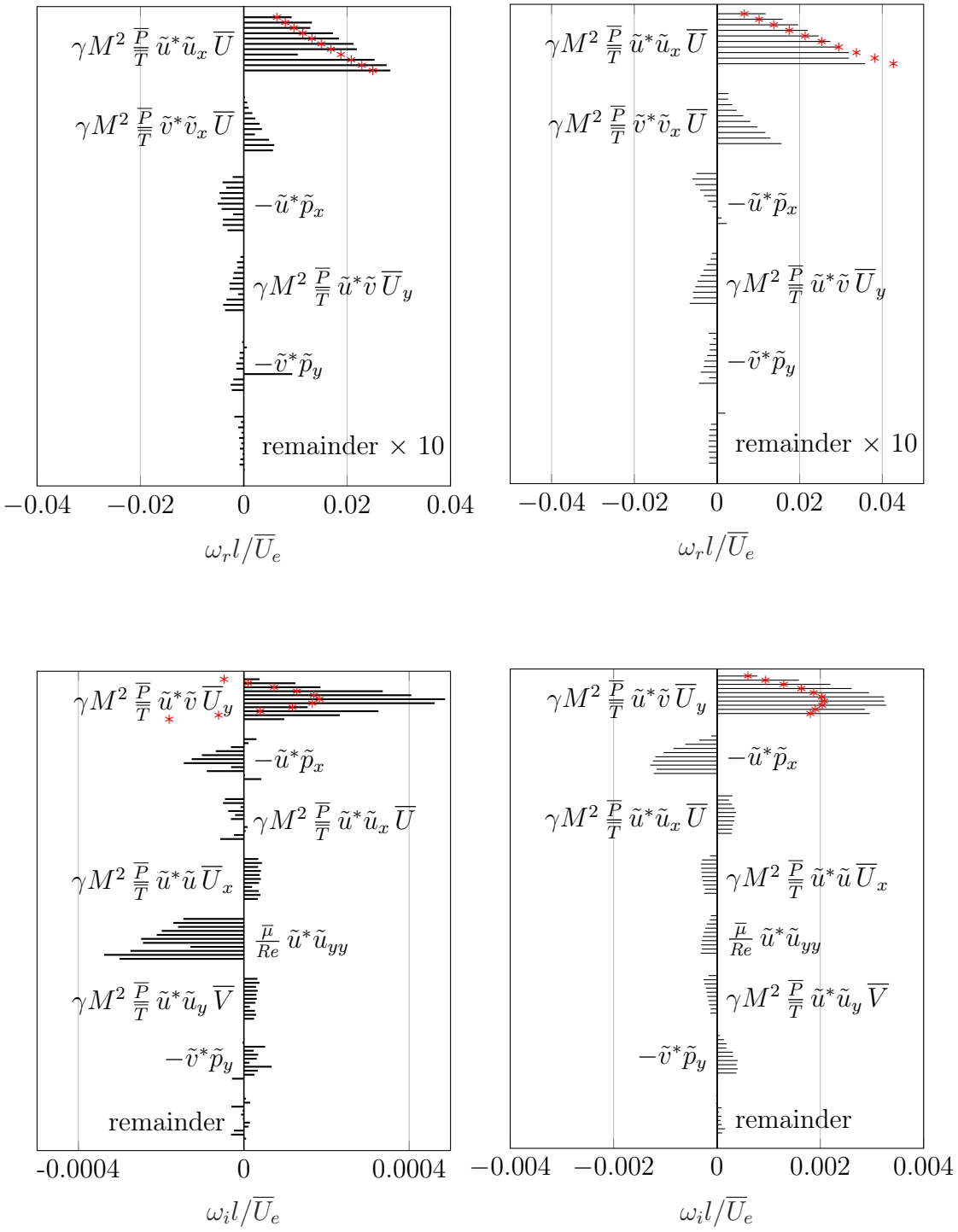

Figure 5.3.5: Most dominant Reynolds-Orr balance terms for KH/TS branch: ω_r-budgets (top) and ω_i-budgets (bottom) with related real and imaginary parts of the complex frequency $\omega l/\overline{U}_e$ (red asterisks). Undisturbed boundary layer (left) and SWBLI with $\theta_d = 2°$ (right). The remainders contributing to the real part are magnified with a factor of 10.

5.3.3 Global steady modes

The identification of the global unstable steady modes in the spectrum has only been successful in the research of Robinet [2007] for a well known case of laminar SWBLI. Robinet [2007] shows with BiGlobal analysis that a bifurcation exists from a 2D steady to a 3D steady separation bubble when the shock strength is increased. From a stability point of view, it implies that a stable global mode becomes unstable when the shock is strong enough. In regards of the spectrum, it implies that the eigenvalue crosses the real axis such that the growth rate becomes positive, along the imaginary axis, implying its steadiness. It yields a bifurcation from a steady bubble with an infinite wavelength in the spanwise direction to a steady bubble with a periodic pattern in this specific direction. In addition to this steady feature, Robinet [2007] showed through DNS that continuing to increase the shock strength leads to a second bifurcation from a 3D steady to a 3D unsteady flow organisation of the bubble. Nevertheless, such transition has not be shown by the author with BiGlobal analysis.

For the present numerical experiments, the flow conditions are totally different from the reference case (Degrez et al. [1987]) used by Robinet [2007] and it is, therefore, difficult to argue that a physical global steady mode exists in the current SWBLI. The presence of a low-frequency unsteadiness instead of steady modes due to the second bifurcation must not be discarded. Nevertheless, the complexity of the SWBLI spectrum and the low number of considered shock angles do not allow to identify such bifurcation. Consequently, in the current section, two modes (one at $\theta_d = 2°$ and one at $\theta_d = 3°$) lying

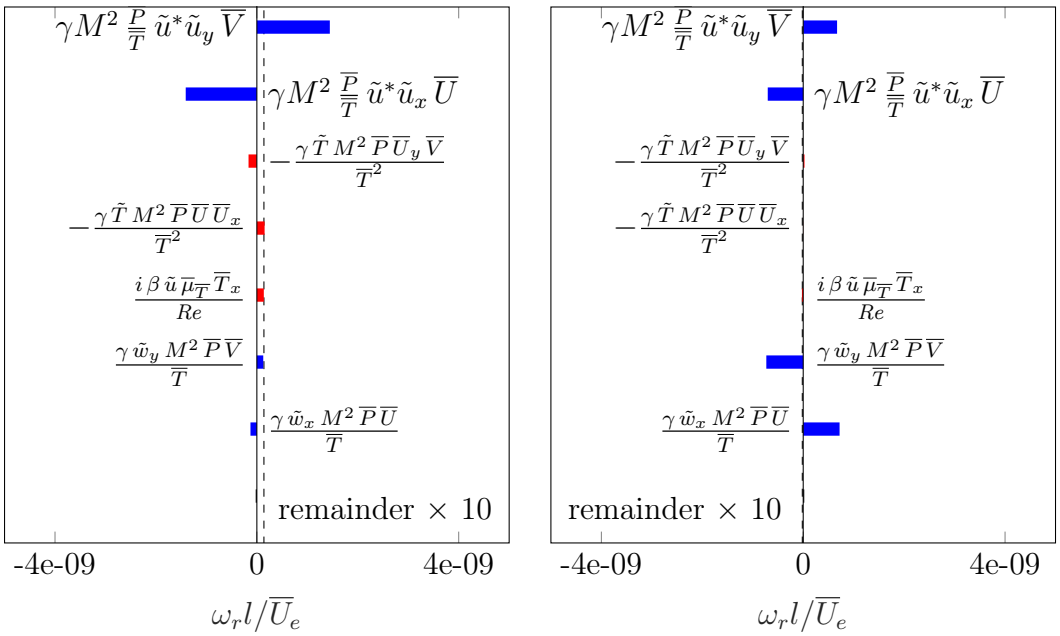

Figure 5.3.6: Most dominant Reynolds-Orr balance terms for steady modes: ω_r-budgets (top) and ω_i-budgets (bottom) with related real and imaginary parts of the complex frequency $\omega l/\overline{U}_e$ (black dashed line). SWBLI with $\theta_d = 2°$ (left), $\omega = -0.001507i$, and $\theta_d = 3°$ (right), $\omega = -0.000218i$. The advection terms are highlighted in blue and the remainders contributing to the real part are magnified with a factor of 10.

on the imaginary axis are analysed to characterise the features common to such modes. Even though the convergence study conducted in x and y-directions for both cases does not reveal a clear trend allowing to identify irrevocably the physical integrity of the modes, the two most converged ones are retained for the following analysis. The BiGlobal stability analysis are performed with β such that the assumed spanwise wavelength corresponds to $0.75L_{SB}$. This an approximate value of the most unstable spanwise wavelength observed in a laminar separation bubble with shock (Robinet [2007]) and with incompressible flow (Rodriguez [2010]).

The identification of the physics underlying the steady mode is carried out through the evaluation of the Reynolds-Orr energy budget as depicted in Fig. 5.3.6. For both shock angles, the advection has the most dominant contribution to the dispersion of the steady modes. Nonetheless, the order of magnitude of all terms in the ω_r-budget are very small. A different expected scenario, where the advection is balanced by the action of other terms, is therefore precluded. As a consequence, the mode is not advected; it is a steady standing wave. The explanation is found by considering the mathematical expression of the dispersion relation for the advection appearing in the ω_r-budget:

$$\Re\Big\{A^{\overline{U}} + A^{\overline{V}} + \underbrace{A^{\overline{W}}}_{0}\Big\} = \gamma M^2 \frac{\overline{P}}{\overline{T}} \begin{bmatrix} \overline{U} \\ \overline{V} \\ \overline{W} \end{bmatrix} \cdot \Im \left\{ - \begin{bmatrix} \tilde{\mathbf{q}}^* \cdot \partial\tilde{\mathbf{q}}/\partial x \\ \tilde{\mathbf{q}}^* \cdot \partial\tilde{\mathbf{q}}/\partial y \\ \tilde{\mathbf{q}}^* \cdot i\beta\tilde{\mathbf{q}} \end{bmatrix} \right\} \tag{5.3.2}$$

with A the advection of the eigenfunctions by the velocity indicated with the superscript and $\tilde{\mathbf{q}}$ the perturbation velocity vector. The entire expression of the Reynolds-Orr terms

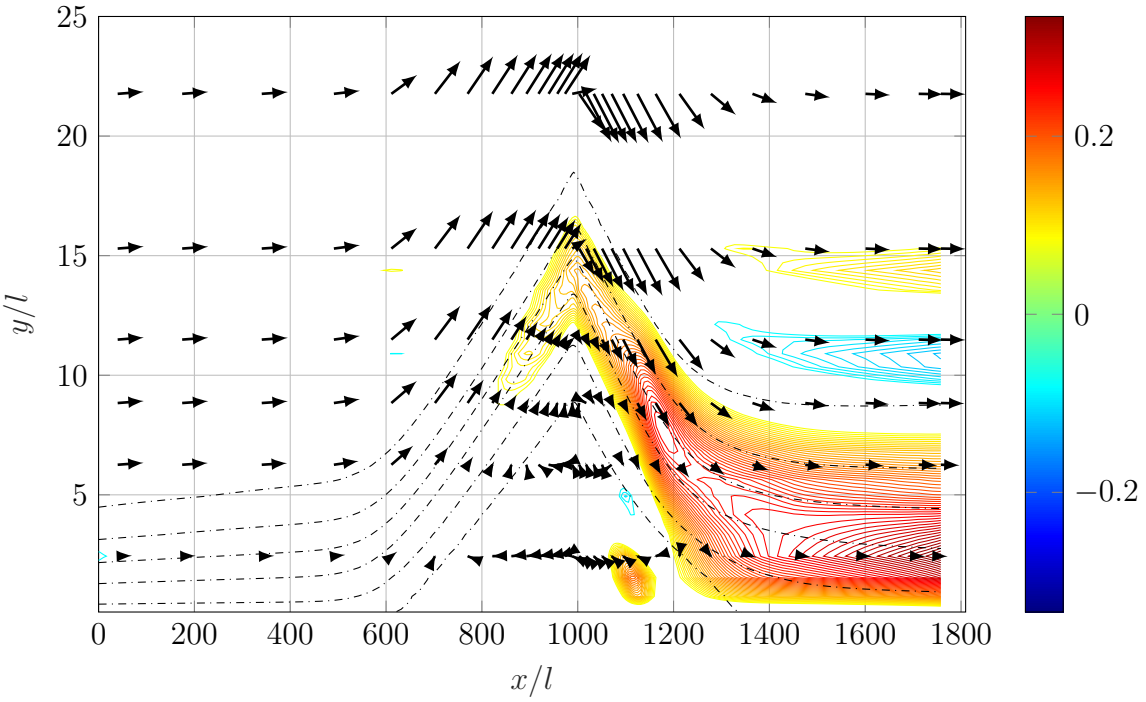

Figure 5.3.7: Contour of the real part $\Re(\tilde{u})/|\tilde{u}|_{max}$ of the $\theta_d = 2°$ steady mode $\omega = -0.001507i$. $(\overline{U},\overline{V})$-vectors indicated by black arrows. Contour level [0,0.1,0.3,0.5,0.7,0.9] of $\overline{U}$ in dash dotted lines.

can be found in appendix A. Note that the advection term $A^{\overline{W}}$ is strictly zero for the present case as there is no spanwise velocity $\overline{W}$. The advection terms in the Reynolds-Orr budget are virtually small, so the terms in Eq. (5.3.2) are zero. This means that the velocity vector is orthogonal to the vector quantity on the right, which represents the gradient of the phase or the in-plane wave vector. An illustrative example is depicted in Fig. 5.3.7 by considering the advection of $\tilde{u}$ by $\overline{U}$ and $\overline{V}$. It shows that velocity vectors represented by the black arrows are aligned with the isocontours of the eigenfunction. Towards the outflow, the structure increases in magnitude along the in-plane flow direction, which is excluded from the phase.

5.4 Intermediate conclusion

This chapter considers the Laminar Shock-Wave/Boundary-Layer Interaction (SWBLI). The numerical base flows consist of an incident shock impinging on the supersonic boundary layer handled in chapter 4.3. Three deflection angles of the shock ($\theta_d = 1°$, $2°$ and $3°$) are employed, according to the experiments of Giepman [2016], to induce different types of separation bubble. In order to ensure steady-state solutions, the encapsulated selective frequency damping method is applied to the Direct Numerical Simulations (DNS) solver and a third-order Weighted Essentially Non-Oscillatory (WENO) scheme is used for the reconstruction of the convective fluxes evaluated with a Harten-Lax-van Leer-Contact (HLLC) solver.

The flow fields of the three SWBLI cases are fundamentally different due to the shock strengths. While the smallest angle exhibits a very weak separation yielding only a small deflection of the boundary layer, the largest shock angle reveals the presence of a secondary recirculation zone within the primary separation bubble. Between these two extreme cases, the deflection $\theta_d = 2°$ induces one large separated region that should adhere to free interaction theory. The latter stipulates that, for a strong enough adverse pressure gradient, the wall-pressure distribution of a separated supersonic boundary layer is independent of the downstream mechanisms inducing the interaction. It yields to an equilibrium between the deflected viscous layer and the inviscid supersonic outflow. From this concept, several similarity laws are derived to assess the pressure distribution and, in case of laminar separation, the boundary layer deflection and the bubble length can be predicted. Although the smallest shock does not strictly verify the assumption of strong separation, the three SWBLIs reveal a very good agreement with the free interaction theory, while the experiments of Giepman [2016] exhibit significant discrepancies. It is suggested this is due to the measurement techniques and the slight freestream turbulence of the TST-27 blowdown transonic/supersonic wind tunnel of Delft University of Technology.

In the last section, the stability of the SWBLI is handled. A convective instability related to the Kelvin-Helmholtz (KH) mode and two steady global modes are considered. The former is based on the SWBLI with the intermediate shock strength and, for comparison purpose, the latter considers one steady mode for $\theta_d = 2°$ and one for $\theta_d = 3°$. The introduction of a Dirac impulse within the domain to reconstruct the convective mode shows that the perturbation is significantly amplified when it travels through the shock and within the bubble such that it suggests the presence of an absolute instability in the bubble. Furthermore, the mode observed in the lifted shear layer is a KH instabil-

ity, which degenerates into a TS wave after the reattachment. The Reynolds-Orr energy budget reveals that the two modes have their common origins in the shear stress while their differences lie in the main advection contributions which are destabilising for the KH wave and stabilising for the TS wave. In addition, the diffusive term is significantly more stabilising for the TS waves than for the KH ones. This is due to the inviscid nature of the KH modes travelling through the inflectional SWBLI part. Finally, the characteristics of the steady modes are considered by analysing the Reynolds-Orr energy balance. It reveals that the contribution to the steadiness of the modes is due to the very small advection caused by the alignment of the in-plane velocity vector with the constant phase levels; the mode is very long and does not have any phase structure in the streamwise direction, yielding a standing wave.

6. Conclusion

First, several theoretical aspects of the linear stability theory are handled, followed by mathematical considerations for the discretisation of the stability equations with a spectral method based on the Chebyshev polynomials. Two mappings are presented to transform the domain from the Chebyshev space to a physical space. The eigenvalue problem is built and several boundary conditions are considered. Furthermore, the linearised pressure Poisson equation initially derived by Theofilis [2017] for incompressible problems is extended to the current compressible BiGlobal framework in order to provide an additional boundary condition, which removes spurious pressure modes from the stability solution. Finally, two eigensolvers are discussed in order to yield stability results with very high accuracy.

Secondly, the validation of the BiGlobal solver is handled with the relatively simple stability analysis of the parallel Blasius, which is well documented in the literature. The compressible and incompressible base flows computed by Groot [2013] are reused to reduce the source of error. In addition to the original case, a spanwise velocity is added to this base flow such that the flow is rotated in the direction of the most unstable mode. Although it leads to the same physical modes, it involves other terms of the BiGlobal equations for the validation of the solver. Finally, we find excellent agreements with the results of Groot [2013] and with the literature in general for both compressible and incompressible Blasius flows. Therefore, we deem that the BiGlobal stability solver developed in the current thesis is verified.

Thirdly, the stability of subsonic and supersonic developing boundary layers is considered. Different boundary conditions for the wall and freestream boundaries are employed to analyse the impact on the results. We conclude that the Dirichlet conditions for the velocity and temperature perturbation variables combined with an extension to the compressible BiGlobal framework of the linearised pressure Poisson equation provides excellent results and removes the spurious modes related to pressure boundary closure. In addition, a convergence analysis shows that the number of collocation nodes in the streamwise direction is limited by the computational memory. On the other hand, the spatial characteristics of the Tollmien-Schlichting waves are evaluated with the BiGlobal and one-dimensional Linear Stability Theory (LST) stability methods. While it shows an excellent agreement for the subsonic case, the supersonic equivalent exhibits significant discrepancies due to the complexity of the compressible Tollmien-Schlichting mode and the inflow boundary. Nonetheless, the wave packet corresponding to the Tollmien-Schlichting instability travelling at a certain group speed is successfully reconstructed for both boundary layers and it illustrates clearly the convective behaviour of this mode. Finally, by removing the group speed from the base flow, we represent for the first time a convective mode by an unique isolated eigenfunction. The related spectrum exhibits

a cusp with a branch point that is conjectured to show more favourable convergence characteristics compared to a continuous branch. We emphasize that this result consists of a major improvement for the study of convective instabilities.

Finally, we consider the laminar shock-wave/boundary-layer interactions. The base flow is computed with direct numerical simulations according to the set-up of the experiments conducted by Giepman [2016] in the transonic/supersonic wind tunnel of Delft University of Technology. A comparison of the numerical and experimental results with the free interaction theory reveals discrepancies, which are potentially caused by the measurement techniques of the latter, that tend to underestimate significantly the size of the separated region. Considering the numerical base flows, we reveal the presence of a convective mode associated to the Kelvin-Helmholtz waves in the laminar shock-wave/boundary-layer interactions. It originates in the shear layer of the separated region and degenerates into Tollmien-Schlichting waves after the reattachment of the boundary layer. With the Reynolds-Orr energy budget, we highlight the differences between these two types of instability. The chapter ends with the comparison of steady modes at two different shock angles. Through the Reynolds-Orr energy balance, we find that this standing wave (i.e. not advected by the flow) is caused by the alignment of the in-plane velocity and the constant phase levels of the mode.

6.1 Recommendations and future research work

First, in the present thesis, we highlighted the representation of convective instability as absolute instability in a moving reference frame. Future research would focus on the effectiveness of this representation. The improvement of the convergence rate with respect to the number of streamwise collocation nodes has to be quantified. In addition, convergence analyses have to be carried out to determine the influence of the domain length and of the inlet location on the cusp representation.

Secondly, as presented with the stability analysis of the shock-wave/boundary-layer interaction, the Tollmien-Schlichting and the Kelvin-Helmholtz waves can exist simultaneously in a single eigenmode. Although the shape of the eigenfunctions allows identifying the two instabilities, future research work would consist of the exact distinction between the Tollmien-Schlichting and the Kelvin-Helmholtz waves through the Reynolds-Orr analysis to be conducted on viscous and inviscid BiGlobal simulations of the same (viscous) shock-wave/boundary-layer interaction base flow. Thereby the transition from one type of wave to the other type can be identified.

Thirdly, we conducted separately the Reynolds-Orr methodology on the different modes of the convective wave packet. A complement to this study would be to apply the Reynolds-Orr energy balance on the entire wave packet at different instants, aiming to characterise the movement of the perturbation. In addition, detailed analyses about the integrand of the production terms would provide information about the laminar-turbulent transition triggered by the Tollmien-Schlichting and the Kelvin-Helmholtz modes. Similar analyses of the wave packet shall be applied to the shock-wave/boundary-layer interaction to find the mechanisms underlying the absolute perturbation behaviour at the top of the separation bubble.

Bibliography

Åkervik, E., Brandt, L., Henningson, D. S., Hœpffner, J. m., Marxen, O. and Schlatter, P. [2006]. *Steady solutions of the Navier-Stokes equations by selective frequency damping*, Physics of Fluids 18(6): 068102–4.

Åkervik, E., Ehrenstein, U., Gallaire, F. and Henningson, D. S. [2008]. *Global two-dimensional stability measures of the flat plate boundary-layer flow*, European Journal of Mechanics - B/Fluids 27(5): 501–513.

Alizard, F. and Robinet, J.-C. [2007]. *Spatially convective global modes in a boundary layer*, Physics of Fluids 19(11): 114105–12.

Anderson, E., Bai, Z., Bischof, C., Blackford, L. S., Demmel, J., Dongarra, J., Du Croz, J., Greenbaum, A., Hammarling, S., McKenney, A. and Sorensen, D. [2012]. *LAPACK Users' Guide*, Society for Industrial and Applied Mathematics.

Anderson, J. D. [2011]. *Fundamentals of Aerodynamics Engineering*, McGraw Hill Series in Aeronautical and Aerospace Engineering, fifth edn, McGraw-Hill Higher Education.

Babinsky, H. and Harvey, J. K. [2011]. *Shock wave-boundary-layer interactions*, Cambridge University Press.

Balakumar, P. and Malik, M. [1992]. *Discrete modes and continuous spectra in supersonic boundary layers*, Journal of Fluid Mechanics 239: 631–656.

Batterson, J. W. [2011]. *The Biglobal Instability of the Bidirectional Vortex*, PhD thesis.

Boin, J. P., Robinet, J. C., Corre, C. and Deniau, H. [2006]. *3D Steady and Unsteady Bifurcations in a Shock-wave/Laminar Boundary Layer Interaction: A Numerical Study*, Theoretical and Computational Fluid Dynamics 20(3): 163–180.

Borges, R., Carmona, M., Costa, B. and Don, W. S. [2008]. *An improved weighted essentially non-oscillatory scheme for hyperbolic conservation laws*, Journal of Computational Physics 227(6): 3191–3211.

Carrière, P., Sirieix, M. and Solignac, J. L. [1969]. Similarity properties of the laminar or turbulent separation phenomena in a non-uniform supersonic flow, *Applied Mechanics*, Springer Berlin Heidelberg, pp. 145–157.

Chapman, C.-J. [2000]. *High Speed Flow*, Cambridge, UK: Cambridge University Press.

Chapman, D., Kuehn, D. and Larson, H. [1958]. Investigation of Separated Flow in Supersonic and Subsonic Streams with Emphasis of the Effect of Transition , *Technical Report 1356*, National Advisory Committee for Aeronautics. Ames Aeronautical Lab, Moffett Field, CA, United States.

Chapman, D. R. [1949]. *Temperature and Velocity Profiles in the Compressible Laminar Boundary Layer with Arbitrary Distribution of Surface Temperature*, Journal of the Aeronautical Sciences 16(9): 547–565.

Clemens, N. T. and Narayanaswamy, V. [2014]. *Low-Frequency Unsteadiness of Shock Wave/Turbulent Boundary Layer Interactions*, Annual Review of Fluid Mechanics 46(1): 469–492.

Courant, R. and Friedrichs, K. O. [1999]. *Supersonic Flow and Shock Waves*, Vol. 21 of *Applied Mathematical Sciences*, Springer New York.

Davidson, P. [2015]. *Turbulence: An Introduction for Scientists and Engineers*, Oxford University Press.

De Vicente, J., Rodriguez, D., Gonzalez, L. and Theofilis, V. [2012]. High-Order Numerical Methods for BiGlobal Flow Instability Analysis and Control, p. 187–234.

Degrez, G., Boccadoro, C. H. and Wendt, J. F. [1987]. *The interaction of an oblique shock wave with a laminar boundary layer revisited. An experimental and numerical study*, Journal of Fluid Mechanics 177(4): 247–263.

Dogval, A. V., Kozlov, V. V. and Michalke, A. [1994]. *Laminar Boundary Layer Separation: Instability and Associated Phenomena*, Progress in Aerospace Sciences 30(1): 61–94.

Dolling, D. S. [2001]. *Fifty Years of Shock-Wave/Boundary-Layer Interaction Research: What Next?*, AIAA Journal 39(8): 1517–1531.

Dutykh, D. [2016]. A brief introduction to pseudo-spectral methods: application to diffusion problems. Lecture - 55 pages, 40 references, 14 figures.
URL: *https://cel.archives-ouvertes.fr/cel-01256472*

Eckert, E. [1955]. *Engineering relations for friction and heat transfer to surfaces in high velocity flow*, Journal of the Aeronautical Sciences 22(8): 585–587.

Ehrenstein, U. and Gallaire, F. [2005]. *On two-dimensional temporal modes in spatially evolving open flows: the flat-plate boundary layer*, Journal of Fluid Mechanics 536: 209–218.

Erdos, J. and Pallone, A. [1963]. Shock-Boundary Layer Interaction and Flow Separations.

Ferri, A. [1939]. Experimental Results with Airfoils Tested in the High-Speed Tunnel at Guidonia, *Technical Report NACA-TM-946*.

Frahnert, H. and Dallmann, U. C. [2002]. Examination of the Eddy-Viscosity Concept Regarding its Physical Justification, *New Results in Numerical and Experimental Fluid Mechanics III*, Springer Berlin Heidelberg, Berlin, Heidelberg, pp. 255–262.

Gadd, G. E. [1953]. *Interactions Between Wholly Laminar or Wholly Turbulent Boundary Layers and Shock Waves Strong Enough to Cause Separation*, Journal of the Aeronautical Sciences 20(11): 729–739.

Ganapathisubramani, B., Clemens, N. T. and Dolling, D. S. [2007]. *Effects of upstream boundary layer on the unsteadiness of shock-induced separation*, Journal of Fluid Mechanics 585: 369–394.

Ganapathisubramani, B., Clemens, N. T. and Dolling, D. S. [2009]. *Low-frequency dynamics of shock-induced separation in a compression ramp interaction*, Journal of Fluid Mechanics 636: 397–425.

Giepman, R. H. M. [2016]. *Flow Control for Oblique Shock Wave Reflections Interactions*, PhD thesis.

Greber, I., Hakkinen, R. J. and Trilling, L. [1958]. *Laminar boundary layer oblique shock wave interaction on flat and curved plates*, Zeitschrift für angewandte Mathematik und Physik ZAMP 9(5): 312–331.

Grilli, M., Schmid, P. J., Hickel, S. and Adams, N. A. [2012]. *Analysis of unsteady behaviour in shockwave turbulent boundary layer interaction*, Journal of Fluid Mechanics 700: 16–28.

Groot, K. J. [2013]. *Derivation of and Simulations with BiGlobal Stability Equations*, Master's thesis.

Groot, K. J., Serpieri, J., Kotsonis, M. and Pinna, F. [2017]. Secondary Stability Analysis of Crossflow Vortices using BiGlobal Theory on PIV Base Flows, *55th AIAA Aerospace Sciences Meeting*, number AIAA 2017-1880, Reston, Virginia.

Guiho, F., Alizard, F. and Robinet, J. C. [2015]. Global Instability in Shock Wave Laminar Boundary-Layer Interaction, *Instability and Control of Massively Separated Flows*, Springer International Publishing, Cham, pp. 97–102.

Guiho, F., Alizard, F. and Robinet, J. C. [2016]. *Instabilities in oblique shock wave/laminar boundary-layer interactions*, Journal of Fluid Mechanics 789: 1–35.

Hakkinen, R. J., Greber, I., Trilling, L. and Abarbanel, S. S. [1959]. The Interaction of an Oblique Shock Wave with a Laminar Boundary Layer , *Technical report*, Massachussets Institute of Technology.

Holmes, M. H. [2013]. *Introduction to Perturbation Methods*, Vol. 20, Springer-Verlag New York.

Jiang, G.-S. and Shu, C.-W. [1996]. *Efficient implementation of weighted eno schemes*, Journal of Computational Physics 126(1): 202 – 228.
URL: *http://www.sciencedirect.com/science/article/pii/S0021999196901308*

Jones, L. E. and Sandberg, R. D. [2011]. *Numerical analysis of tonal airfoil self-noise and acoustic feedback-loops*, Journal of Sound and Vibration 330(25): 6137–6152.

Jordi, B. E., Cotter, C. J. and Sherwin, S. J. [2014]. *Encapsulated formulation of the selective frequency damping method*, Physics of Fluids 26(3): 034101–11.

Katzer, E. [1989]. *On the lengthscales of laminar shock/boundary-layer interaction*, Journal of Fluid Mechanics 206: 477–496.

Larchevêque, L. [2016]. Low- and Medium-Frequency Unsteadinesses in a Transitional Shock–Boundary Reflection with Separation, *54th AIAA Aerospace Sciences Meeting*, number AIAA 2016-1833, American Institute of Aeronautics and Astronautics, San Diego, California, USA.

Lehoucq, R. B., Sorensen, D. C. and Yang, C. [2012]. *ARPACK Users' Guide*, Society for Industrial and Applied Mathematics.

Lesshafft, L. [2017]. Artificial Eigenmodes in Truncated Flow Domains.

Liu, X.-D., Osher, S. and Chan, T. [1994]. *Weighted Essentially Non-oscillatory Schemes*, 115(1): 200–212.

Mack, L. [1976]. *A numerical study of the temporal eigenvalue spectrum of the blasius boundary layer.*, Journal of Fluid Mechanics 73: 497–520.

Malik, M. [1990]. *Numerical methods for hypersonic boundary layer stability*, Journal of Computational Physics 86(2): 376—413.

Masahito, A., Kiyohiro, A. and Nishioka, M. [1996]. *A nonlinearity-coupled receptivity process generating a Tollmien-Schlichting wave behind a backward-facing step*, Fluid Dynamics Research 17: 225–236.

Matheis, J. and Hickel, S. [2015]. *On the Transition Between Regular and Irregular Shock Patterns of Shock-Wave/Boundary-Layer Interactions* , Journal of Fluid Mechanics 776: 200–234.

Pasquariello, V., Hickel, S. and Adams, N. A. [2017]. *Unsteady effects of strong shock-wave/boundary-layer interaction at high Reynolds number*, Journal of Fluid Mechanics 823: 617–657.

Pinna, F. [2012]. *Numerical study of stability and transition of flows from low to high Mach number*, PhD thesis, Von Karman Institute for Fluid Dynamics and Universitá "La Sapienza" di Roma.

Pinna, F. and Groot, K. J. [2014]. Automatic derivation of stability equations in arbitrary coordinates and for different flow regimes, *44th AIAA Fluid Dynamics Conference*, number AIAA 2014-2634, Reston, Virginia.

Piot, E. [2008]. *Simulation numérique directe et analyse de stabilité de couches limites laminaires en présence de micro-rugosités*, PhD thesis.

Pope, S. [2000]. *Turbulent Flows*, Cambridge University press, Cornell University.

Rempfer, D. [2006]. *On Boundary Conditions for Incompressible Navier-Stok Problems*, Applied Mechanics Reviews 59: 107–125.

Reshotko, E. and Tumin, A. [2006]. Application of Transient Growth Theory to Bypass Transition, *IUTAM Symposium on One Hundred Years of Boundary Layer Research*, Springer, Dordrecht, Dordrecht, pp. 83–93.

Rist, U. [2005]. *Instability and Transition Mechanisms in Laminar Separation Bubbles* , Proceedings of Low Reynolds Number Aerodynamics on Aircraft Including Applications in Emerging Unmanned Aerial Vehicle Technology .

Rist, U. and Maucher, U. [2002]. *Investigations of time-growing instabilities in laminar separation bubbles*, European Journal of Mechanics - B/Fluids 21(5): 495–509.

Rizzetta, D. P., Burggraf, O. R. and Jenson, R. [1978]. *Triple-deck solutions for viscous supersonic and hypersonic flow past corners*, Journal of Fluid Mechanics 89(3): 535–552.

Robinet, J. C. [2007]. *Bifurcations in shock-wave/laminar-boundary-layer interaction: global instability approach*, Journal of Fluid Mechanics 579: 85–112.

Robitaillié-Montané, C. [2005]. *Une approche non locale pour l'étude des instabilités linéaires : application à l'écoulement de couche limite compressible le long d'une ligne de partage*, PhD thesis.

Rodriguez, D. [2010]. *Global Instability of Laminar Separation Bubbles*, PhD thesis.

Rodriguez, D. and Theofilis, V. [2010]. *Structural changes of laminar separation bubbles induced by global linear instability*, Journal of Fluid Mechanics 655: 280–305.

Sansica, A., Sandham, N. D. and Hu, Z. [2014]. *Forced response of a laminar shock-induced separation bubble*, Physics of Fluids 26(9): 093601–14.

Sansica, A., Sandham, N. D. and Hu, Z. [2016]. *Instability and Low-Frequency Unsteadiness in a Shock-Induced Laminar Separation Bubble*, Journal of Fluid Mechanics 798: 5–26.

Sansica, A., Sandham, N. and Hu, Z. [2013]. Stability and Unsteadiness in a 2D Laminar Shock-Induced Separation Bubble, *43rd AIAA Fluid Dynamics Conference*, American Institute of Aeronautics and Astronautics, San Diego, California, USA.

Schlichting, H. [1960]. *Boundary layer theory*, McGraw-Hill series in mechanical engineering, McGraw-Hill.

Schmid, P. J. and Henningson, D. S. [2001]. *Stability and Transition in Shear Flows*, Springer.

Sivasubramanian, J. and Fasel, H. F. [2015]. Numerical Investigation of Shock-Induced Laminar Separation Bubble in a Mach 2 Boundary Layer, *45th AIAA Fluid Dynamics Conference*, American Institute of Aeronautics and Astronautics, Dallas, Texas, p. 59W.

Stewartson, K. and Williams, P. G. [1969]. *Self-Induced Separation*, Proceedings of the Royal Society A: Mathematical, Physical and Engineering Sciences 312(1509): 181–206.

Theofilis, V. [2017]. *The linearized pressure Poisson equation for global instability analysis of incompressible flows*, Theoretical and Computational Fluid Dynamics (online first).

Theofilis, V. and Colonius, T. [2004]. Three-Dimensional Instabilities of Compressible Flow over Open Cavities: Direct Solution of the BiGlobal Eivenvalue Problem, *34th AIAA Fluid Dynamics Conference and Exhibit*, American Institute of Aeronautics and Astronautics, Reston, Virigina, pp. 2004–13.

Theofilis, V., Hein, S. and Dallmann, U. [2000]. *On the origins of unsteadiness and three-dimensionality in a laminar separation bubble*, Philosophical Transactions of the Royal Society A: Mathematical, Physical and Engineering Sciences 358(1777): 3229–3246.

Touber, E. and Sandham, N. D. [2009]. *Large-Eddy Simulation of Low-Frequency Unsteadiness in a Turbulent Shock-Induced Separation Bubble* , Theoretical and Computational Fluid Dynamics 23(2): 79–107.

Weideman, J. A. C. and Reddy, S. C. [2000]. *A MATLAB differentiation matrix suite*, ACM Transactions on Mathematical Software 26(4): 465–519.
URL: *http://doi.acm.org/10.1145/365723.365727*

White, F. M. [1991]. *Viscous Flow*, McGraw Hill Series in Mechanical Engineering, McGraw-Hill Professional Publishing, University of Rhode Island.

Williams, P. G. [1975]. A reverse flow computation in the theory of self-induced separation, *in* R. D. Richtmyer (ed.), *Proceedings of the Fourth International Conference on Numerical Methods in Fluid Dynamics: June 24–28, 1974, University of Colorado*, Springer Berlin Heidelberg, Berlin, Heidelberg, pp. 445–451.

Yongzhao, L., Qiushi, L. and Shaobin, L. [2015]. *Modeling the Effect of Stability Bleed on Back-Pressure in Mixed-Compression Supersonic Inlets*, Journal of Fluids Engineering 137(12): 121101–13.

Zhang, S., Jiang, S. and Shu, C.-W. [2011]. *Improvement of Convergence to Steady State Solutions of Euler Equations with the WENO Schemes*, Journal of Scientific Computing 47(2): 216–238.

Zhang, S. and Shu, C.-W. [2006]. *A New Smoothness Indicator for the WENO Schemes and Its Effect on the Convergence to Steady State Solutions*, Journal of Scientific Computing 31(1-2): 273–305.

A. Reynolds-Orr energy terms

The Reynolds-Orr energy terms in the compressible BiGlobal stability momentum equations are grouped according to the advection (A_a) by the base flow velocity indicated with the superscript, advection (A_d) by the diffusion imposed through a temperature gradient, Reynolds stress (R) and dissipation (D) by the viscosity.

$$
\begin{aligned}
A_a^{\overline{U}} &= -i \int\int (\gamma M^2 \frac{\overline{P}}{\overline{T}} \overline{U} \tilde{u}^* \tilde{u}_x + \gamma M^2 \frac{\overline{P}}{\overline{T}} \overline{U} \tilde{v}^* \tilde{v}_x + \gamma M^2 \frac{\overline{P}}{\overline{T}} \overline{U} \tilde{w}^* \tilde{w}_x)\, dx\, dy \\
A_a^{\overline{V}} &= -i \int\int (\gamma M^2 \frac{\overline{P}}{\overline{T}} \overline{V} \tilde{u}^* \tilde{u}_y + \gamma M^2 \frac{\overline{P}}{\overline{T}} \overline{V} \tilde{v}^* \tilde{v}_y + \gamma M^2 \frac{\overline{P}}{\overline{T}} \overline{V} \tilde{w}^* \tilde{w}_y)\, dx\, dy \\
A_a^{\overline{W}} &= -i \int\int (\gamma M^2 \frac{\overline{P}}{\overline{T}} \overline{W} i\beta \tilde{u}^* \tilde{u} + \gamma M^2 \frac{\overline{P}}{\overline{T}} \overline{W} i\beta \tilde{v}^* \tilde{v} + \gamma M^2 \frac{\overline{P}}{\overline{T}} \overline{W} i\beta \tilde{w}^* \tilde{w})\, dx\, dy
\end{aligned}
$$

$$
\begin{aligned}
A_d = i \int\int & \frac{\tilde{u}^*}{Re} (\overline{\mu}_{\overline{T}} \overline{T}_y \tilde{u}_y + 2\overline{\mu}_{\overline{T}} \overline{T}_x \tilde{u}_x + \overline{\lambda}_{\overline{T}} \overline{T}_x \tilde{u}_x + \overline{\mu}_{\overline{T}} \overline{T}_y \tilde{v}_x + \overline{\lambda}_{\overline{T}} \overline{T}_x \tilde{v}_y + i\overline{\lambda}_{\overline{T}} \overline{T}_x \beta \tilde{w}) \\
& + \frac{\tilde{v}^*}{Re} (\overline{\lambda}_{\overline{T}} \overline{T}_y \tilde{u}_x + \overline{\mu}_{\overline{T}} \overline{T}_x \tilde{u}_y + 2\overline{\mu}_{\overline{T}} \overline{T}_y \tilde{v}_y + \overline{\lambda}_{\overline{T}} \overline{T}_y \tilde{v}_y + \overline{\mu}_{\overline{T}} \overline{T}_x \tilde{v}_x + i\overline{\lambda}_{\overline{T}} \overline{T}_y \beta \tilde{w}) \\
& + \frac{\tilde{w}^*}{Re} (i\overline{\mu}_{\overline{T}} \overline{T}_x \beta \tilde{u} + i\overline{\mu}_{\overline{T}} \overline{T}_y \beta \tilde{v} + \overline{\mu}_{\overline{T}} \overline{T}_y \tilde{w}_y + \overline{\mu}_{\overline{T}} \overline{T}_x \tilde{w}_x)\, dx\, dy
\end{aligned}
$$

$$
\begin{aligned}
R = -i \int\int & \tilde{u}^* (\gamma M^2 \frac{\overline{P}}{\overline{T}} \overline{U}_x \tilde{u} + \gamma M^2 \frac{\overline{P}}{\overline{T}} \overline{U}_y \tilde{v}) \\
& + \tilde{v}^* (\gamma M^2 \frac{\overline{P}}{\overline{T}} \overline{V}_x \tilde{u} + \gamma M^2 \frac{\overline{P}}{\overline{T}} \overline{V}_y \tilde{v}) \\
& + \tilde{w}^* (\gamma M^2 \frac{\overline{P}}{\overline{T}} \overline{W}_x \tilde{u} + \gamma M^2 \frac{\overline{P}}{\overline{T}} \overline{W}_y \tilde{v})\, dx\, dy
\end{aligned}
$$

$$
\begin{aligned}
D = i \int\int & \frac{\tilde{u}^*}{Re} (\overline{\mu}\, \tilde{u}_{yy} + 2\overline{\mu}\, \tilde{u}_{xx} - \overline{\mu}\, \beta^2 \tilde{u} + \overline{\lambda}\, \tilde{u}_{xx}) \\
& + \frac{\tilde{v}^*}{Re} (2\overline{\mu}\, \tilde{v}_{yy} + \overline{\mu}\, \tilde{v}_{xx} - \overline{\mu}\, \beta^2 \tilde{v} + \overline{\lambda}\, \tilde{v}_{xx}) \\
& + \frac{\tilde{w}^*}{Re} (2\overline{\mu}\, \tilde{w}_{yy} + \overline{\mu}\, \tilde{w}_{xx} - 2\overline{\mu}\, \beta^2 \tilde{w} - \overline{\lambda}\, \beta^2 \tilde{w})\, dx\, dy
\end{aligned}
$$